Computational Models Explaining Cochlear Implant Principles: A Hypothesis, Applications and Physical Validations

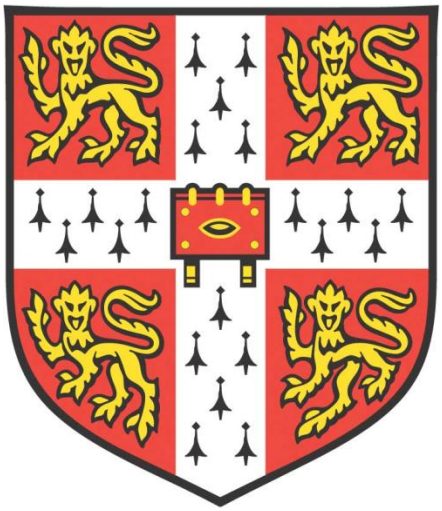

Botian Huang

Sidney Sussex College

Department of Clinical Neurosciences

University of Cambridge

This dissertation is submitted for the degree of Doctor of Philosophy

December 2023

DECLARATION

This thesis is the result of my own work and includes nothing which is the outcome of work done in collaboration except as declared in the preface and specified in the text. I confirm that this thesis is not substantially the same as any work that has already been submitted before for any degree or other qualification except as declared in the preface and specified in the text. This thesis does not exceed the prescribed word limit for the Clinical Medicine Degree Committee.

ABSTRACT

Computational models explaining cochlear implant principles: A hypothesis, applications and physical validations

Botian Huang

This thesis combines computational modelling with cadaveric and clinical data to deepen our understanding of cochlear implants (CIs). For the past two or three decades, improvements in CI performance have been limited due to gaps in our understanding of how CI interacts with auditory nerves. Persistent questions, such as the unexplained polarity effect and the impact of CI-modiolus distance, have remained unclear. This research aims to improve our knowledge of CI principles. It introduces a hypothesis, based on precise computational models, that explains these unclear phenomena, suggesting the internal auditory meatus (IAM) as a key factor in neural activations by CI. This work also involves validating these computational models through physical experiments on cochleae and CIs. It compares clinical measurements from patients and from simulations like extra-cochlear electrodes and scalp voltages. Additionally, it proposes a proof-of-concept in-vitro cell culture model based on these simulations.

In detail, Chapter 2 focuses on validating these models against human temporal bone specimens for evaluating the accuracy of computational methods. Chapter 3 develops a comprehensive head model that sheds light on how CIs affect neural pathways and electric field intensities, with a special focus on the IAM. This leads to the proposed hypothesis. Chapter 4 explores clinical applications, studying extra-cochlear electrodes and simulating CI-induced scalp voltages, supported by cadaveric and clinical data. Chapter 5 introduces a novel in-vitro model for studying responses of spiral ganglion neurons (SGNs) to CIs. Overall, this thesis aims to advance our understanding of CI principles and opens up new possibilities for research in the field of auditory prosthetics.

ACKNOWLEDGMENT

Thanks to my supervisor Manohar Bance for the guidance in the field of cochlear implants. Thanks to colleagues Dr. Iwan Roberts, Dr. Chloe Sword and everyone who helped me with this work.

Thanks to Yi-Lin Yu and Shiqiang Liu for the time together in lab. Thanks to all the friends for the enjoyable time having meals together.

The time spent in the cleanroom was also non-forgettable. Regretfully the fabrication work in the first half of my PhD did not end as expected. Thanks to Prof. George Malliaras for the generous support.

Finally, thanks to my parents for their support. Regretfully I was unable to visit home within these years in the UK before finishing my work.

CONTENTS

LIST OF TABLES

LIST OF FIGURES

LIST OF ABBREVIATIONS AND ACRONYMS

CI	Cochlear Implants
ST	Scala Tympani
SV	Scala Vestibuli
SM	Scala Media
RC	Rosenthal's canal
IAM	Internal Auditory Meatus
SGN	Spiral Ganglion Neuron
EFI	Electrical Field Imaging
EE	Extra-cochlear Electrodes
ECAP	Electrically-evoked Compound Action Potential
LW	Lateral Wall
PM	Peri-modiolar
CT	Computed Tomography
FEM	Finite Element Method

1 INTRODUCTION

Cochlear implants (CIs), recognized as the most successful neural prostheses, have restored functional hearing to one million individuals worldwide who are either partially or completely deaf[1]. However, the performance of CIs has seen no significant improvements in the sentence recognition rate of patients over the past 30 years due to the lack of understanding of how to optimise their function[2].

In order to provide some current understanding of how cochlear implants work, I briefly explain cochlear anatomy, how hearing loss happens and then describe the functions of cochlear implants. Then I introduce several clinical phenomena with CIs that remain unexplained, which could point to some fundamental issues with CIs. Next, due to the difficulties in physically acquiring data from the cochlea or auditory nerve, computational methods are presented as a feasible approach to explain or predict clinical data. Lastly, the structure of this thesis is also outlined.

1.1 Hearing and Cochlear Implants

1.1.1 Cochlea and auditory system

In the process of normal hearing, acoustic sounds are first converted into mechanical vibrations by the tympanic membrane and the middle ear ossicles. These mechanical vibrations are then transformed into an intracochlear fluid pressure wave due to the movement of the footplate of the stapes at the oval window of the cochlea, as shown in the left part of Figure 1.1.

The cochlea, which is part of the inner ear, is a tapered and coiled tube that makes approximately 2.5 turns around a porous conical bony structure known as the modiolus. The cochlea is embedded within the temporal bone and is divided into three sections by membranes within it, known as scalae (Figure 1.1 right). These include the scala vestibuli, which is connected to the stapes and oval window; the scala media, which houses the organ of Corti; and the scala tympani, which is connected to the round window. The modiolus serves as a housing for the auditory nerve, which carries signals from the cochlea to the brain. The auditory nerve passes through a canal in the temporal bone called the internal auditory meatus (IAM). Bundles of auditory nerve fibres travel through the internal auditory meatus, allowing auditory information to be relayed from the cochlea to the central auditory pathways in the brain.

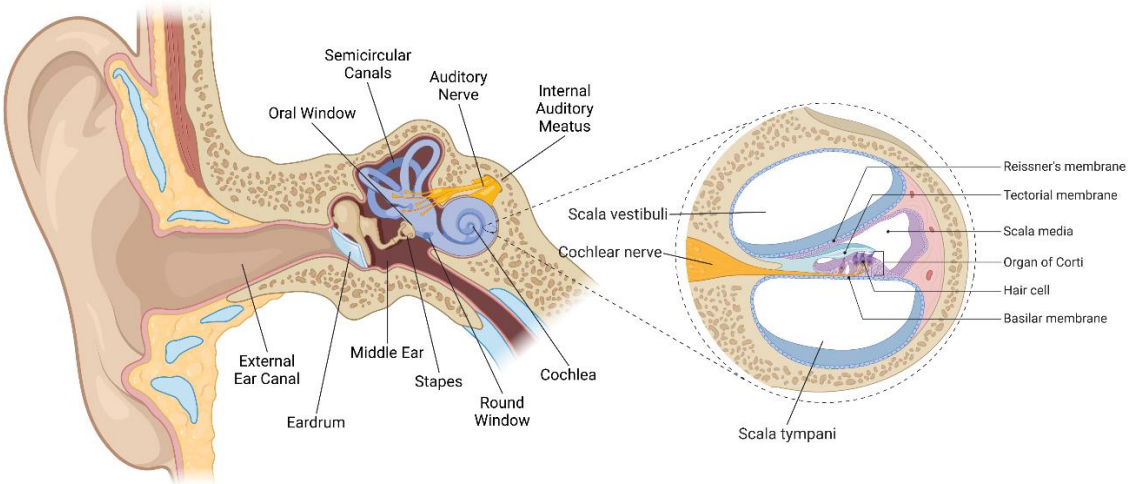

Figure 1.1: Anatomy of the auditory system and cochlea. Vibrations are transmitted from the eardrum to the oval window of the cochlea through middle ear. Auditory signals are transmitted by the auditory nerve through modiolus and internal auditory meatus to the brain. In the cochlea, the scala tympani, scala vestibuli and scala media are filled with fluids. Hair cells can detect vibrations and activate the cochlear nerve, resulting in hearing. Figure made with Biorender®.

The intracochlear fluid pressure wave causes displacement of the basilar membrane, an element of the cochlea that separates the scala media from the scala tympani. The basilar membrane's stiffness varies along the course of the cochlea, being stiffer and narrower at the base and more flexible and wider at the apex. These properties lead to what is called tonotopic organization of the cochlea, where high-frequency sounds are transduced at the basal end, and low-frequency sounds at the apical end.

The displacement of the basilar membrane is sensed by the filamentous stereocilia on hair cells in the organ of Corti, which lie within the scala media. When these stereocilia are deflected by the relative shearing movements of the tectorial and basilar membrane in the organ of Corti, this causes an influx of positive ions leading to hair cell depolarization. This depolarization triggers a release of neurotransmitters that subsequently depolarize afferent auditory nerve fibers. This complex process allows us to perceive and interpret sound.

1.1.2 Hearing loss

Hearing loss occurs when there is disruption at any point in the auditory pathway, reducing or preventing the transmission of sound. It is categorized by the specific location of the pathology within the auditory system.

Conductive hearing loss stems from damage or obstruction within the outer or middle ear. This impedes the conduction of acoustic sound waves through the external auditory canal, tympanic membrane, and ossicles to the inner ear. Common causes include the build-up of earwax, perforation of the eardrum, otitis media, otosclerosis affecting the stapes bone, or malformation of the outer/middle ear structures. Conductive loss typically manifests as an attenuation or reduction in perceived loudness across all frequencies.

Sensorineural hearing loss is the most common type of hearing loss. It originates within the cochlea, or further along the auditory nerve pathway. Damage to the delicate hair cells that detect sound within the cochlea is a common cause[3]. Hair cell damage in the cochlea can lead to additional degeneration of the auditory nerve over time[4]. Besides, factors such as acoustic injury will cause direct degenerations of the peripheral nerve fibres of spiral ganglion neurons, which will also contribute to sensorineural hearing loss[5].

A key difference between sensorineural and conductive loss is that hair cell damage in the cochlea is permanent, as human hair cells will not regenerate if damaged. While some medical and surgical interventions can help certain conductive hearing loss causes, severe or profound sensorineural hearing loss often requires cochlear implants to restore auditory function.

1.1.3 How cochlear implants work

Cochlear implants aim to restore hearing in patients with severe to profound sensorineural hearing loss by bypassing non-functional hair cells and directly stimulating the auditory nerve electrically. This technology converts acoustic sound waves picked up by an external microphone into encoded electrical signals that activate auditory neurons, allowing users to perceive sound.

The cochlear implant system has both external and internal components working in tandem. Externally, a behind-the-ear speech processor analyses and filters incoming sound using advanced digital signal processing strategies to optimize speech encoding. Coded signals are transmitted to an internal receiver using a radio frequency coil link, which also powers the implant. A schematic of a cochlear implant is shown in Figure 1.2.

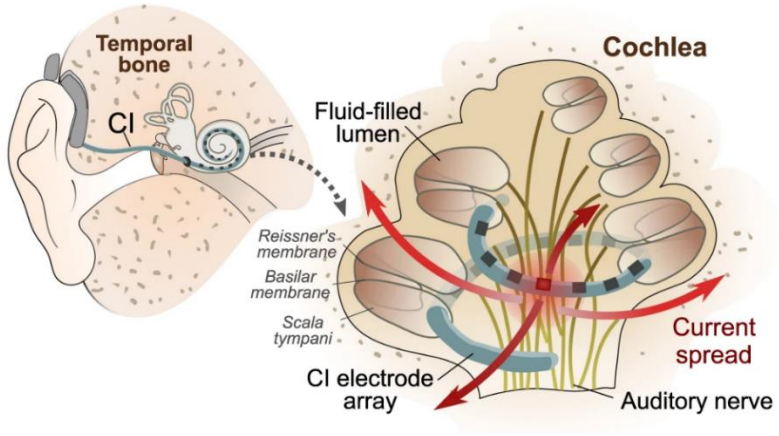

Figure 1.2: Schematic of a cochlear implant. The cochlear implant is inserted into the scala tympani of the cochlea through the round window. The cross-sectional view shows the positioning of the electrode within the spiral cochlea. This allows stimulation of the auditory nerve housed in modiolus. Figure adapted from Lei *et al.*[6] CC BY 4.0.

Internally, the receiver is secured in a mastoid bone recess and integrated circuitry decodes the received signals which are sent through silicone-coated wires to electrodes

mounted on a flexible electrode array inserted into the cochlea. The array typically contains 12-22 platinum-iridium contacts that stimulate spiral ganglion neurons based on input frequency and intensity, with lower frequencies channelled apically and higher frequencies more basally, to mimic the normal "tonotopic" organisation. An extracochlear ground electrode is usually placed under the temporal muscles scalp, either on the casing of the receiver-stimulator (Med-El and Advanced Bionics), or in some designs as an additional floating lead (Cochlear corp).

When activated by biphasic current pulses, the electrodes directly stimulate adjacent auditory neurons, bypassing dysfunctional hair cells. Despite its limitations, this novel approach provides tremendous benefit. Most recipients show improved speech perception and auditory awareness, and exhibit greatly enhanced communication and quality of life[7].

The modern multi-channel cochlear implant was developed in the 1980s[8]. The last major breakthrough in performance of cochlear implants was the development of the Continuous-Interleaved-Sampling strategy in 1991, which improved the sentence recognition rate in quiet to 70%~80% correct[9]. Regretfully, in terms of the speech recognition rate of patients, it has been more than 30 years, and despite the large amount of research going on, we have not seen a further increase of it to date[2].

1.2 Challenges in Understanding Cochlear Implant Principles

In this section, I will introduce several clinical findings that have been discovered, replicated, or studied over the decades, yet remain difficult to fully comprehend. These findings might point to some underlying currently poorly understood principles. Additionally, I will discuss the methods used to physically assess cochlear implant outcomes in patients. However, due to the cochlea's deeply embedded location within the bone, the information we can obtain is still quite limited in-vivo.

1.2.1 Electrode positions and spread of excitations

Modern cochlear implant electrode arrays have between 12-22 electrode contacts intended to stimulate localized, distinct regions of the auditory nerve. However, in

practice, it is believed that the excitation fields from neighbouring electrodes overlap due to current spread in the cochlear fluids[10] (Figure 1.3). This reduced selectivity, or large spread of excitation, limits the number of perceptually discriminable pitches. Past studies have shown that speech recognition does not improve with more than 8 active electrodes, at least with a speaker in quiet[11]. It can even be difficult for patients to simply discriminate sounds produced by two adjacent electrode contacts[12].

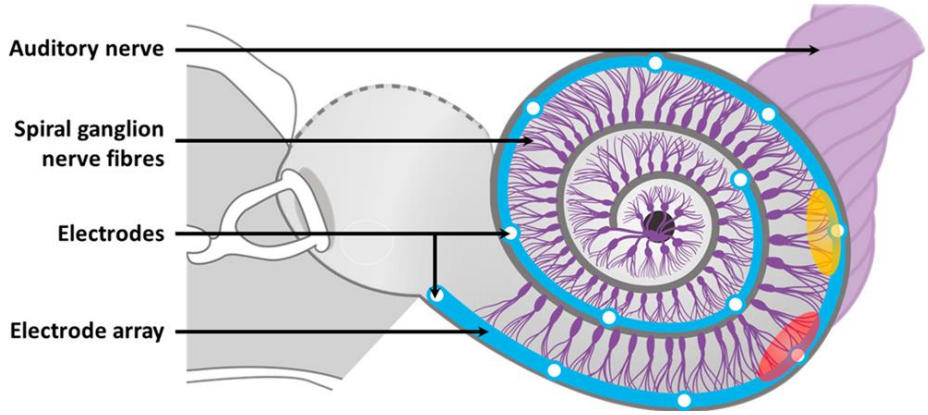

Figure 1.3: Illustration of spread of excitation. The voltage spread from CI electrodes in cochlea (a lateral wall one). Figure adapted from Joly *et al*.[13] CC BY 4.0.

Therefore, several attempts have been made to improve or understand CI performance. Considering the anatomy (Figure 1.4A), intuitively, the most straightforward way to reduce current spread might be to place the CI closer to the modiolus. This would take electrodes much closer to the spiral ganglion neuron bodies, which, in theory, could provide more focused stimulation and lower the current thresholds. In light of this, the modiolus hugging, or peri-modiolar (PM) CIs were developed around 20 years ago[14]. The theoretical improvement of reducing spread of excitation is illustrated in Figure 1.4B. Comparing to normal straight "lateral wall" (LW) ones, these pre-curved CIs remains closely contacted with the modiolus walls after insertion[15].

While PM devices have been widely used in patients, even after 20 years of clinical practice and research, we still have not come to conclusions how (or whether) this placement is benefiting patients. The literature has shown conflicting results on their performance. Some papers have reported improved pitch-ranking ability[16], decreased threshold levels and channel interactions[17] for PM electrodes compared with LW ones. Others have found weak or no correlation between the electrode position and hearing outcomes in relatively long-term post-implantation experiments[18,19]. Yet others have

reported the electrode-modiolus distance does not affect stimulation thresholds[20]. Another factor to consider is that PM electrodes are more likely to cause insertion trauma during implantation surgery[21], which can affect the residual hearing preservation for patients.

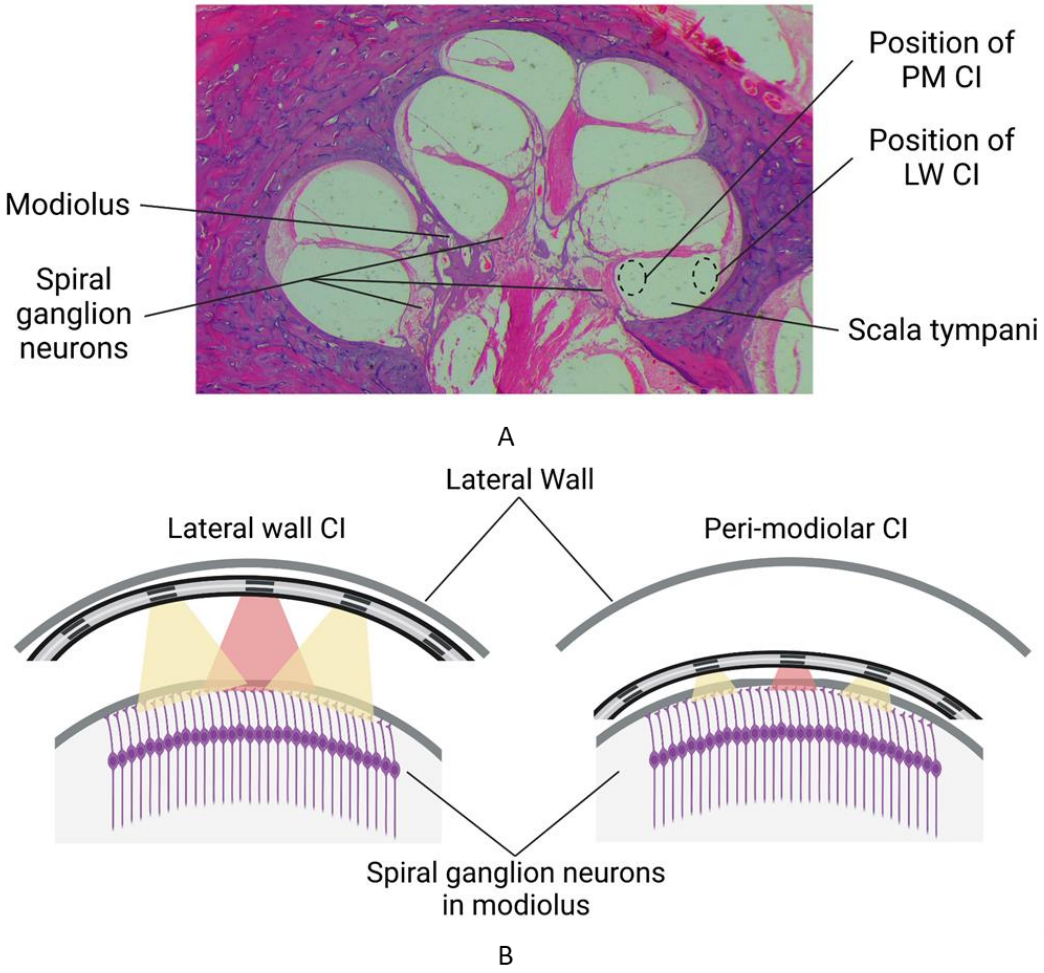

Figure 1.4: Illustration of CI positions and spread of excitations. (A) A histology cochlea slice showing the relative position of the modiolus, spiral ganglion neurons and CIs. The positions of lateral wall (LW) and peri-modiolar (PM) CIs are indicated. (B) Illustration of how cochlear positions will (in theory) affect the spread voltage and therefore how it will affect the spiral ganglion neurons. Figure made with Biorender®.

Another interesting surgical technique is to use the "pull-back" technique, which is to pull a fully or over inserted electrode array back slightly[22]. This could place the CI electrode position closer to modiolus near the base, enabling a comparison of CI outcomes on the same patient before and after this pull-back. Results indeed showed a slightly lowered threshold[23] and a reduced spread of excitation from electrically evoked compound action potentials (ECAP) measurements[24].

Though existing results provide some evidence that PM electrodes might stimulate differently than LW electrodes, how PM implants exactly work and if and why they are making improvements is still unclear[25]. While physiological spread of excitation measurements and pitch ranking results typically correlate with each other in individual patients, neither of them is shown to be strongly related to their speech recognition performance[26,27]. The peak amplitudes of ECAPs could be related to perceived loudness in some studies[11], however, this is not enough to assess actual CI performance.

Both LW and PM implants are still widely used. It remains unclear why PM implants do not show significantly better performance over the past 20 years, despite being much closer to spiral ganglion neurons. This question then remains to be discussed if the electrode position matters with monopolar stimulation (the commonly used stimulation mode). Particularly, the question remains: are CIs really stimulating spiral ganglion cell bodies, and if not where are the sites of stimulation?

1.2.2 Polarity effect

Another well-known and longstanding observed phenomenon is also difficult to explain adequately, i.e., the polarity effect. This refers to the stimulation being either cathodic or anodic. This question has two components: the effectiveness of stimuli polarity, and the delay of the neural response (latency).

In the 1980s ~ 90s, researchers found in animal cochleae that the cathodic phase was more effective than anodic[28]. However, in human patients, the polarity effect was the opposite: anodic-leading stimuli had lower threshold levels in patients than cathodic[29], and the result was consistent when using different stimuli pulse shapes[30]. ECAP results have also confirmed that anodic-leading stimuli evoke higher neural excitations[31]. Many other researchers have found similar findings, and this is well summarized by Carlyon et al.[30]

With regard to latency, studies have reported that at a fixed stimulation level, ECAPs show a shorter latency when evoked by anodic-leading pulses when compared to cathodic leading ones[32]. Also, the electrically evoked auditory brain response (EABR) also has shown that the brainstem will respond to the anodic-leading stimuli faster than to the

cathodic-leading[33]. The response time difference of both methods are similar, basically up to 400 μs[33].

There are some clues as to the causes for these differences. We are aware that for patients with hearing loss, especially those who have lost hearing for a long time, the peripheral dendrites of spiral ganglion neurons will largely be degenerated[34]. In contrast, the animals in experiments are mostly acutely deafened, so their peripheral dendrites will be intact. The anatomy is shown in Figure 1.5. In addition, researchers have noted that in neural signal transmissions, when the signal is going through the soma from peripheral to central axon, it will meet a delay caused by the soma of around 150 to 400 μs[35]. This somatic delay is just of the same level as the response time difference to different polarities of stimulation in brainstem or ECAP.

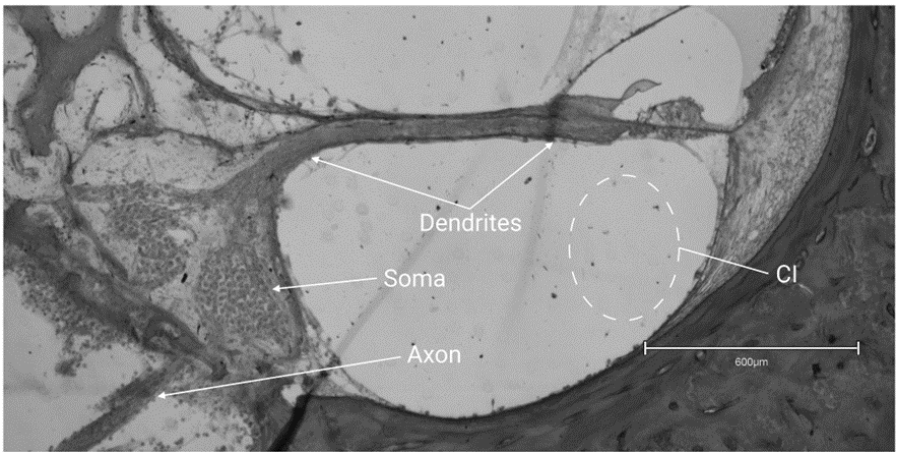

Figure 1.5: Histology slice showing dendrites, soma, and axon. The dendrites are in the spinal lamina between scala tympani and scala vestibuli. Soma is (considered) mostly in Rosenthal's canal. Central axons are in the internal auditory meatus. The dendrites in this slice are clear and complete, indicating normal hearing.

One explanation for the polarity effect that has gained wide traction[36,37] is that the anodic-leading stimuli tend to stimulate the central axon of the spiral ganglion neurons, while the cathodic-leading ones tend to stimulate the peripheral parts. Recent research has already shown that the polarity sensitivity of patients could be used as an indicator of their neural health[38,39]. However, we still have to answer the question as to why the polarity effect happens.

One explanation, originally put forward in the late 1990s, is that the polarity effect is caused by the curved spiral ganglion neural trajectory[40,41] so that the electric field has

different orientations for different parts of the neuron. The electrical field in these papers is calculated as a much-simplified homogeneous field. However, this calculation might be over-simplified, and there appears to be little additional work developing this idea. More recently papers tend to believe that it is an intrinsic characteristic of the spiral ganglion neuron – its axon is just more sensitive to anodic stimuli, and peripheral is the opposite[36,42]. Such characteristic of spiral ganglion neurons could be validated using patch-clamp or other techniques if proven true; however, as of yet, no paper has reported this.

In summary, the reason for the polarity effect, together with its fundamental mechanisms, have remained unclear for decades. I propose that it is actually caused by the natural structure of cochlea and its surrounding parts. I will raise the hypothesis and provide some evidence to support this in chapter 3.

1.2.3 Clinical measurements to assess CI and patient status

Beyond applying stimulation to restore hearing, cochlear implants demonstrate promise as sensing instruments inside the cochlea. Over the years, various measures have been developed to assess cochlear implant status and the surrounding cochlear environment. This section introduces a few well-developed methods, what we can infer from their measurements and their limitations.

The mostly widely used measures are the impedance and trans-impedance measurements from electrodes. The electrode impedance can be used to detect open or short circuits, referring to electrode (or wire) damage or shortage[43]. The trans-impedance measurement, sometimes being referred as transimpedance measurements (TIM)[44], impedance and field telemetry (IFT)[45], electric field imaging (EFI)[46] or stimulation-current-induced non-stimulating electrode voltage (SCINSEV)[47] by different authors or companies, records responses from all electrode contacts on an array when stimulating each contact individually. Importantly, there is no current flowing in the measuring electrodes, so the electrode-electrolyte interface does not introduce its own complexities. The schematic is shown in Figure 1.6. The result is an n-by-n transimpedance matrix, where n represents the number of electrodes. It reflects a relatively comprehensive snapshot of electrical conditions of all electrodes and the cochlea status. It is measured routinely for patients,

and clinical software from major CI companies has automated measuring functions. To be simple, I will refer it as the EFI in this thesis.

Recent research has shown that EFI is able to detect CI implantation issues such as tip fold-overs[48] and 2 or more extra-cochlear electrodes[47]. Further attempts have been made to predict CI insertion depth in cochlea[49,50] or the electrode-modiolus wall distance[51] based on clinical datasets. Still, errors exist in these results, e.g. the predicted insertion depth showed an average error of 0.88 mm[49], and the EFI found it hard to detect only 1 extra-cochlear electrode[47]. Basically, the EFI demonstrates the electrical aspects of the CI and the fields generated but is not necessarily related to CI hearing outcomes or neural responses in patients.

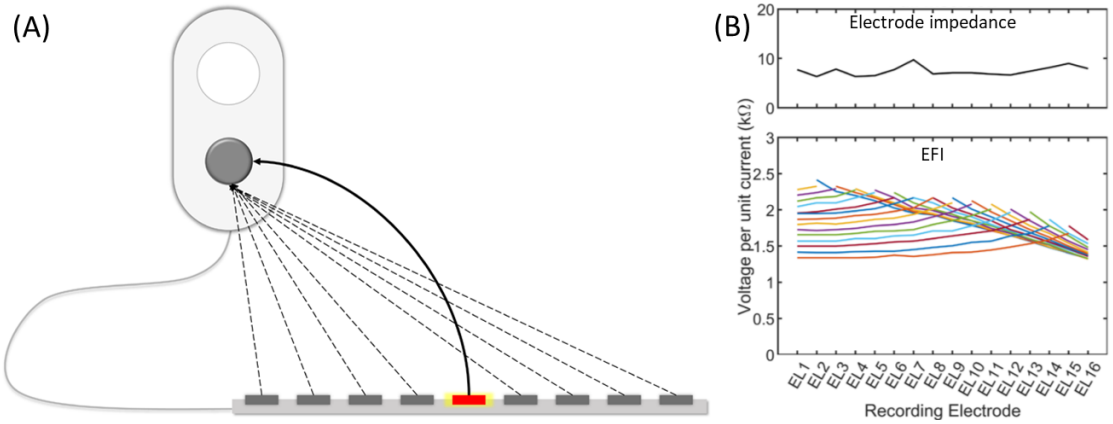

Figure 1.6: Schematic and an example of EFI and impedance measurements. (A) Impedance measurements stimulate a single electrode (red electrode in this case) with current while measuring voltage between that active electrode and the case ground (solid arrow). The voltage is divided by input current to calculate contact impedance. For EFI, voltage is also measured from non-stimulated electrodes to the ground (dashed arrows) when current is applied through the active stimulated electrode. The transimpedances (EFI) are then calculated. (B) An example of measured electrode impedance and EFI (measured in cadaver). Figures adapted from de Rijk *et al.*[47] CC BY 4.0.

Another commonly used method in clinical practice is the electrically evoked compound action potential (ECAP). ECAPs are recorded from the auditory nerve, using cochlear implant electrodes stimulation, with some forward masking methods or alternate polarity stimulation to separate stimulation artefact from nerve responses[52] and it attempts to measure the directly elicited neural responses. It is proven to be stable and requires minimal patient cooperation[31]. ECAPs have the potential, theoretically, to tell us about the spread of neural excitation from each single electrode stimulation[53]. The amplitude, width[54] and slope[55] of the spread of excitation pattern of patients derived from ECAP are

have been found to be related to speech perception scores by some investigators. ECAP has also been used to detect neural health status and dead regions (areas of missing SGNs) in patients[56]. However, as ECAP recordings are all from the CI electrodes in the scala tympani, and not the modiolus, with a relatively large electrode size and spacing, we are still unable to acquire detailed information of how populations of neurons are stimulated in the modiolus.

Imaging methods are also worth mentioning. Computed tomography (CT) is a very important technique for pre- and post-operative clinical evaluation of patients' cochlea and implanted CI positions[57]. However, due to the limited maximal resolution (0.3 mm) of typical clinical CT, it can only acquire blurry (in microanatomical terms) slices of each cochlea whose entire dimensions are only several millimetres[58]. Some higher resolution methods, such as micro-CT or synchrotron[59], can achieve much higher spatial resolution down to a few microns, but are only available for cadaveric temporal bones that have to be cut down to a small size for scanning. The scans from these methods are enough to build accurate three-dimensional (3D) models. These scans are fine enough to trace blood vessels[60], however, it is still hard to trace neurons and neural trajectories from them, although Synchrotron CT seems to be evolving rapidly. Histology slices of cochlea typically provide more precise anatomical details[61] (under the microscope), but they are hard to make 3D models out of, as they are separate slices with their own individual shrinkage and distortion during mounting and staining. Similarly, scanning electron microscopy (SEM) photos provides very fine bone, neuron and hair cell imaging[62,63], but only single images, and not in a stack, are available. The imaging methods are compared in Figure 1.7.

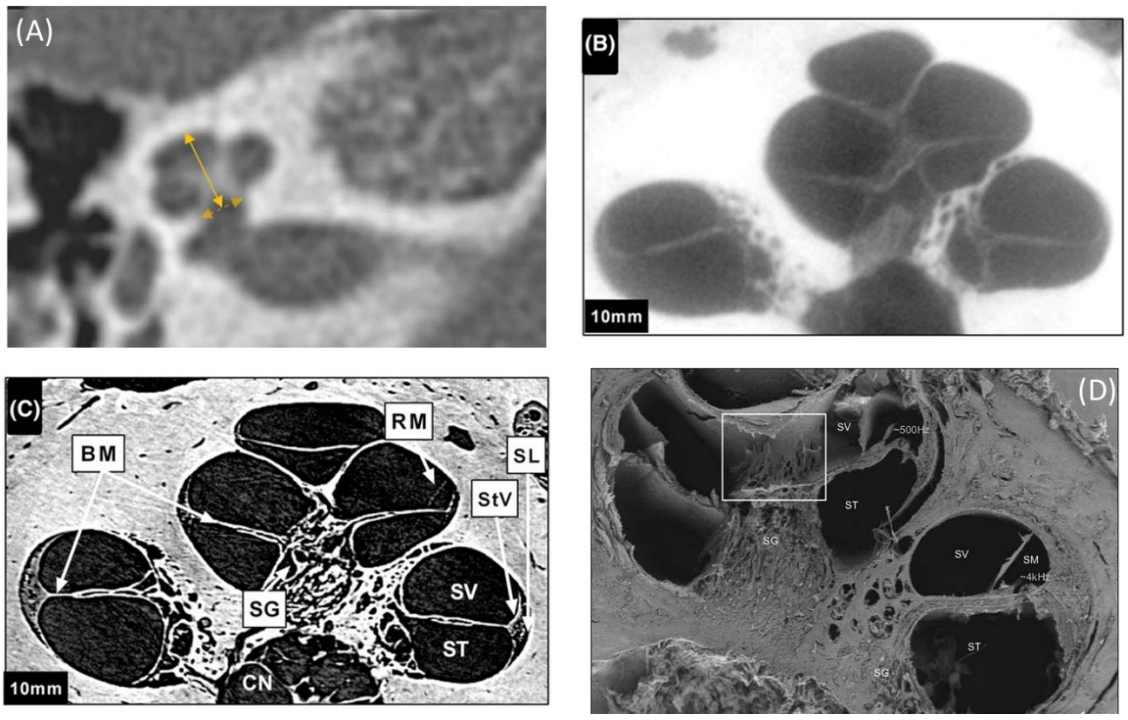

Figure 1.7: Comparison of different imaging methods on cochlea. (A) CT scan. (B) Micro-CT scan. (C) Synchrotron scan. (D) SEM image. Figure A adapted from Orzan *et al.*[64] CC BY 4.0. Figure B and C adapted from Elfarnawany *et al.*[59] Reprinted with permission. Figure D adapted from Rask-Andersen *et al.*[62] Reprinted with permission.

In concluding, current measuring approaches for cochlea and CIs still face many limitations. That is also one reason why we cannot explain many clinical phenomena – we do not have access to the direct neural tracing or activation measurements in individual patients. Alternative methods, such as computational models, are therefore used to study CIs. They will be introduced in the next section.

1.3 Computational Models and Neural Models

1.3.1 Computational models for CI and cochlea

Computational methods on cochlea have been an attractive alternative due to the above discussed challenges. Attempts to build cochlea 3D computational models were started more than 20 years ago[65-67]. Most initial work introduced a parametric spiral-shaped tube (or tubes) as the whole scala, and a central vertical cylinder as the modiolus and auditory nerve tissues[68]. Histology slices were used as validations of the size, shape and relative positions of neurons in those models[65]. A simulated cochlear implant, with realistic dimensions, was placed in the simulated scala tympani. Once one electrode is stimulated (usually by current injection), the resulting voltage in the modiolus will be calculated, so

that the voltage or electrical field applied on auditory nerve (or neurons) will be simulated[69,70]. The next step required is to simulate the resulting neural responses to these electric fields[71].

The electrical field simulation calculations mostly use finite element methods (FEM). This works by discretizing a large system into many simple, interconnected parts called finite elements[72]. The complex geometry is divided into a mesh of elements, e.g., tetrahedra or hexahedra in 3D models. In this way it can find approximate solutions to the physics system, in our case, the resultant voltage and electrical fields caused by current injection into electrodes in the structure. One thing worth noting in the cochlear simulations, or other tissue-neuron related simulations[73], is that due to the scale difference of cochlear size (or any tissue, millimetres to centimetres or more) and neuron size (microns), it is very hard to build a single mesh for both of them in a single 3D model. This results in most of the current cochlear simulations using a "2-level" approach. The first step is to simulate voltage in the modiolus, and also to define the neural trajectory in it, i.e., where the neurons should exist but having no "solid body" or specific 3D anatomical models of these. The second step is to extract the voltage at the positions of neurons to feed to separate external nerve activation models[74]. I will introduce more about the nerve models used in the next section.

More recent papers on cochlea computational models have been working on more precise or complex models in pursue of more accurate results, especially to mimic clinical measurements. One approach is to use micro-CT based cochlea 3D models[75-77]. The neural trajectories can be interpolated based on the positions of spiral lamina, Rosenthal's canal and internal auditory meatus[78]. This more accurate cochlea model could, in theory, improve the simulated results. Another approach is to include a human whole head model, as many models only include a cochlear scala model. A whole head model could provide better estimates of the correct current pathway from CI electrodes to the ground electrode under the temporalis muscle, so that the voltage distribution within cochlea area could be improved[79-81]. The head models could also be used to model real clinical scenarios[82,83] or predict what patients hearing outcomes [84]. Studies have proved that the accuracy of model geometry will affect simulation outcomes[85].

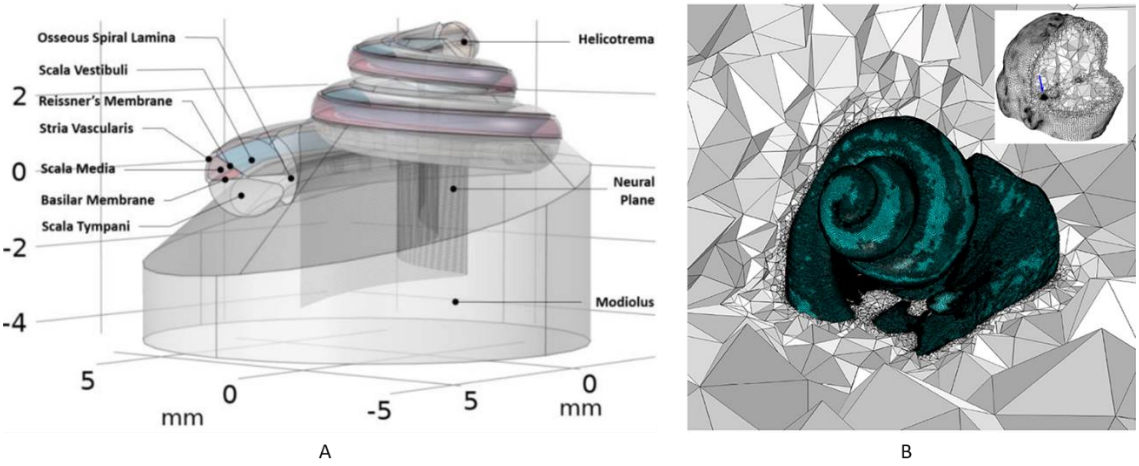

Figure 1.8: Examples of cochlear computational models. (A) Parametric based. (B) Micro-CT based. Figure A adapted from Brochier *et al.*[84] CC BY 4.0. Figure B adapted from Croner *et al.*[86] CC BY 4.0.

1.3.2 Neural models and activating function

Once we get a model of the stimulation voltage and electrical field applied to the neuron soma and axons from cochlear computational models, we will then have to predict the neuron's response to it. Neural physiology models are built based on neural excitation mechanisms, i.e., ion transportations through cell membranes and the multi-compartment structures of dendrites and axons[41]. Also note that these mechanisms are universal for all neurons, but for clarity, I will be using the "auditory nerve" specifically in the following chapters.

An auditory nerve cell consists of a soma (cell body), a dendrite, and an axon[87]. Dendrites are extensions peripherally along the spiral lamina, and contact and receive input from inner hair cells. Axons go from the soma through the internal auditory meatus to the brainstem. Cell bodies are mostly considered to be in the Rosenthal's canal inside the modiolus. The dendrites and axons are both considered to be wrapped in a myelin sheath, which is effectively an insulation layer. However, small unmyelinated gaps are periodically distributed along the axon or dendrites, called the nodes of Ranvier, which separate the myelinated axons or dendrites into multiple compartments[88]. Stimulation-induced voltage difference across the unmyelinated membrane will drive ions transfer through cell membranes at the nodes or the unmyelinated soma area, which will induce action potentials[89]. The details are shown in Figure 1.9. Different auditory nerve models will use different parameters for cell morphology, compartment length or ion conduction parameters to calculate neural responses[88], however, the mechanisms are overall similar.

Please note Figure 1.9 only shows the circuits on the unmyelinated nodes, which are more "straightforward" to understand. Some nerve models only consider this[90], but other nerve models will also consider the voltage on the myelinated compartments[88]. However, the deductions of functions below hold similarly for both cases.

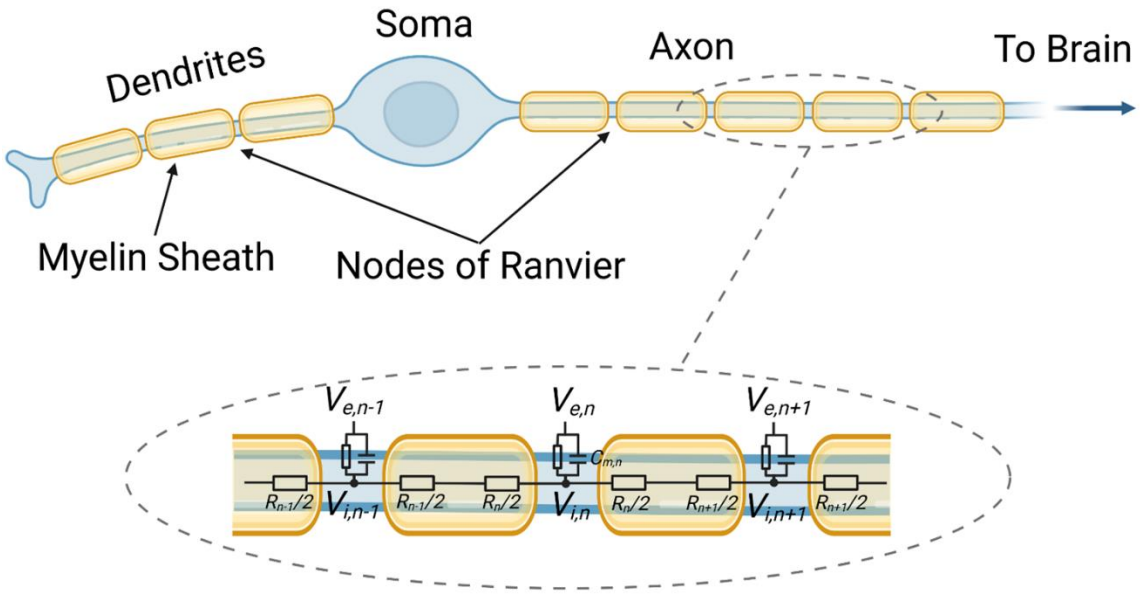

Figure 1.9: Illustration of myelinated compartments and circuit model. The upper part shows dendrites, axon, and the nodes of Ranvier. The lower part shows the circuit model among 3 nodes. Please note, to simple, this figure only shows the circuit model of unmyelinated nodes. Figure made with Biorender®.

The concept of the "activating function" has been extracted from the nerve models[41] as a much easier tool to work with, in order to assess neural activation. It considers the applied voltage of each compartment (or unmyelinated node) along dendrites and axon using a circuit model and then predicts how the extracellular voltage would affect the (trans)membrane potential[40,41], and therefore induce activations of transmembrane ion channels and neural excitation or inhibition[91]. At the *n*th compartment or node, the relative transmembrane potential at *n*th node V_n defined as:

$$V_n = V_{i,n} - V_{e,n} - V_{rest} \tag{1.1}$$

and the change rate of V_n is modelled to as[41]:

$$\frac{dV_n}{dt} = \left[-I_{ion,n} + \frac{V_{n-1}-V_n}{R_{n-1}/2+R_n/2} + \frac{V_{n+1}-V_n}{R_{n+1}/2+R_n/2} + \frac{V_{e,n-1}-V_{e,n}}{R_{n-1}/2+R_n/2} + \frac{V_{e,n+1}-V_{e,n}}{R_{n+1}/2+R_n/2}\right] / C_{m,n} \tag{1.2}$$

where $I_{ion,n}$ is the ionic membrane current at *n*th compartment, R_n is the axoplasmic resistance to the adjacent compartments, $V_{i,n}$ is the intracellular potential at the nth compartment $V_{e,n}$ is extracellular potential at *n*th compartment, $C_{m,n}$ is the membrane

capacitance. V_{rest} is the neural resting potential. This change rate is activating neurons at the *n*th compartment.

If the neuron is in the resting state before a stimulation is applied, the ionic membrane current ($I_{ion,n}$) will be considered as 0, and the intracellular potentials of all nodes will be equal. When considering the most direct stimulating influence, the values of the first three components in equation 1.2 will all be 0, so only the last two components will be extracted as the "activating function[41,92]" f_n:

$$f_n = \left(\frac{V_{e,n-1}-V_{e,n}}{R_{n-1}/2+R_n/2} + \frac{V_{e,n+1}-V_{e,n}}{R_{n+1}/2+R_n/2}\right)/C_{m,n} \tag{1.3}$$

If the axons and dendrites are further simplified to be homogenous, the axoplasmic resistance and membrane capacitance can be expressed by the diameter d, distance Δx, conductivity ρ and specific membrane capacitance c_m, which are all constant. So equation 1.3 can be simplified as[41]:

$$f_n = \frac{d}{4\rho c_m} \cdot \frac{V_{e,n-1}-2V_{e,n}+V_{e,n+1}}{\Delta x^2} \tag{1.4}$$

This form of activating function is interestingly shown to be in the form of the second derivative of voltage along the neuron (if it is not discrete but continuous):

$$f_n = \frac{d}{4\rho c_m} \cdot \frac{\partial^2 V_e}{\partial x^2} \tag{1.5}$$

The continuous form of the activating function (equation 1.5) is employed to analyse neurons without myelinated sheaths, as the concept of "nodes" does not apply to such neurons. However, in the case of the auditory nerve studied in this thesis, all neurons are considered to be myelinated, so only the discrete form of the activating function will be utilized.

Generally, the activation function is derived from the neural model and is closely related to transmembrane potential, indicating the possibility of being activated at each node or compartment. It should be noted that some models consider the myelin sheath as a perfect insulation layer[90], while others actually consider its conductivity[41]. As the node length is tiny, the voltage at its midpoint is reasonably representative of the average voltage the whole node experiences[41]. Hence, all the voltage and distances mentioned or calculated in this thesis will be at the midpoint of each node.

Also, considering that the distances between nodes are not always constant, the activating function in this thesis is derived from equation 1.3 and 1.4:

$$f_n = \frac{d}{4\rho c_m} \cdot \frac{(V_{e,n-1} - V_{e,n})/\Delta x_1 - (V_{e,n} - V_{e,n+1})/\Delta x_2}{(\Delta x_1 + \Delta x_2)/2} \quad (1.6)$$

Also, based on activating function or transmembrane potentials, different nerve models use different parameters, size and node positions to predict neural response, so results will vary[88]. To avoid this problem, the results in this thesis will be shown as the original second order difference of voltage among nodes. After removing all the constants related to neural size etc:

$$\overline{f_n} = \frac{(V_{e,n-1} - V_{e,n})/\Delta x_1 - (V_{e,n} - V_{e,n+1})/\Delta x_2}{\Delta x_1 + \Delta x_2} \quad (1.7)$$

This is the actual simplified "activating function" I use in chapter 3.

Another point to note is that, though axon or dendrite is simplified as homogeneous fibres, the diameter of dendrites is much smaller than that of axons. So, when looking at the "activating function" in equation 1.7, the difference of activation threshold between dendrites and axons should be also considered (e.g., same second derivate of voltage applied on a node on dendrite or axon will cause a different result)[93]. Additionally, the activation threshold of the soma itself is thought to be much higher than that of axons or dendrites due to its large capacitance[41], so it is hard to stimulate.

1.4 Aims and structure of this thesis

This thesis aims to provide hypotheses on cochlear implant principles that could explain the long-standing questions mentioned in section 1.2. Specifically, the existence of the internal auditory meatus (IAM) appears to create a rapid voltage change at the interface between the modiolus and IAM. A computational model of the cochlea and head was built to understand how cochlear implants generate electric fields that activate neurons, which we are unable to measure physically in-vivo. Because of the difficulty in measuring these parameters, validating these hypotheses will for now remain as aspirational targets for the future. Some clinical or cadaveric data were used to validate the head model, as well as the whole computational method.

Chapter 2 focuses on the development and validation of computational models based on human temporal bone specimens, using recordings of voltage spreads from cochlear implants and micro-CT scans including cochlear morphology and electrode placements.

This replication of physical measurement conditions into computational models enables direct comparison and validation of the computational approach's accuracy. Focusing on three temporal bone specimens, the research aims to validate computational modelling methods for cochleae and CIs, setting a foundation for the understanding of computational accuracy in subsequent chapters.

Chapter 3 is a key part of this thesis. The full head model is built in this chapter is based on multiple different scans. EFIs calculated in the head model naturally matched human results for EFIs. The neural trajectories are defined based on the cochlear microCT/Synchrotron scans. Neural activating function patterns are then simulated for both lateral wall and peri-modiolar CIs. A difference in the activating function patterns between cathodic and anodic stimuli is found. The reasons for this can be explained by the cochlear structure, especially the internal auditory meatus (IAM), which has been ignored by most computational works to date, but is modelled and raised as an explanatory structure for clinical results in this thesis.

Chapter 4 is an extension of chapter 3, focusing on clinical applications. Based on the head model, extra-cochlear electrodes are modelled, and a possible method to detect just one extra-cochlear electrode is proposed. The results are validated using cadaveric results. Also, the open or short circuit electrodes and scalp voltages were simulated and validated by clinical data.

Chapter 5 is a proof-of-concept model proposed to study the spiral ganglion neurons (SGNs) *in vitro*. As it is hard to study the “real” response of SGNs to CIs in cochlea (beyond neural models), a physical model is proposed to mimic the voltage that SGNs will “feel” if they were in the cochlea. By using this model, we could make a simplified physical model, which we could grow SGNs on and try to mimic in-vivo conditions,

Chapter 6 summarizes the findings and discusses the significance as well as limitations. Future work is proposed on validating this hypothesis.

2 MODELLING VOLTAGE SPREAD IN BONE SPECIMENS AND VALIDATIONS WITH PHYSICAL MEASUREMENTS

This chapter establishes computational models derived from micro-CT scans of human temporal bone specimens. By comparing the results of these models with physical voltage spread measurements from identical specimens, the accuracy and feasibility of the computational approach will be assessed.

All voltage spread actual measurements, micro-CT scans performed of the human temporal bone specimens, and the segmented 3D models of the cochlea Scala, cochlear implant (CI), and conducting wires are credited as performed by Dr. Chloe Swords, another PhD student in the SENSElab, used with her permission.

2.1 Introduction

As cochleae are deeply situated within the temporal bone, challenges have been long posed in assessing CIs and further understanding how they work. Cadaveric studies can shed light on various CI outcomes, such as electrode placement[94-96] and voltage spread within the cochlea[51]. While whole human heads from cadavers exhibit CI electrical characteristics akin to live patients, extracted human temporal bone specimens provide a more tractable model for cadaveric CI research[47,97]. Due to the much easier access to the round window and auditory nerve, these specimens afford enhanced access for assessing CI insertion[98,99] and performing precise electrical measurements.

The current computational methods associated with cochlea or head models, as detailed in section 1.3.1, have predominantly been theoretical. Notably, few studies to date, if any, have sought to validate the accuracy of these computational models using actual physical measurements.

In this chapter, computational models are based on measurements from human temporal bone specimens that were performed by Dr. Chloe Swords, who recorded the voltage spread caused by the CI within these specimens by inserting wires into the modiolus or auditory nerve. Subsequent micro-CT scans capture the morphology of the cochlear Scala, the placement of CI electrodes, and the position of wires. Dr. Chloe Sword also segmented these models from the micro-CT scans. With this comprehensive data, we can construct computational models, which was my work, mirroring the conditions of the physical measurements, enabling a direct comparison to ascertain the computational approach's precision.

This research evaluates three temporal bone specimens and presents the results side-by-side with computational models. While the electrical properties of temporal bones might diverge from intact heads (discussed in chapter 3), the primary objective here is to validate computational modeling methods specific to cochlea and CIs. This endeavour paves the way for subsequent chapters, expanding our comprehension of computational method accuracy.

2.2 Models of Human Temporal Bone Specimens

Dr. Chloe Sword prepared and measured three human temporal bone specimens. These specimens, each meticulously cut into cubic shapes with side lengths approximately ranging from 30 to 40 mm, ensuring that they all included the cochleae. To assess the voltage spread by CI stimulations within the cochlear region, 10 recording wires were inserted into the modiolus area of each specimen. These metal recording wires were sheathed in insulating layers, leaving only their tips exposed for conductive purposes. For each specimen, Dr. Sword recorded the electrical field imaging (EFIs) and voltages from these 10 wires during CI electrode stimulation.

Upon completing the micro-CT scans of all specimens, Dr. Sword segmented the detailed cochlear structures: scala tympani, scala vestibuli, scala media, the locations of CI electrodes, and the positions of the 10 recording wires. The segmentation of scala tympani, scala vestibuli, and scala media was performed using an alignment-based method[58] in StradView[100] software. These segmented 3D models, along with the micro-CT scans and recorded data for each specimen, were then shared with me for the creation of computational models. The workflow for constructing models for these three specimens is depicted in Figure 2.1.

After receiving the scala models, wire models, and micro-CT scans from Dr. Chloe Sword (as outlined in step 1 of Figure 3.1), additional segmentation was performed in this study by me, to extract the bone and muscle models, completing the comprehensive model. During this grayscale-based segmentation process, the threshold for bone was set at 100, while the threshold for muscle ranged between 30 and 99. It is important to note that the segmented muscle inadvertently includes some nerve tissue, as they are indistinguishable in the scans. However, since muscle and nerve tissues have similar electrical conductivities (as detailed in Table 3.3), this overlap is not expected to significantly impact the simulation results. The porous modiolus is also roughly segmented; due to the limited resolution of the micro-CT scans, this modiolus model is an approximation (a more precise segmentation of the porous modiolus is presented in Chapter 3, utilizing a high-resolution synchrotron scan).

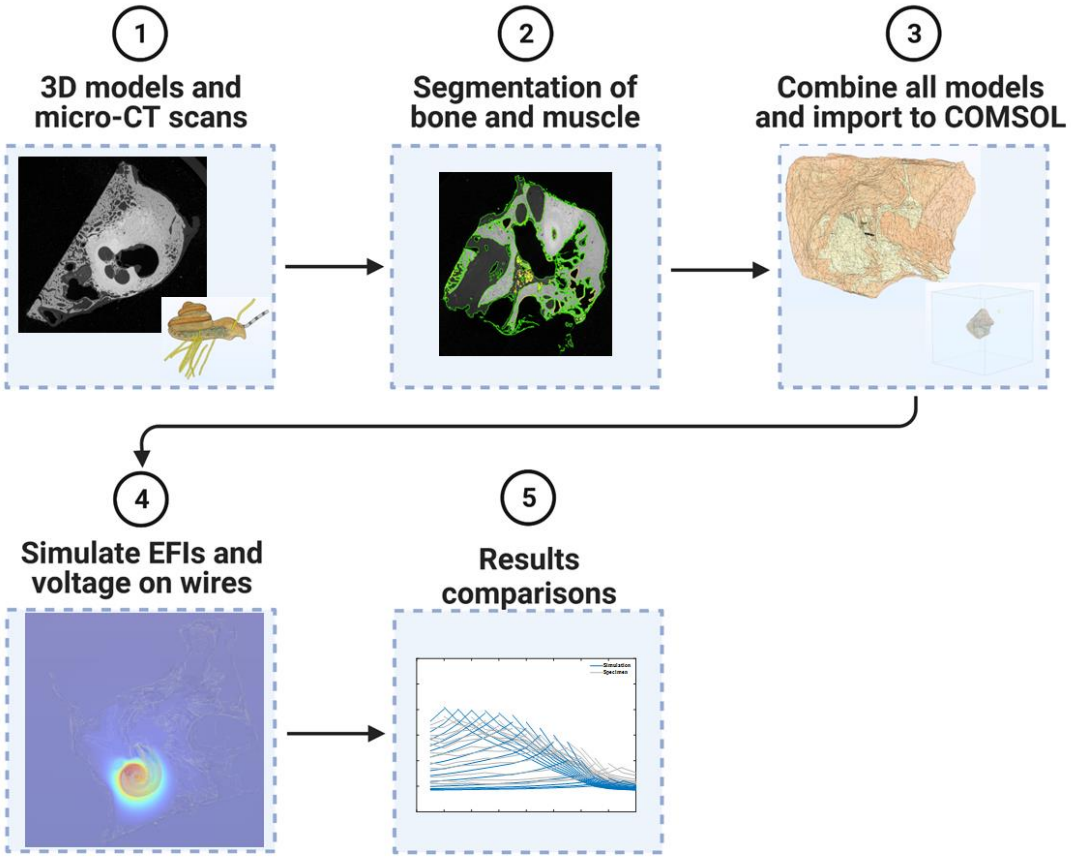

Figure 2.1: Workflow for bone specimen model constructions and Simulations. It starts with 3D models and micro-CT scans from Dr. Chloe Sword (Step 1), followed by further development and simulation by myself within this PhD thesis. The final step compares simulation results with actual specimen measurements to assess the differences.

All the 3D models are pre-processed prior to importing into COMSOL. Given that overly complex 3D models with an extremely high number of faces can hinder functionality in COMSOL, model simplification is essential. MeshLab, a free open-source software for processing 3D meshes, is utilized for this purpose. The "Quadric Edge Collapse Decimation" function in MeshLab is employed to reduce the models to a manageable number of faces. This simplification process, however, may lead to errors such as self-intersecting faces, non-manifold edges, and the splitting of non-manifold vertices. These issues are rectified using various functions within MeshLab. Following these corrections, all models become compatible for use in COMSOL. Table 2.1 enumerates the components included in each specimen and specifies the size of each 3D mesh.

Table 2.1 Overview of all the components in the bone specimen models.

Model	Specimen 1	Specimen 2	Specimen 3	Source
	Number of vertices and faces	Number of vertices and faces	Number of vertices and faces	
Scala Tympani	4999, 9994	4998, 9992	4989, 9974	Dr. Chloe Sword
Scala Media	6418, 12832	6479, 12936	6489, 12974	
Scala Vestibuli	4825, 9646	4750, 9496	4988, 9972	
Wires	2520, 5000	2497, 4998	2520, 5000	
Bone	8388, 17212	7339, 14870	7795, 16054	This own work
Muscle	7017, 14232	7114, 14360	7860, 15976	
Modiolus pores	5675, 11370	5813, 11706	5444, 11132	

During the physical measurement process, the specimens were submerged in normal saline within a container. To replicate this scenario, all bone specimen models in this study are similarly immersed in a simulated saline block (measuring 100mm × 100mm × 100mm). Additionally, a metal plate, 4 mm in diameter and 1 mm thick, is positioned on one side to serve as the ground electrode. The finalized models of these specimens are depicted in Figure 2.2. This includes the models of the 10 recording wires that were inserted into the modiolus region of each specimen, which were also accurately segmented directly from the micro-CT scans. This precise representation enables the simulation of voltage recording from these wires, facilitating comparisons with actual results. Due to page space limits, Figure 2.2 only illustrates the model of specimen 1 as a representative example. The models for the other two specimens, which are similar in their format, are provided in the appendix as Figures A.1 and A.2.

To ensure the precision of cochlear implant (CI) placements, the CI models were constructed based on the segmented CI electrode locations extracted from the micro-CT scans. Figure 2.3 presents a side-by-side comparison of the modelled CI positions and the segmented CI electrode positions from these scans. It is important to note that metal artifacts in the micro-CT scans can slightly affect the accuracy of electrode segmentation. Consequently, I made minor adjustments to the CI positions in the modelling process to ensure their accurate placement within the scala tympani.

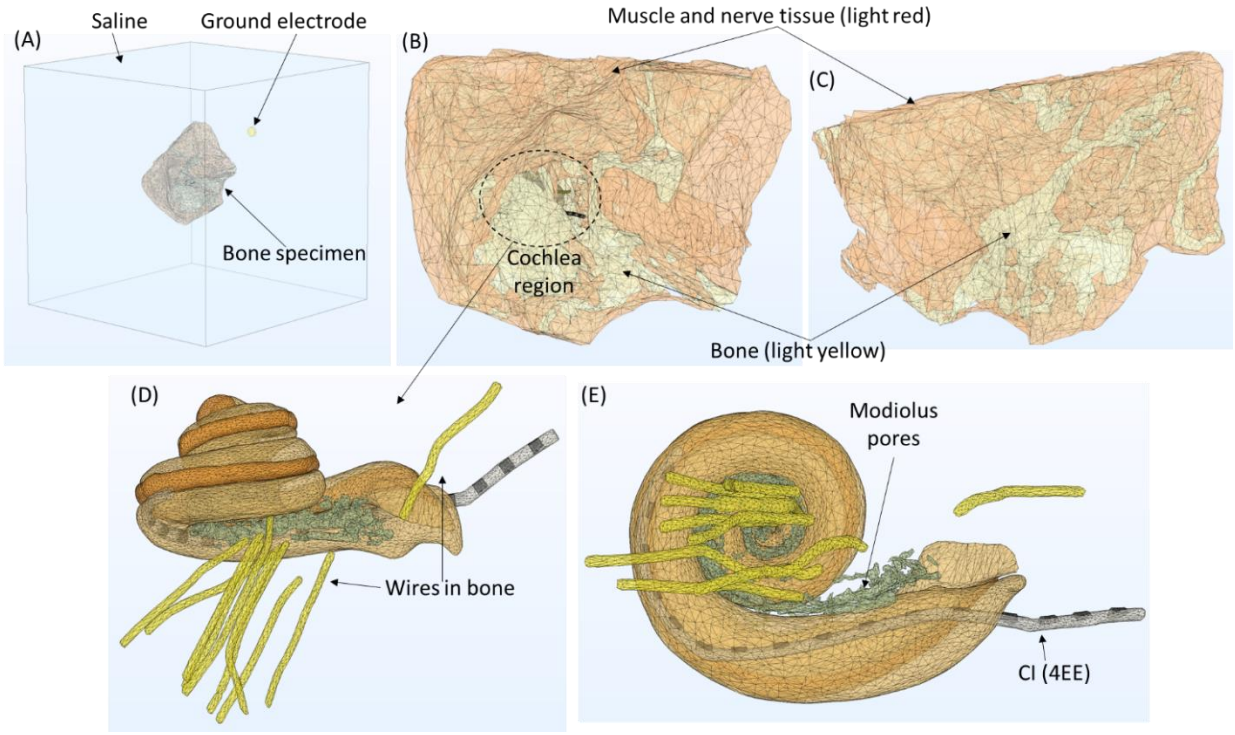

Figure 2.2: The built human temporal bone specimen models. (A) The temporal bone specimen merged by saline block to mimic the physical measurement conditions. (B) and (C) show the specimen model in 2 different points of views. The bone is mostly wrapped by muscle. (D) The model of cochlea, modiolus, 10 recording wires, and CI. The bone and muscle models are hidden. (E) The bottom view of cochlea. The CI has 4 extra-cochlear electrodes (EE) during the physical measurements, shown from micro-CT scan. This figure shows specimen 1. The rest 2 specimen models are shown in Figure A.1 and A.2.

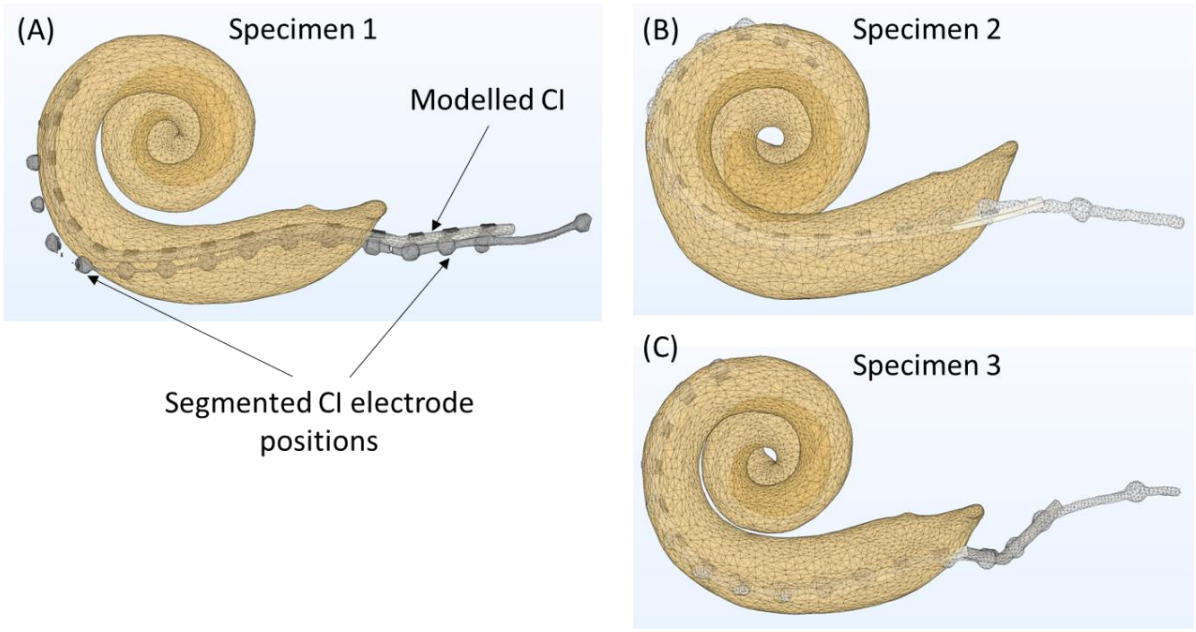

Figure 2.3: Modelled CI positions in comparison with segmented CI electrode positions. (A), (B) and (C) shows specimen 1, 2 and 3, respectively. Specimen 1 has slightly larger deviations due to metal artifact, while specimen 2 and 3 fit well.

In such small cadaveric specimens, CI insertion can be difficult, resulting in a few extra-cochlear electrodes (EEs) in all the specimens. However, in the scope of this research, which primarily aims at validating the precision of the computational method, the presence of EEs does not detract from the results. In fact, these EEs introduce a more complex scenario for simulation, which can actually be advantageous for the purpose of validation. The modelled CIs correspond well with the segmented electrode positions, including the extra-cochlear (EE) parts, ensuring that the simulated voltages accurately mirror real situations. With the complete models ready, the next phase is to simulate the EFIs and record voltage from the wires.

2.3 Simulations of EFIs and recorded voltage

In this section, the simulation outcomes for Electric Field Imaging (EFIs) and the voltages recorded by the wires are presented, with a focus on contrasting these results with the actual physical measurements. Since the computational models faithfully replicate the anatomy of the bone specimens and the conditions under which measurements were taken, the results herein offer a perspective on the computational method's accuracy.

Before simulation, the electrical conductivities of all components should be determined. Table 2.2 presents the conductivities utilized in COMSOL, along with their respective sources. Some of them are identical to those in Table 3.3. These values are commonly adopted in computational studies in this area. Additionally, it is worth noting that the simulations in this model are exclusively resistive, given the greatly increased complexities when considering the complex impedance for high frequency stimuli within all the tissue types.

In the models, muscle and nerve tissues are treated as having equivalent conductivities, as differentiation during segmentation is not feasible, and the prevalence of muscle tissue is substantially greater than that of nerve tissue. Additionally, unlike in living patients, the cochlear scalae of the modelled cadaveric specimens are filled with normal saline, reflecting the conditions during measurement where specimens are submerged in saline. The recording wires, insulated except for their conductive proximal ends near the cochlea, are similarly represented in the simulation models, although these specifics are not detailed in the table.

Table 2.2 Overview electrical conductivities in the bone specimen models.

Model	Material	Conductivity (S/m)	Source
Scala Tympani	Normal Saline	1.45	[101]
Scala Vestibuli			
Scala Media			
Saline Block			
Muscle and nerve tissue	Muscle (approximation)	0.46	ITIS Foundation database[102]
Modiolus pores			
Bone	Bone (skull)	0.018	[102]
CI body	Silicone	0	
CI electrode	Platinum	9.4E6	[84]
Ground electrode			
Recording Wire			

It is also important to note that the parameters used, taken from the most commonly accepted values, are consistently applied across all specimens in this study. To maintain integrity, I deliberately refrained from making any specimen-specific adjustments to the conductivities for "optimizations".

2.3.1 Results of EFI

For the EFI simulations, I used MATLAB scripts to individually stimulate the 16 electrodes. During each stimulation, the spread voltage is recorded at all electrodes, allowing for the calculation of the EFI as the voltage divided by the stimulation current, which is uniformly set at a convenient 500 µA. Notably, this model operates linearly, meaning that the spread voltage and current can be linearly scaled.

Figure 2.4 displays a side-by-side comparison of the simulated EFIs against the physically measured EFIs in the three specimens. In the physical measurements, to facilitate voltage recording from the wires, a small grounding electrode roughly similar in scale to the modelled ground electrode is used. This leads to non-negligible contact impedances of the ground electrodes, which vary across specimens. To align the EFI simulations (and recorded voltage) with actual conditions, surface impedances of the ground electrode in each specimen is incorporated into the model (0.003, 0.01, 0.018 Ωm^2, respectively).

These ground electrode impedances cause a vertical shift in the overall amplitude of the EFIs but do not alter the shape or span of the curves.

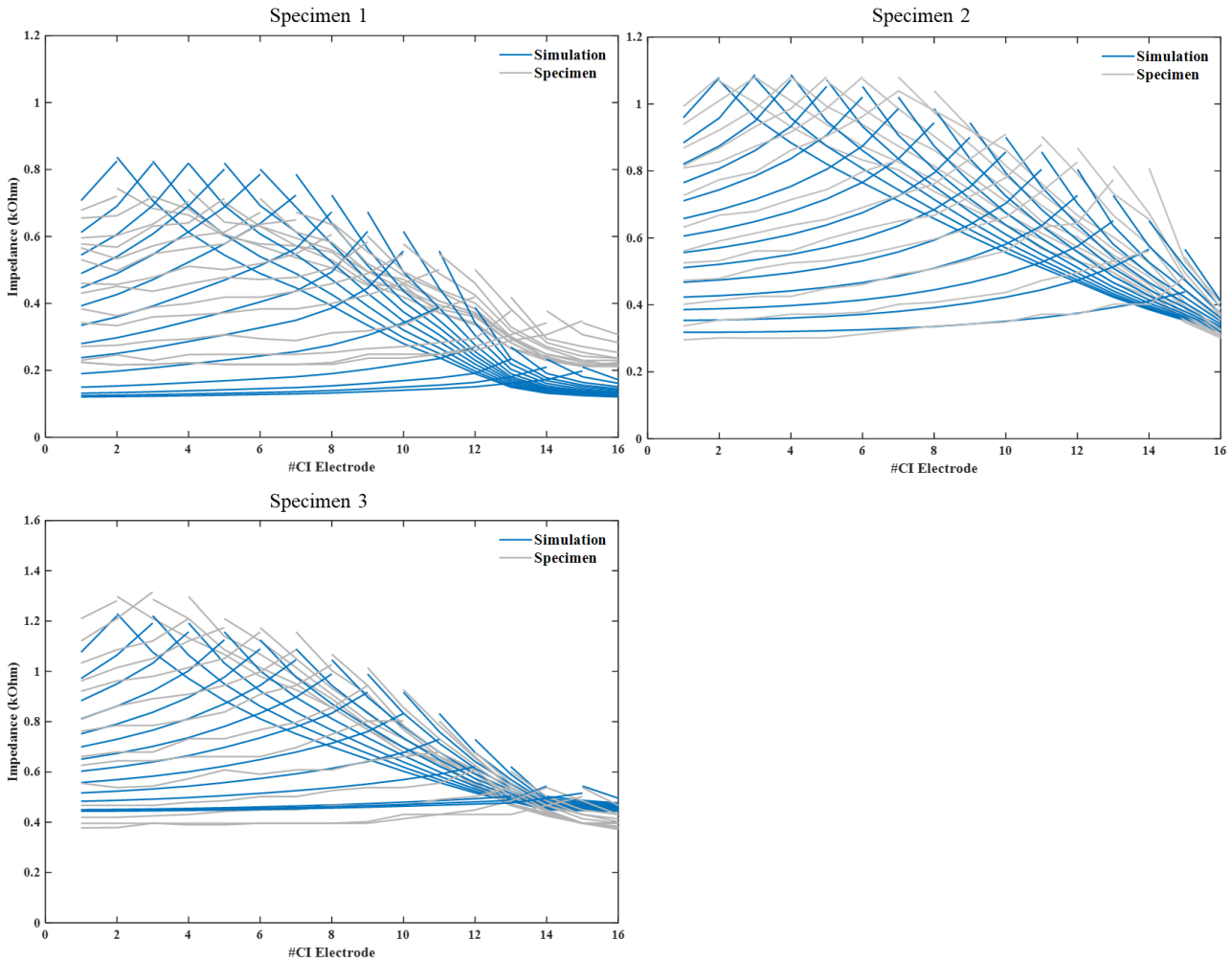

Figure 2.4: EFI Comparisons between simulations and physical measurements. All 3 specimens are shown. Specimen 1 has some deviations, while specimens 2 and 3 correlate better.

Given that the conductivity parameters are uniformly applied across all specimens, some deviations among different specimens are to be expected. Nonetheless, the EFI results demonstrate a relatively high degree of accuracy in the simulations compared to the real measurements. To assess the relative errors between the simulated EFIs and the actual EFIs, a widely used approach based on the Euclidean norm is employed:

$$Relative\ error = {Norm(Simulated\ EFI - Real\ EFI)}\Big/{Norm(Real\ EFI)} \quad (2.1)$$

While the Euclidean norm of a matrix is calculated as:

$$Norm = \sqrt{\sum_{k=1}^{N} |v_k|^2} \quad (2.2)$$

v denotes each element in the matrix.

The relative error of specimens 1, 2, and 3 are calculated as 23.0%, 9.7%, and 9.6%, respectively. This relatively high accuracy is attributed to the complexity and precision of the model, although it is important to acknowledge that bone or tissue conductivity can vary significantly among individuals. Adjusting the conductivities could potentially refine the EFIs, but that falls outside the scope of this study.

The EFI outcomes affirm the accuracy of the computational models in representing voltage spread within the scala tympani. To extend this validation to the modiolus region, the next section will present the simulated voltage data from the recording wires.

2.3.2 Results of recorded voltage from wires

To further validate our computational methods, the recorded voltages from the wires are simulated in this section. This offers an in-depth look at the actual voltage spread within the cochlear region, as a further validation of the model's accuracy.

In the cadaveric measurements, a biphasic current pulse with an amplitude of 2000 μA and a phase duration of 32 μs was used, stimulated using electrode 8, located in the middle of the CI. This current amplitude, considerably higher than typical patient usage, was set for clearer recording and reduced impact of electrical noise. The voltages were measured using the wires during CI stimulation in five modes: monopolar (MP), bipolar (BP), tripolar (TP), partial tripolar at 50% (pTP50), and 75% (pTP75). In the bipolar mode, the current was emitted from electrode 8 and returned through electrode 9. In the tripolar mode, the returned current was equally divided between electrodes 7 and 9. For partial tripolar modes, 50% (pTP50) and 75% (pTP75) of the current returned through electrodes 7 and 9, with the rest returned from the ground electrode. Given the biphasic nature of the stimulations, the peak-to-peak values of the recorded voltages were noted in all wires. This configuration was consistently applied across all three specimens.

The simulation accurately replicated all the specified configurations. When CI electrode 8 stimulated in each of the five modes, voltages were recorded from the terminals of each wire. Figures 2.5, 2.6, and 2.7 present the comparisons between the simulated voltages and the actual physical measurements from the 3 specimens. The positions of each wire are marked in each specimen from two different viewing angles of the cochlea. It is

important to note that in the physical measurements, some wires were non-functional due to defects, and therefore, their voltage readings were not included. Consequently, the data typically includes voltages from 7 to 9 wires per specimen. Wires that were excluded are indicated with an "×" in these figures. Since the voltage amplitude of bipolar and tripolar modes is significantly lower than that of monopolar mode, both linear and logarithmic scales of the voltage are displayed in the figures.

The comparison results indicate that the simulated voltages from the wires closely match the amplitudes observed in the physical measurements. While there are some inevitable deviations, the overall trends in the simulated data are relatively accurate across all five stimulation modes. This consistency further validates the outcomes of the computational methods, both in terms of EFIs and voltage distribution within the modiolus regions. Consequently, this validation provides assurance that the voltage simulations in subsequent chapters, particularly those concerning the modiolus, are reasonably reliable.

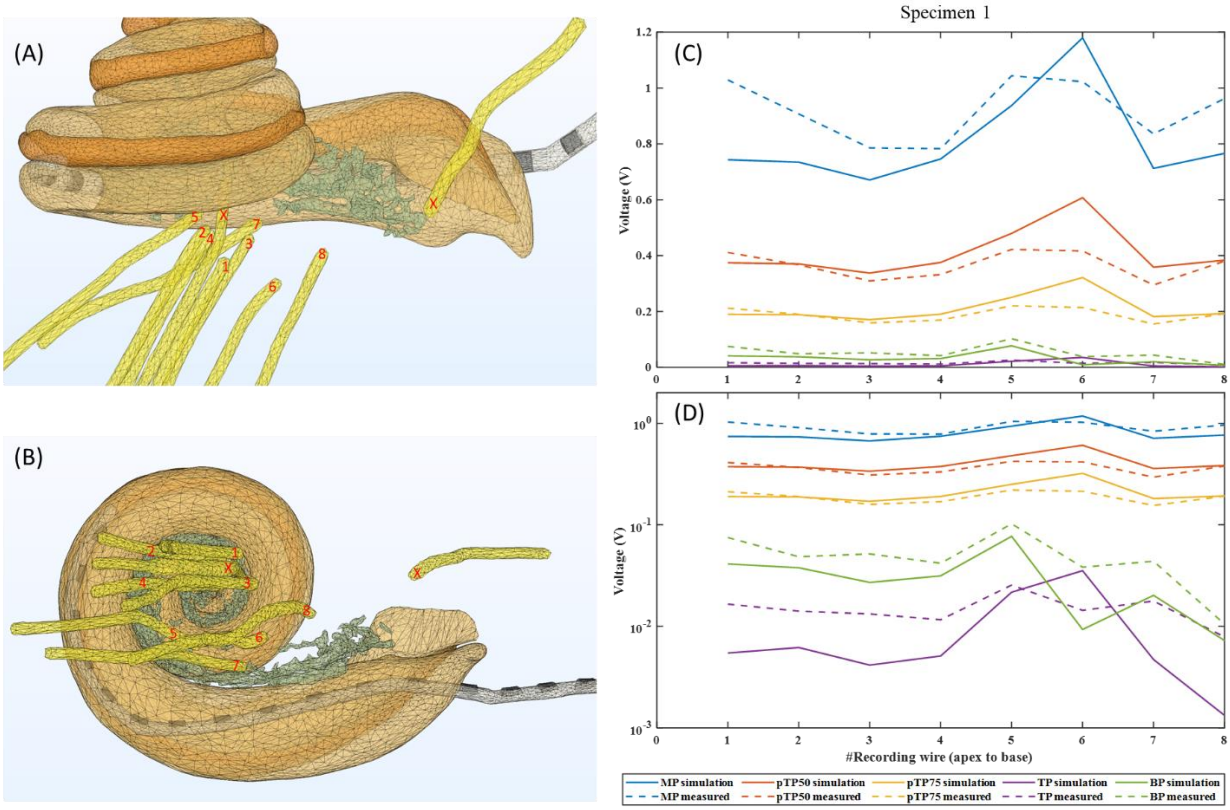

Figure 2.5: Comparisons of recorded voltages from wires between simulations and physical measurements in specimen 1. (A) and (B) show the model and the positions of wires from a side view and bottom view. Wires numbered 1 to 8 are labelled in the cochlea model from two separate viewing perspectives. Wires excluded from the analysis are marked with an "×". (C) and (D) present voltage comparisons in linear and logarithmic scales, respectively. Solid lines illustrate simulation results, and dashed lines correspond to the results from physical measurements for all five stimulation modes.

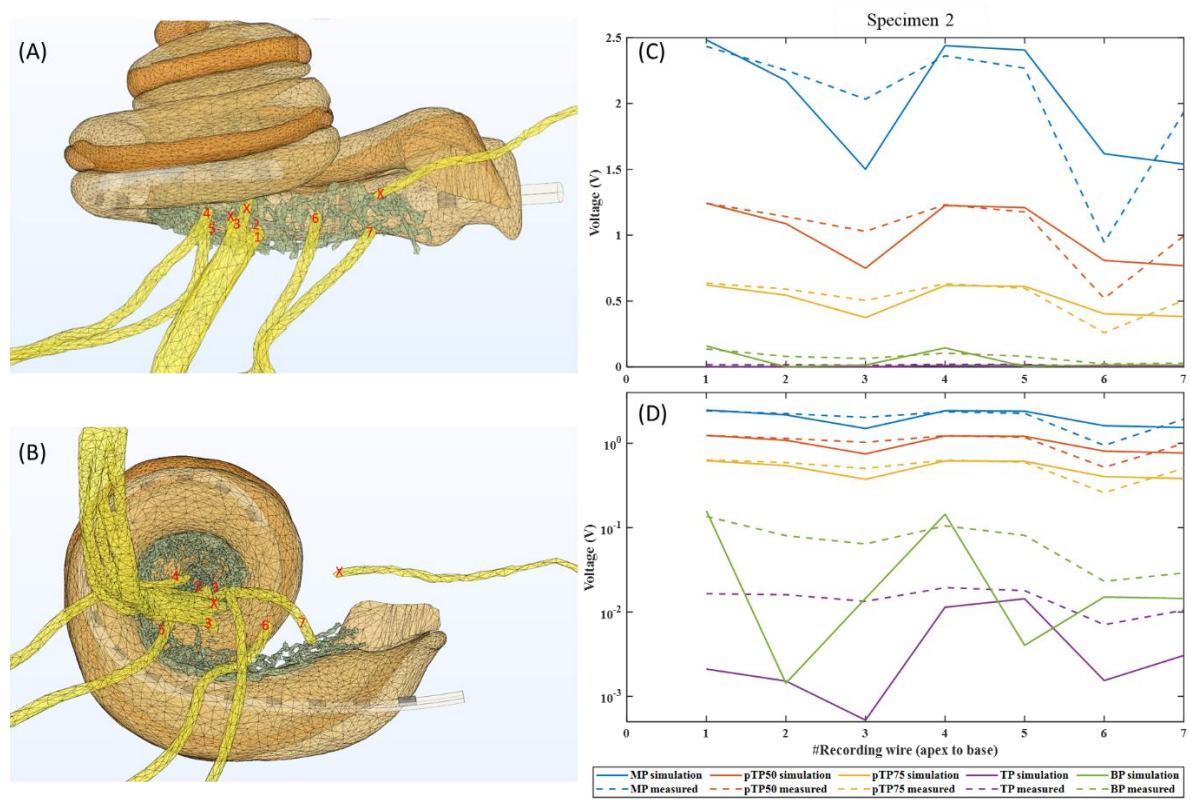

Figure 2.6: Comparisons of recorded voltages from wires between simulations and physical measurements in specimen 2. Wires numbered 1 to 7 are labelled in the cochlea model from two separate viewing perspectives. Wires excluded from the analysis are marked with an "×".

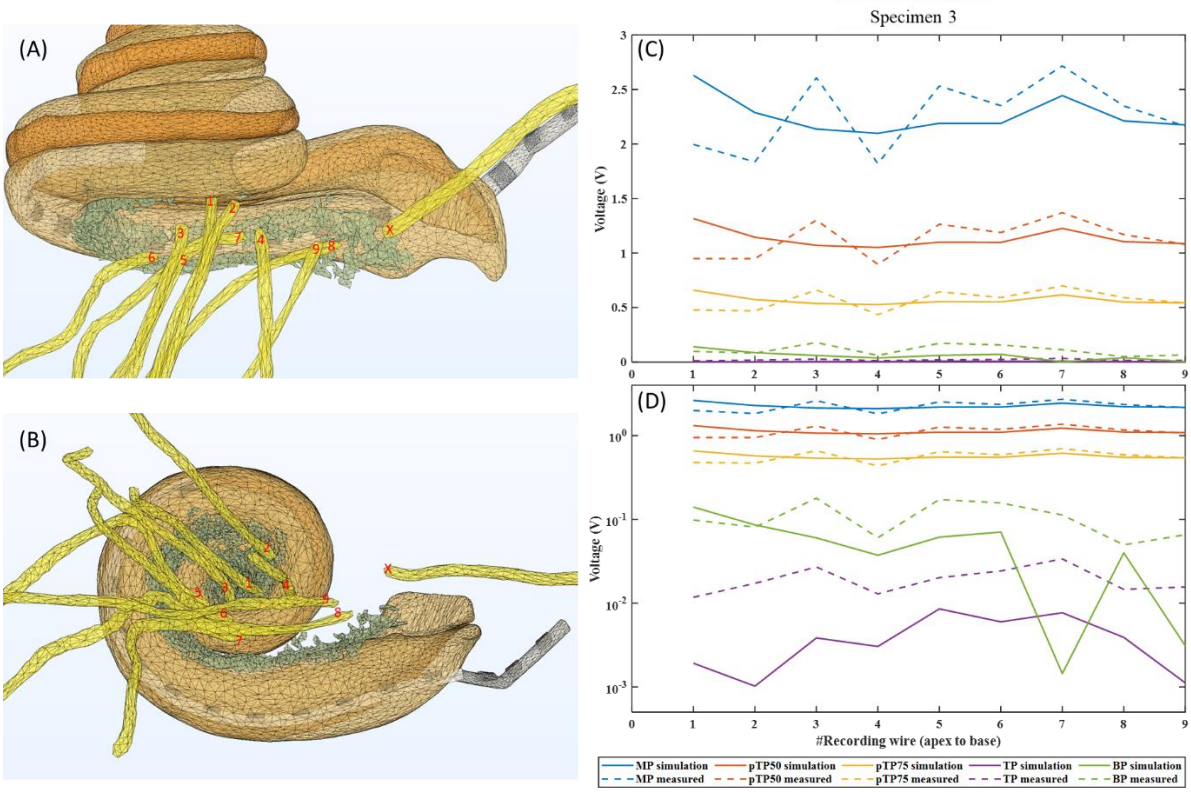

Figure 2.7: Comparisons of recorded voltages from wires between simulations and physical measurements in specimen 3. Wires numbered 1 to 9 are labelled in the cochlea model from two separate viewing perspectives. Wires excluded from the analysis are marked with an "×".

2.4 Discussion

This study is focused on validating the accuracy of computational models against real physical measurements. By precisely replicating three human temporal bone specimens and their measurement methods in simulations, direct comparisons between computational results and physical data are made possible. The study presents clear, intuitive comparisons of EFIs and voltages recorded from wires. Relying on precise computational models developed from micro-CT scans, the simulated outcomes generally exhibit a strong correlation with the physical measurements. To my knowledge, this is the inaugural effort in directly validating computational methods against physical measurements in this field.

This research lays a foundation for subsequent chapters. The same set of electrical conductivity parameters are consistently used throughout this thesis. With the validation of this method, the reliability of simulation results in later chapters is proved from one aspect. However, there are several limitations in this work.

One limitation is the accuracy of some specific model details. While the specimen modelling is largely accurate, minor metal artifacts in the micro-CT scans and the lack of photos during physical measurements lead to some estimations. These include the positions of ground electrodes, the placement of specimens in saline, and the precise amount of saline used in experiments. However, these factors are unlikely to significantly impact the results. Additionally, the contact impedances of the ground electrodes are estimated, as they were not physically measured.

Another limitation concerns the resolution of micro-CT scans. The limited resolution and contrast ratio hinder the clear segmentation of detailed structures such as the porous modiolus or nerve tissue. Consequently, this study employs approximations, such as assuming nerve tissue has the same conductivity as muscle, which might introduce further errors. In the next chapter, a high-resolution, high-contrast ratio synchrotron cochlea scan is utilized for more precise segmentations and modelling. This will facilitate the creation of accurate models of structures such as the porous modiolus.

3 COMPUTATIONAL HEAD MODEL INDICATES HOW CI STIMULATES AUDITORY NERVE – A HYPOTHESIS ON CI STIMULATION PRINCIPLES

This chapter introduces a computational full head model and the activating function patterns by CI stimulations. It proposes a hypothesis that could explain the polarity effect and why lateral wall and peri-modiolar CIs do not show an obvious difference. This chapter forms the core of this thesis.

The neural trajectory and cochlea scala models in this chapter are segmented by Dr. Chloe Swords and processed by Dr. Iwan Roberts. The synchrotron scan of the cochlea came from collaborators[60].

3.1 Introduction

Based on the validations of computational method, a further question comes up: is it possible build a precise cochlea and head model that predicts the "real" voltage profile along the auditory nerves, which we cannot obtain directly from patients, and therefore predict realistic neural activations? Computational work has been done by many researchers as summarized in section 1.3.1, however, we still did not come to a clear conclusion on how CI current spreads and how the resultant electrical fields operate.

This chapter aims to build a new head and cochlea model that:

- Contains a precise modiolus model, for the first time. All the neurons sit within the porous modiolus, and assumably the porous structure will cause fluctuations to the voltage spread on dendrites and axon, which will in theory affect the activating functions.
- Contains complete cochlea-related and surrounding structures. Looking at the detailed anatomy, many structures will affect the current path. The middle ear, which is basically air, is an insulating "wall", especially to the basal part. The vestibular part will also provide a conductive current path from the basal cochlea. More importantly, the internal auditory meatus (IAM) provides a current path from modiolus to the brain through the temperal bone. This overlooked pathway has proved to be important to neural activation in my modelling.

This chapter shows that a more precise structure that is more true to the anatomy does indeed produce different results than ones that are not. Nearly all previous works have ignored the existence of the IAM, which turns out to be a key contributor to the results and our hypothesis in this work. The detailed structure of the model is shown in section 3.2, and the results and hypothesis are in 3.3 and 3.4. These are all for monopolar stimulation, as almost all patients and companies use monopolar stimulation. Tripolar (and sometimes bipolar) stimulation is also of interest to many researchers. We also simulated this kind of stimulation in the whole head model and the conclusions are different to those for monopolar stimulation, as shown in 3.5. Section 3.6 summarizes this chapter and provides some insights to future work.

3.2 Human Head Model

The process of building models and doing simulations, from original scans to neural activation patterns, basically contains 6 steps as shown in Figure 2.1. COMSOL Multiphysics is a commonly used software for FEM simulations (mentioned in section 1.3.1). This introduction will start from the solid 3D models to the "virtually" defined neural trajectories.

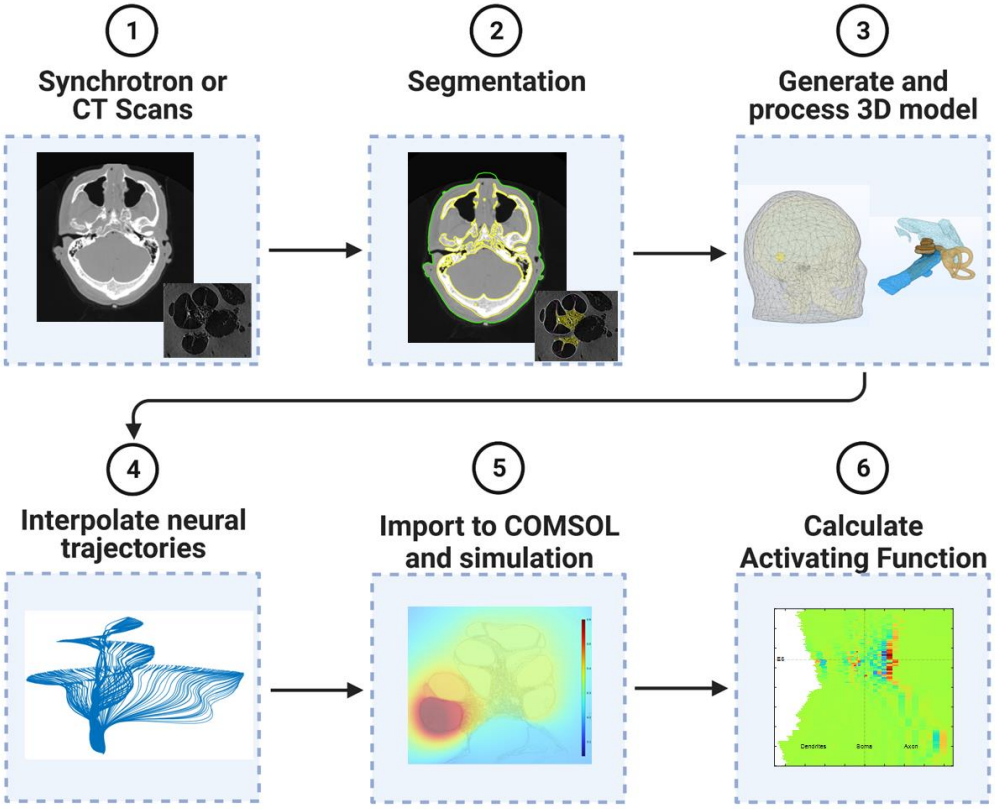

Figure 3.1: Process of building models and simulations. Scans from different sources are segmented first, and then 3D models are generated. To make the models able to work in COMSOL Multiphysics, some processing will be necessary. After calculating the resultant voltage by CI stimulation, the activating functions can be further calculated.

3.2.1 3D models of cochlea, modiolus, internal auditory meatus in head

The scala tympani, scala vestibuli and scala media models of cochlea were segmented from a synchrotron cochlear scan from collaborators[60] and processed by Dr. Chloe Swords and Dr. Iwan Roberts (also in the SENSE lab). A further modiolus model was built by laboriously segmenting the numerous pores within modiolus (this was performed by me). This is enabled by the high-resolution synchrotron scan. The pores are considered

to represent nerve tissue or other soft tissue, while the solid structures are bone. Figure 3.2 shows an example frame of segmentation of the scala and pores. The segmentation software used was Stradview[100]. The pores are segmented from around 150 slices of the synchrotron scan, and the grayscale threshold when segmenting is set to be 12. The pores that extend into the spiral lamina are also included.

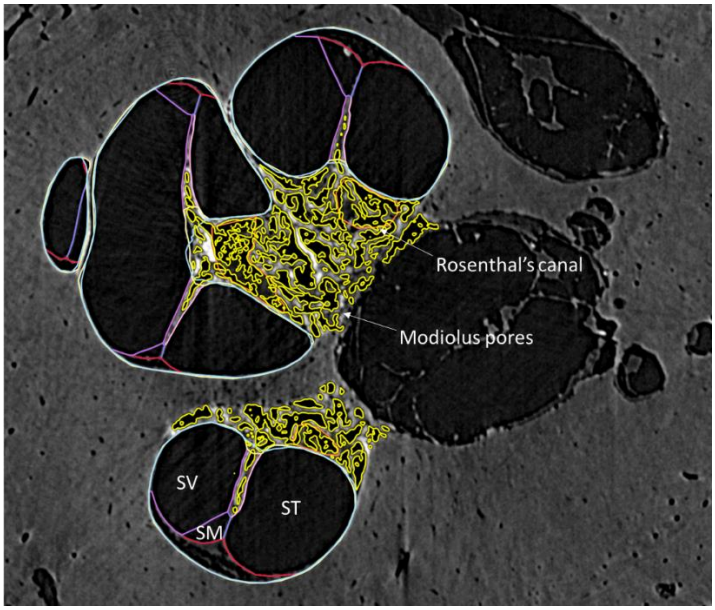

Figure 3.2: Segmentation of the scala and porous modiolus. The yellow lines are segmented pores in the modiolus. The orange lines are rough indications of the Rosenthal's canal position.

The resulting model generated for scalae and modiolus are shown in Figure 3.3. As the synchrotron is very high-resolution and only providse a narrow view field, the vestibule and semicircular canals are not included. In this model, the vestibule and semicircular canals were segmented from another micro-CT model and were then merged to the basal part of scala vestibuli based on realistic anatomy.

The next step is to include other cochlear related, connected, and surrounding components. The internal auditory meatus (IAM) connects to the modiolus from the medial side of it and allows auditory nerves to enter the cochlea. The middle ear, especially the part near round window and oral window, will also block current spread as it is mostly air. Hence, I also built these components into the model.

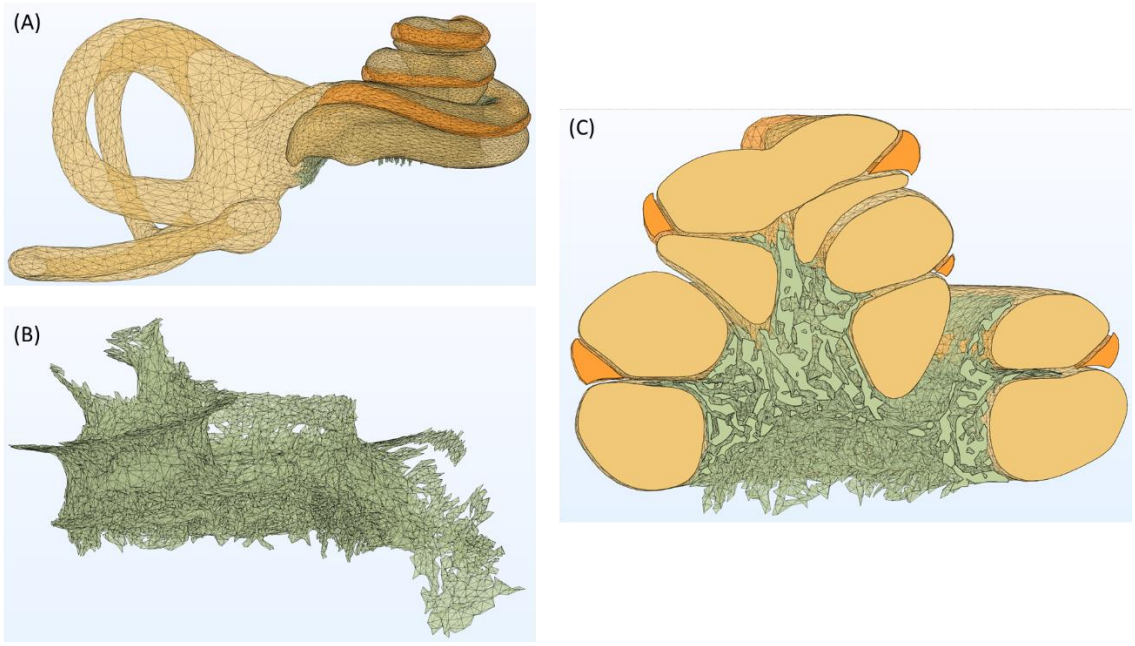

Figure 3.3: The cochlea and modiolus 3D model. (A) the whole otic capsule. (B) The pores in modiolus (nerve tissue and soft tissue). (C) A cross sectional view of the model. The porous modiolus could be seen.

The model of the IAM comes from anatomy taken from an open database[103]. The IAM model is adjusted to fit the cochlea model. The auditory nerve model is segmented from another micro-CT scan from our lab. To make it fit the IAM model, it is aligned and the redundant parts cut to make sure it sits properly inside IAM. The middle ear model is also segmented from the micro-CT scan. It only contains the part of the middle ear that is close to cochlea. It is aligned and scaled based on the positions of round window and oral window. They are added to the cochlea model and are shown in Figure 3.4.

This "aggregation" method will have some model mismatches on shape. For example, the synchrotron scan, limited by its small viewing field, cannot provide a full IAM model. The IAM from another source, however, cannot fit the modiolus pores at its top part, as it is derived from different people and the exact pores will of course vary from person to person. Hence, a merging method is used to solve this mismatch, as shown in Figure 3.5. Merging the top of the original IAM with external IAM made it fit well with the modiolus model. Similar method also applied to the auditory nerve model, which is omitted for brevity.

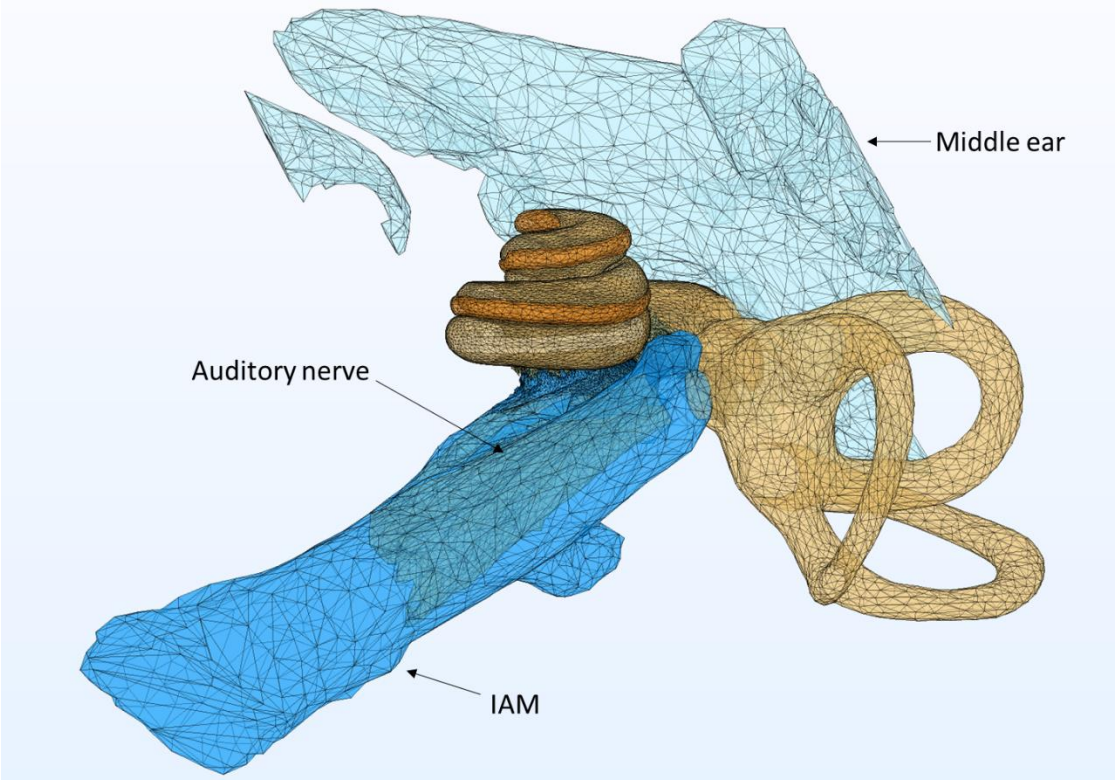

Figure 3.4: The IAM, auditory nerve and middle ear model with cochlear model. The auditory nerve is within the IAM. The middle ear contains part of it which is close to cochlea.

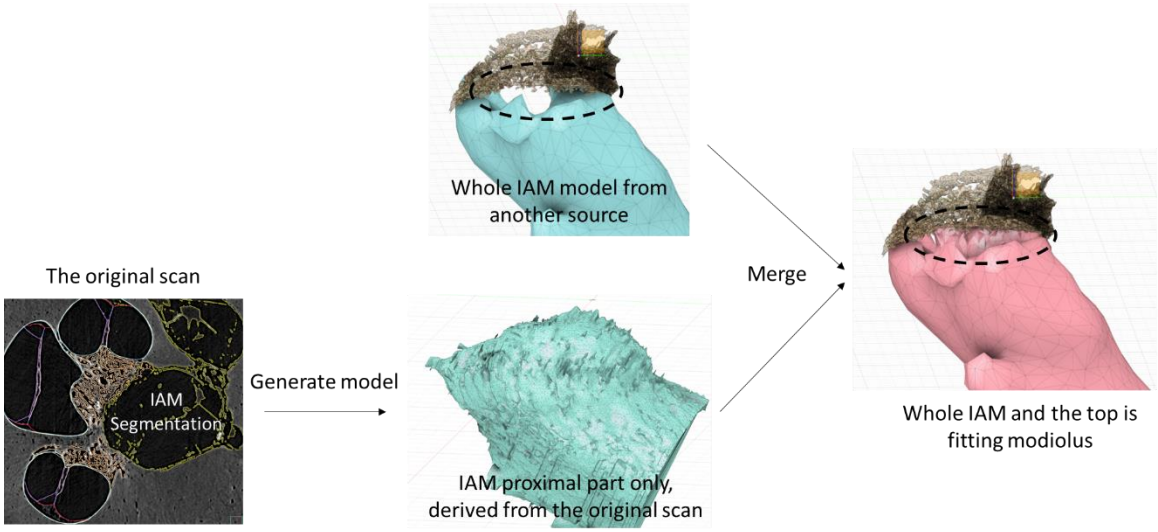

Figure 3.5: Merging method to IAM model to make it fit modiolus. After merging, the whole IAM fits well with our proximal IAM and attached modiolus.

After finishing all the cochlear-related models (shown in Figure 3.4), the next step was to build a head model and place the cochlea to the correct position. A human head CT scan was used from the Visible Human Project CT Datasets (University of Iowa, Magnetic Resonance Research Facility), which is an open access source. After segmentation, the models of scalp (head shape), skull, brain, and cerebrospinal fluid around brain are exported. The scalp is considered to include the whole skin, muscle, fat

etc. of the head. The cochlear parts are placed to the correct position based on anatomical orientation. A ground electrode is also placed beneath the scalp behind ear, as it would be in living patients. The finalized model is shown in Figure 3.6.

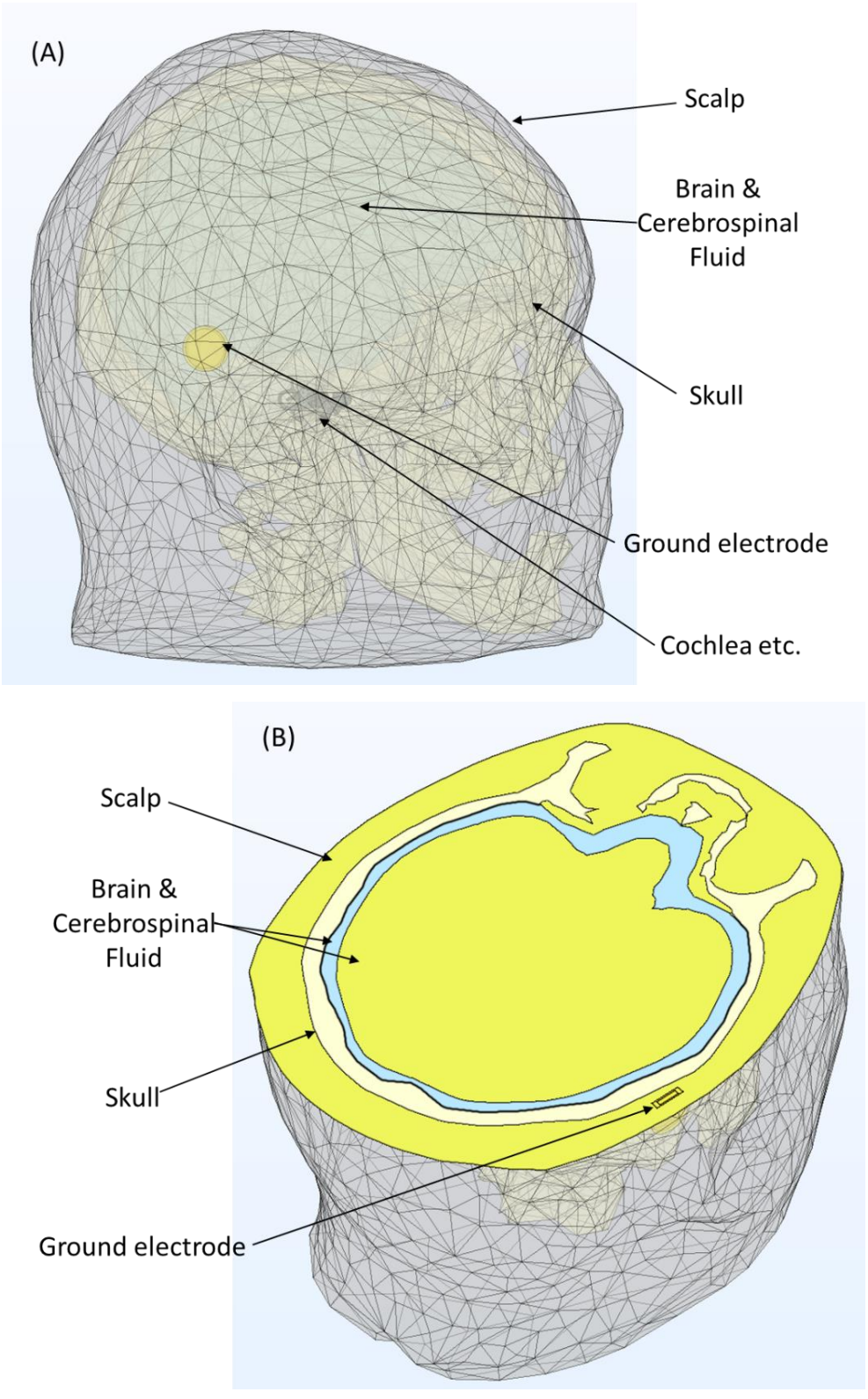

Figure 3.6: The finalized head model. (A) A side view. (B) A cross-sectional view.

The generated 3D models are then pre-processed before being imported into COMSOL. MeshLab is free open software used to process 3D meshes. As excessively complex 3D models with enormously large number of faces will make it impossible to work in COMSOL, model simplifications are necessary. The "Quadric Edge Collapse Decimation" function in MeshLab was used to simplify all the models to a reduced number of faces. During this simplification, errors of 3D models like self-intersecting faces, non-manifold edges, and split of non-manifold vertices will occur. They are removed and fixed with the functions in MeshLab as well. After these steps, all the models worked in COMSOL. Table 3.1 shows the overview of all the finalized components in this model after processing, including the size of the 3D mesh and their original sources.

Table 3.1 Overview of all the components in the head model.

Model	Number of vertices in 3D mesh	Numbe of faces in 3D mesh	Source
Scala Tympani	5002	10000	Synchrotron scan[60]
Scala Media	6690	13376	
Modiolus pores	25158	55444	
Scala Vestibuli and vestibule	6745	13498	Synchrotron scan[60] and micro-CT scan
Internal Auditory Meatus	3555	7106	Open Ear Database[103]
Auditory Nerve	3630	7384	Micro-CT scans
Middle Ear	3183	6358	
Scalp	1010	2013	Visible Human Project CT Datasets (University of Iowa)
Skull	2704	5540	
Brain	1002	2000	
Cerebrospinal Fluid	1375	2750	

Before importing into COMSOL, all the models are imported into another software application, Fusion 360, to convert from 3D mesh (.stl file) to 3D CAD format (.ipt file). This is necessary to import into COMSOL.

The last step was to build the simulated cochlear implant electrode array model in COMSOL. For this, I have referred to the datasheets of CIs from Cochlear Ltd., which provide dimensions and spacing of electrodes, including one lateral wall CI (CI622) and one peri-modiolar CI (CI632). These CIs arrays are parametric based and created in COMSOL. Their positions in scala tympani are shown in Figure 3.7 and the detailed parameters are shown in Table 3.2. Please note these parameters may not be exactly the same as the real CIs.

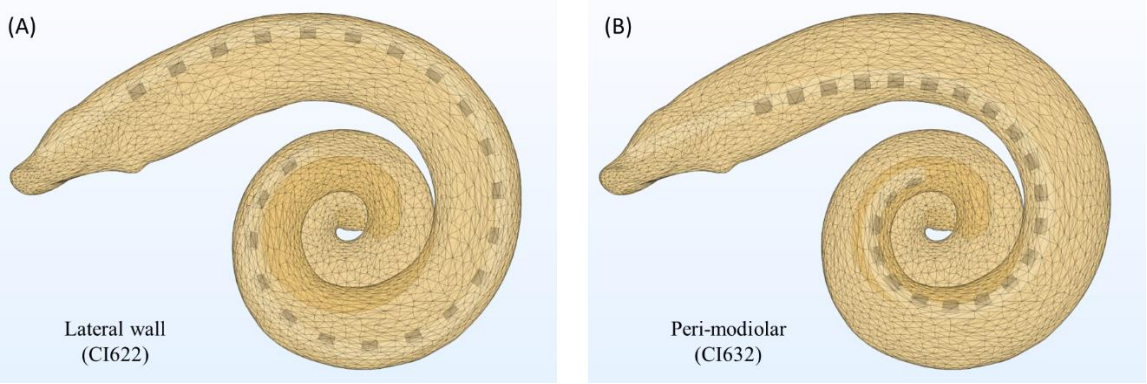

Figure 3.7: Cochlear implant models in scala tympani. (A) The lateral wall CI. (B) The peri-modiolar CI.

Table 3.2 Parameters of the CI model in COMSOL.

	Lateral Wall	**Peri-Modiolar**
Number of Electrodes	22	22
CI Insertion depth	20.8 mm	16.5 mm
CI Insertion angular depth	410°	420°
Electrode width	0.3 mm	0.3 mm
Electrodes gaping	0.57 mm	0.34 mm
CI diameter	0.3 mm × 0.44 mm	0.3 mm × 0.44 mm
Curve function (Cylindrical coordinates)	$R = 0.04e^{-2.7\theta} + 3.58e^{-0.14\theta}$ $Z = -2.756 \times 10^{-5}\theta^6 - 0.00104\theta^5 - 0.0143\theta^4 + 0.0823\theta^3 - 0.133\theta^2 - 0.0699\theta - 0.428$	$R = 0.07e^{-2.7\theta} + 2.6e^{-0.16\theta}$ Same Z function as Lateral wall

The 22 electrodes are programmed to be current sources, and could be switched on and off individually, which could be used to simulate monopolar, bipolar, tripolar cases etc.

3.2.2 Interpolation of neural trajectories

Following the construction of the head model, the subsequent phase involves the generation of the neural trajectory. Due to limitations in scan resolutions, achieving precise visualization of cell bodies and axons, which can be as diminutive, and only a few microns, is unattainable. Consequently, the only viable method to create a neural trajectory from a scan or 3D model is through interpolation based on cochlear anatomy. Simultaneously, histology slices served as valuable references for trajectory determination, as exemplified in Figure 3.8A. This histology slice comes from our clinical cochlear implant centre. Dendrites are anticipated to be located between scala tympani and scala vestibuli, with cell bodies residing in Rosenthal's canal, and all axons converging in the internal auditory meatus (IAM). Although the positions of cell bodies and axons may vary significantly, a central position is adopted for approximation.

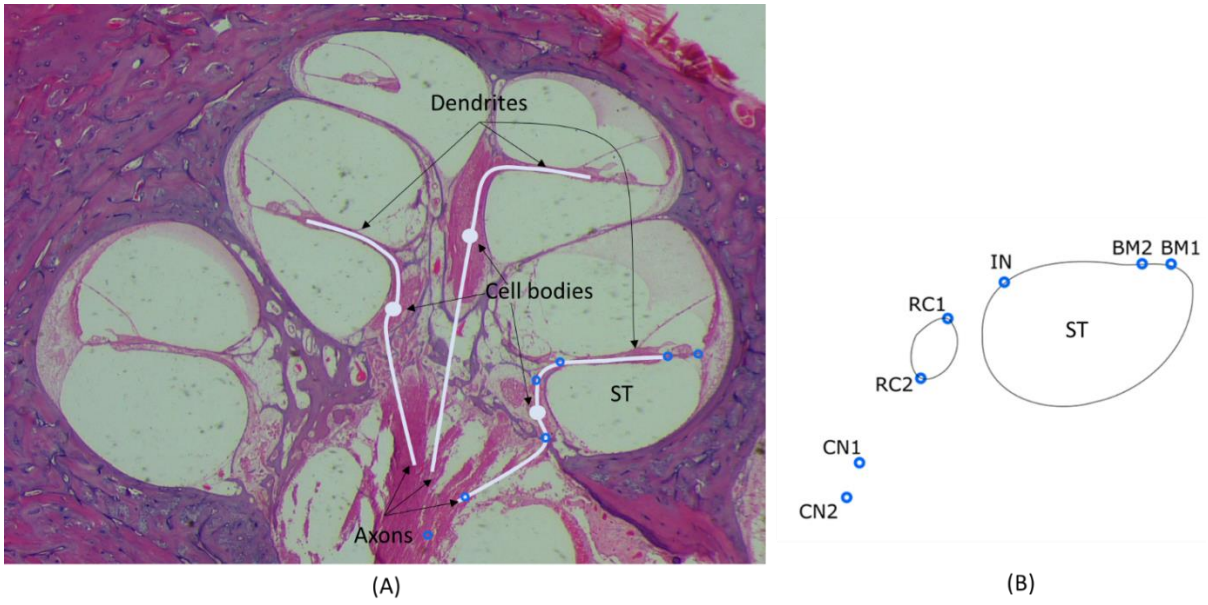

Figure 3.8: Demonstrations of neural trajectories interpolation method in a histology slice. **(**A) Neural trajectories in the histology slice, indicating dendritic, somatic, and axonal positions. (B) Identifies landmarks for interpolating neural trajectories, encompassing 2 points on the Basilar membrane (BM), the innermost edge of scala tympani (IN), 2 points on Rosenthal's canal (RC), and 2 points on the cochlear nerve (CN). These landmarks are also highlighted in Figure A.

In this thesis, Dr. Iwan Roberts created the neural trajectory using a landmark-based interpolation method rooted in cochlear anatomy, as depicted in Figure 3.8. It is crucial to note that all landmarks are segmented from the original synchrotron scan, and Figure 3.8 is illustrative of the method, not a true segmentation of the synchrotron scan. Landmarks, including 2 edges of Basilar membrane (BM), the innermost edge of scala

tympani (IN), 2 points on Rosenthal's canal (RC), and 2 points on the cochlear nerve (CN), are segmented. Employing the double exponential fitting spiral of the cochlea, described earlier, 800 points were interpolated along the cochlear spiral, each representing 1 degree. This angular definition extends from base to apex concerning the best-fit cochlear center point and the mid-point of the round window. MATLAB was employed for this process, with manual checks and adjustments ensuring trajectories remained within the modiolus or spiral lamina, avoiding entry into the scala tympani or other canals.

The derived neural trajectory is illustrated in Figure 3.9, covering an angular depth ranging from 0 (round window) to 800 degrees. Each tip of the trajectory is separated by 1 degree, culminating in 800 trajectories. A composite view presents the scala tympani, modiolus pores, and the estimated Rosenthal's canal. The diagrams affirm the alignment of the neural trajectory with the scala tympani and the modiolus pores. In the peripheral dendrite segment, trajectories pass through slender pores, which is consistent with anticipated results (as seen in Figure 3.9C).

These trajectories, consisting of 200 points each, amount to a total of 160,000 points, which are subsequently incorporated into COMSOL. After the determination of voltage dispersion in the 3D head model by COMSOL, the voltages at these spatial points are extracted. Thereafter, drawing upon neuron compartment theory and the principle of the activating function, the positions of the soma and the associated "nodes" along the trajectory are identified.

Proceeding to calculate soma positions, as illustrated in Figure 3.9D, MATLAB is employed to determine the positions where Rosenthal's canal intersects with neural trajectories. The average or midpoint of these overlapping positions is considered the approximate soma position. The finalized soma positions are depicted in Figure 3.10. These positions form a spiral curve, densely concentrated towards the apex, aligning with anatomical expectations.

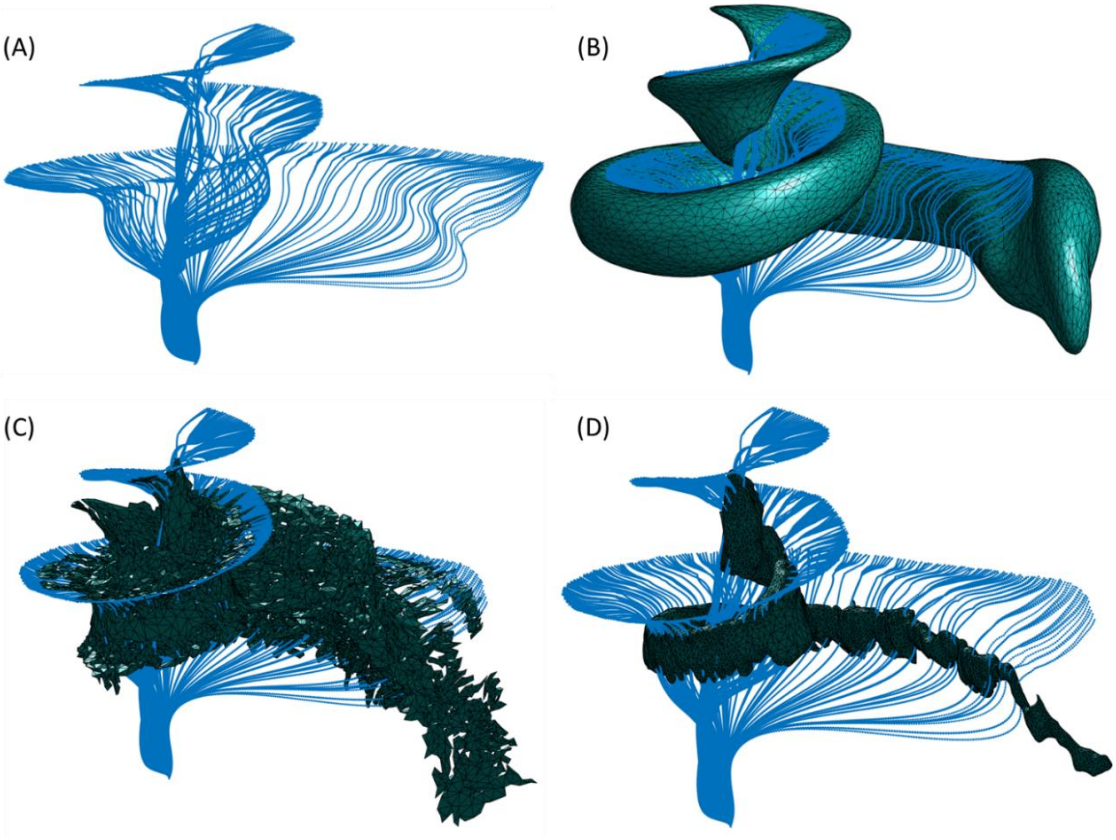

Figure 3.9: The 3D neural trajectory and cochlear models. (A) The trajectory. (B) The trajectory and scala tympani model. (C) The trajectory and modiolus pores model. (D) The trajectory and the (rough) Rosenthal's canal model.

With the soma positions determined, the positions of unmyelinated nodes can be subsequently calculated. Existing models of spiral ganglion neurons propose different node positions and intervals (as summarized in Bachmaier et al.[88], details in the supplementary material). Although these models differ in node positions, they converge in terms of node numbers. This thesis adopts the node positions from the Briaire and Frijns model[90], which includes six compartments in peripheral dendrites with scalable lengths based on the entire dendrite length. The compartment lengths in the axon are fixed, ranging from 150 µm at the first compartment to 350 µm from the fifth compartment onwards. The precise compartment lengths (before scaling) are delineated in Figure 3.11A.

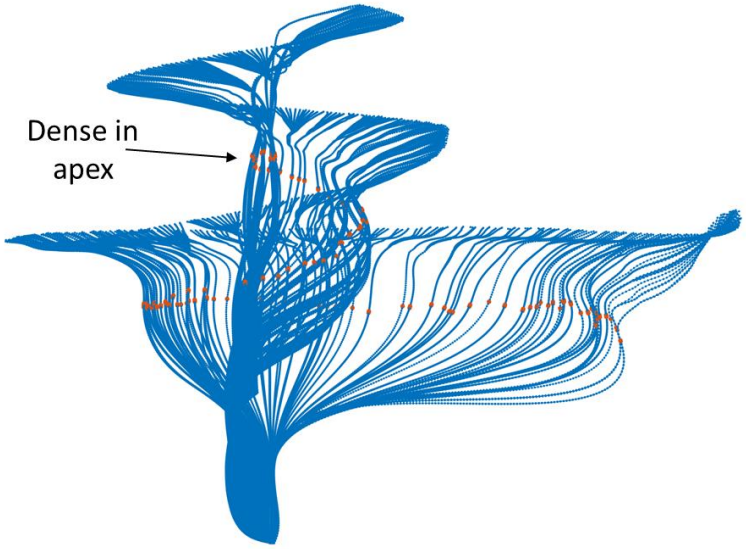

Figure 3.10: Positions of soma on trajectories. The red dots are the calculated soma positions along trajectories, showing a dense distribution at apex.

Given the variability in dendrite length from base to apex, dendritic compartments are linearly scaled to accommodate this variation while maintaining a total of six dendrite compartments. Figure 3.11B illustrates the scaled compartment lengths along each neural trajectory, ranging from the base to the apex. For instance, at the basal trajectory (~0 degrees), the 250 µm compartment is scaled to ~350 µm, while at the apical trajectory (~800 degrees), it is scaled to ~500 µm. The scaled lengths of 50 µm, 100 µm, and 150 µm compartments are also proportionally adjusted, as depicted in the figure. Notably, the shortest dendrites are observed around 400 degrees. Additionally, the node length (1 µm), pre-somatic region (100 µm), soma, and central axon compartment length remain unchanged and are not subject to scaling.

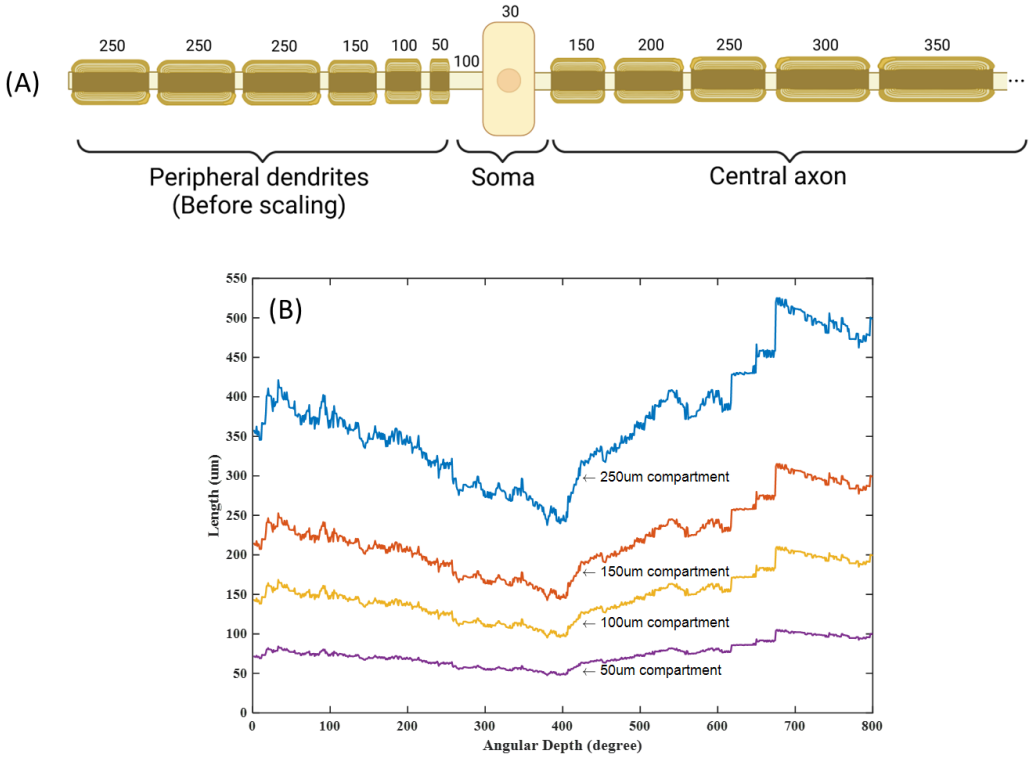

Figure 3.11: Length of compartments before and after scaling on all trajectories. (A) The original compartments length and positions in the model. (B) The scaled dendrite compartments length at different angular positions, based on the nerve trajectories in this model. The basal dendrites (or compartments) are longer than the middle part, but shorter than the apical part. Only the peripheral dendrites are scaled.

Building on this, Figure 3.12 presents the 3D positions of the "nodes" considered in this chapter, alongside the soma position. These "effective" trajectory sections are crucial for calculating activating functions. Similar to widely used nerve models[88], these "nodes" represent either the positions of the nodes of Ranvier or the midpoint of each myelinated compartment (as depicted in Figure 3.11A). Notably, the "effective" part of the neural trajectory is shorter than the entire trajectory in Figure 3.9, as it is unnecessary to consider the further parts of axons deep within the IAM. Furthermore, while each trajectory in Figure 3.9 comprises 200 points, Figure 3.12 depicts only 31 sampled "nodes" (12 in dendrites, 1 at the pre-somatic region, 1 at the soma, 1 at the post-somatic region, and 16 in the axon). Voltage sampling will be conducted at these points, and activating functions will be computed, as explained in section 1.3.2.

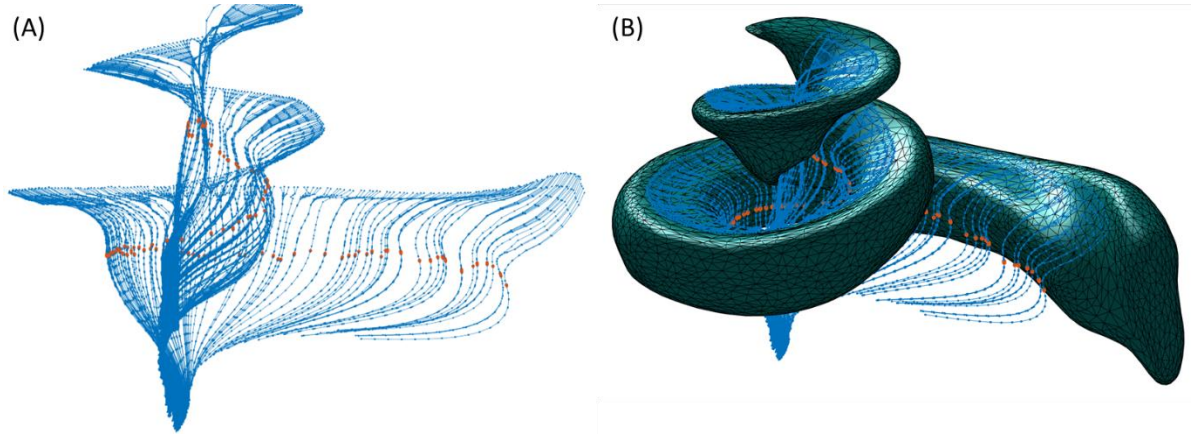

Figure 3.12: Positions of "nodes" on neural trajectory. (A) Blue points represent the "nodes," referring to the nodes of Ranvier or the midpoint of each myelinated compartment. The red dots denote the soma position. (B) Depicts the positions of nodes and the scala tympani.

With all components of neural trajectories calculated and finalized, the subsequent section involves simulating CI stimulations and examining neural responses.

3.3 Results of Monopolar Stimulations

Monopolar stimulation is the predominant method employed in CI patients. This section will initially delve into the EFI and current distribution during the monopolar stimulation, as it manifests within the 3D models and this part is independent of neuronal considerations. Following this, the activating function of neural trajectories will be computed.

3.3.1 EFI and current spread

To model the EFI and current distribution, the initial step involves identifying the electrical conductivities for every component of the model. Table 3.4 presents the conductivities utilized in COMSOL, along with their respective sources. These values are consistently adopted in computational studies. Additionally, it is worth noting that the simulations in this model are exclusively resistive, given the complexities involved in accounting for the complex impedance within all the tissue types.

Within the array of conductivities, air and silicone are considered ideal insulators, both possessing a conductivity of 0. The modiolus pores, resembling nerve tissues, are

assigned the same conductivity as the auditory nerve. As for the IAM, excluding the auditory nerve, it comprises cerebrospinal fluid.

Table 3.3 Overview electrical conductivities in the head model.

Model	Material	Conductivity (S/m)	Source
Scala Tympani	Perilymph	1.43	[78,81,85]
Scala Vestibuli and vestibule			
Scala Media	Endolymph	1.68	[78,81,85]
Modiolus pores	Nerve tissue	0.33	[78,81,85]
Auditory Nerve			
Internal Auditory Meatus	Cerebrospinal Fluid	1.8	ITIS Foundation database[102]
Cerebrospinal Fluid			
Middle Ear	Air	0	
Scalp	Scalp	0.33	[81,85]
Skull	Bone (skull)	0.018	[102]
Brain	Brain	0.375	[102]
CI body	Silicone	0	
CI electrode	Platinum	9.4E6	[84]
Ground electrode			

For EFI simulations, I have programmed the 22 electrodes to stimulate individually. During each stimulation, the voltage experienced by all 22 electrodes resulting from current spread is recorded, allowing the calculation of EFI as voltage recorded divided by the stimulation current—set at a nominal 500 µA. Notably, this model operates linearly, enabling the spread voltage and current to be scaled linearly, rendering the exact amplitude of the stimulation current non-essential.

Interestingly, when employing commonly used (or average) conductivities for the cochlear compartments, the resulting EFI closely mirrors that of real patients, both in terms of amplitude and shape. Figure 3.13 illustrates the EFI without peaks for both CI622 and CI632. The EFI of CI632 (peri-modiolar) is slightly higher than CI622, a reasonable outcome given the proximity of its electrodes to the modiolar wall. It is important to note that electrode 1 is the most apical, while electrode 22 is the most basal, unlike the numbering used by Cochlear Corp themselves.

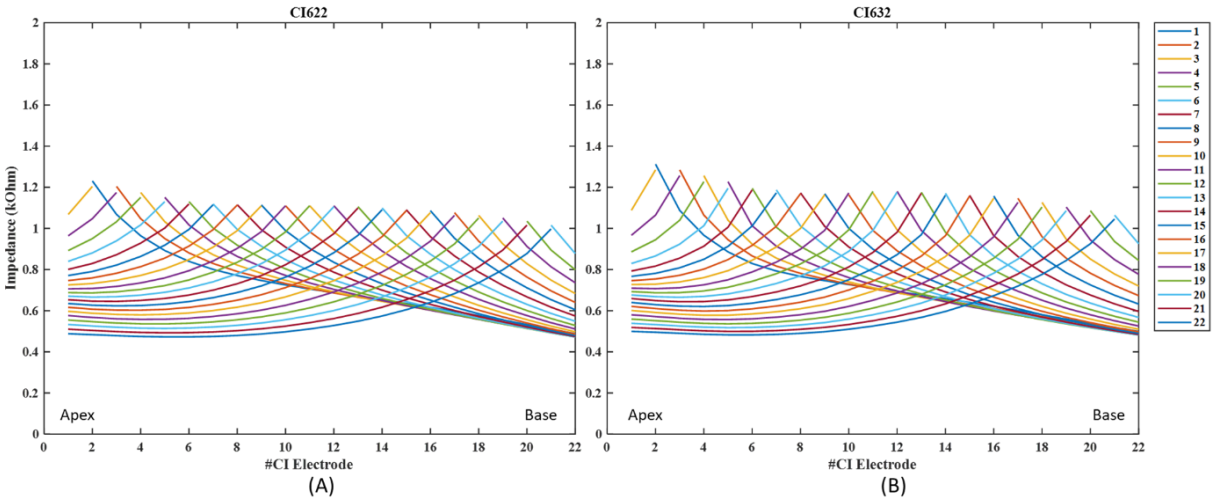

Figure 3.13: Simulated EFI for lateral wall and Peri-modiolar CIs. (A) Lateral wall CI. (B) Peri-modiolar CI. The overall amplitude, range, slope and general trend are naturally similar as patient data, which is attributable to the relatively complete models.

considering the case with stimulating electrode impedance (i.e., not the voltage on the non-stimulating electrodes- sometimes called EFI with peaks), the scenario becomes more complex. CI electrode impedance, as measured, comprises two components: the contact impedance of the electrode-electrolyte interface as now there is current flowing through the electrode and it is not just recording voltage with essentially no current flow, and secondly the impedance of the biological pathway from the cochlea to the ground electrode[50]. In reality, measuring the "pure" impedance of the biological pathway is challenging, given that all electrodes exhibit contact impedance. Similarly, the contact impedance of electrodes fluctuates based on environmental factors, electrode usage status, etc., making it challenging to measure in patients. However, in simulations, we can simplify matters by setting the contact electrode-electrolyte impedance of electrodes as 0 (although this scenario does not exist in reality), allowing us to measure the "pure" impedance of the biological pathway.

Figure 3.14 presents the EFI with peaks under the scenario of 0 electrode contact impedance. The peaks signify the pure biological impedance. Essentially the EFI traces in 3.13 are the “skirts” of these peaks not including the peak itself. In contrast to assumptions of a smooth curve[49,50], the actual curves exhibit small peaks. From these peaks, we can estimate that the biological impedance from CI to ground is approximately 1.5 to 1.8 kΩ. (This is a rough estimation, as measuring this in real cases is exceedingly challenging, leaving no avenue for validation.)

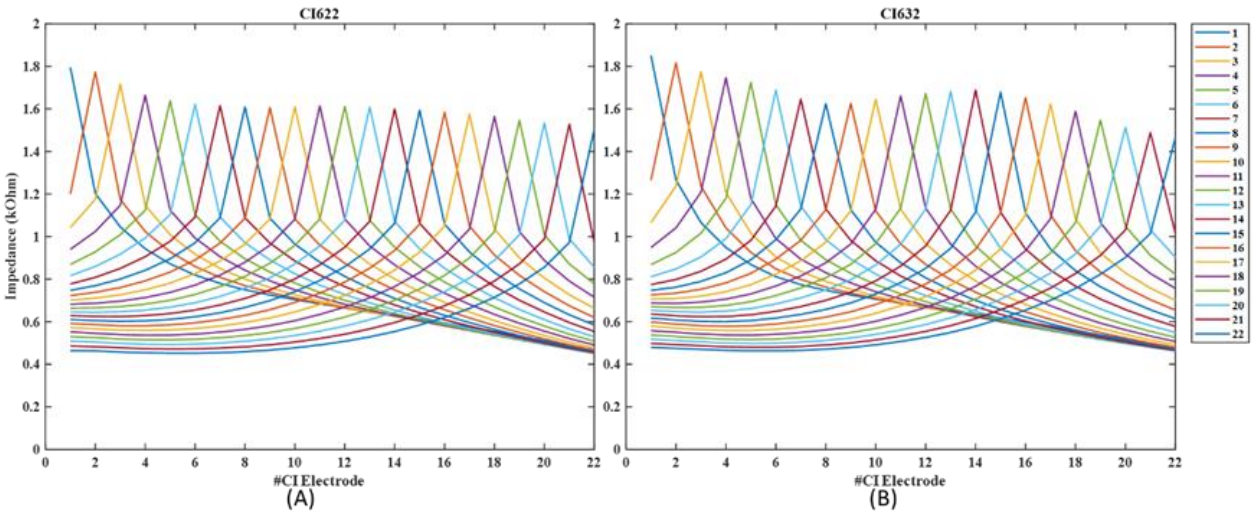

Figure 3.14: Simulated EFIs with peak under 0 electrode contact impedance. (A) Lateral wall CI. (B) Peri-modiolar CI. The peaks reflect the impedance of pure biological pathways.

To enhance the simulation's realism, the contact impedance of electrodes must be incorporated. I have adopted the average value for the normal "full" electrode impedance in patients, which is around 6 kΩ on average[104], acknowledging potential variations between CI brands or small changes post-implantation time. The surface area of electrodes is approximately 0.15 mm^2. Consequently, the contact impedance of electrodes in the model is set at 0.7 kΩ·mm^2, adding a contact impedance of around 4.67 kΩ and bringing the total electrode impedance in line with real-world values. Figure 3.15 illustrates the EFI with peaks after the inclusion of electrode contact impedance, showing a much closer resemblance to actual impedance traces with peaks when measuring EFIs.

To assess the voltage spread within the cochlea area, two cross-sectional views of voltage distribution—vertical and horizontal—are depicted in Figure 3.16, utilizing the lateral wall CI (622) as an example. Both figures include the stimulating electrode, prompting an adjustment of the voltage scale (colour bar). The maximum voltage is capped at 0.6 V to ensure clear visualization of the voltage spread. The insets provide a view of electrode voltage, with a maximum set at 3 V (CI electrode voltage).

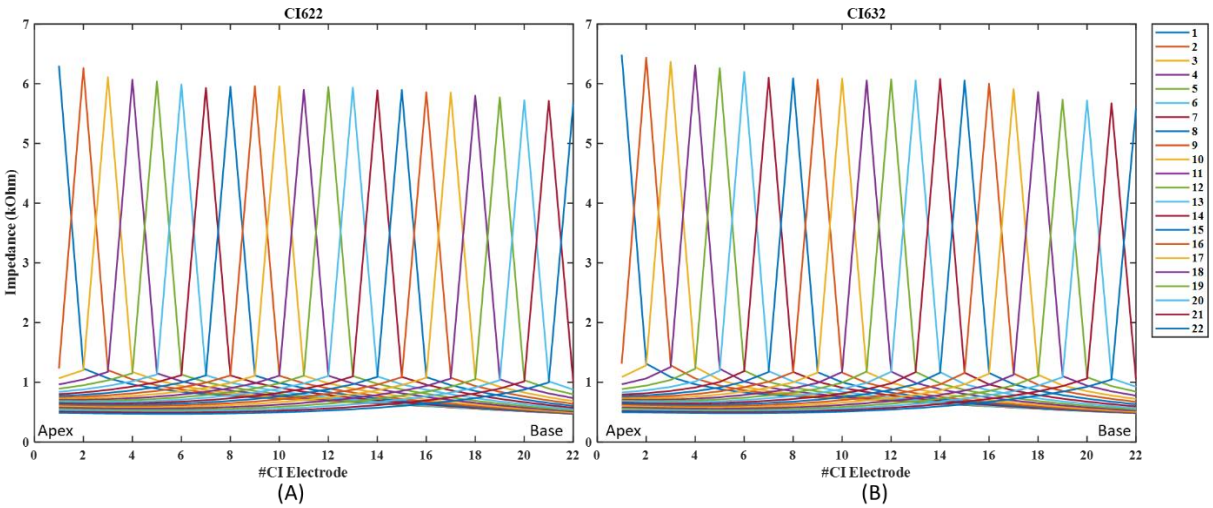

Figure 3.15: Simulated EFI with peaks after adding electrode contact impedance. (A) Lateral wall CI. (B) Peri-modiolar CI.

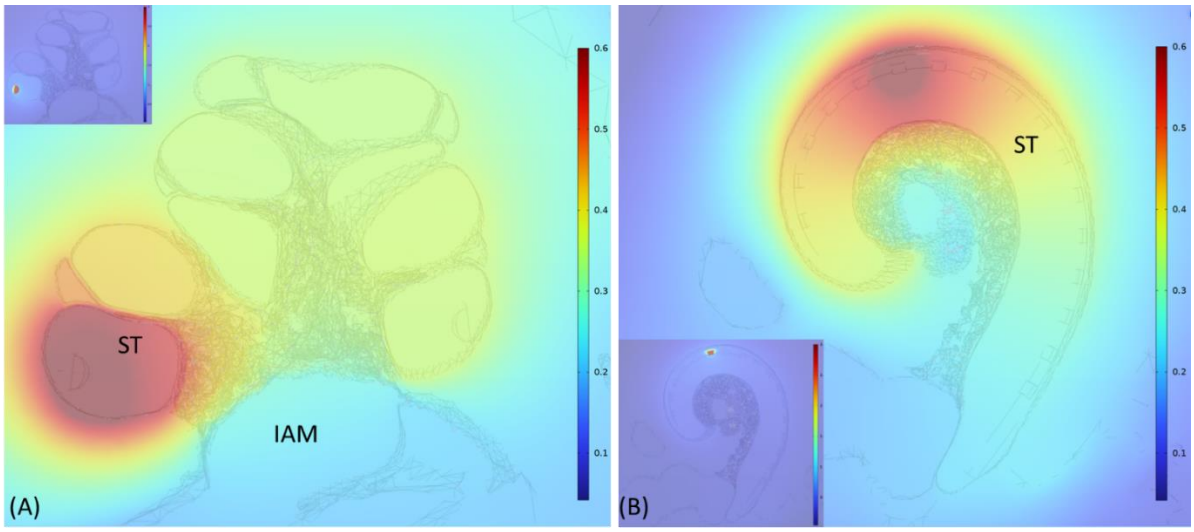

Figure 3.16: Cross-sectional views of voltage spread. (A) Vertical section. (B) Horizontal section. The outlines of the scala, electrodes, porous modiolus, and IAM are visible. The insets present another scale with the maximum voltage set at 3V (to show CI electrode voltage which is "capped" in main figures).

An intriguing question is how much current flows through the IAM and bone, which is unmeasurable physically but is feasible to show in simulations. A sphere boundary is established near the cochlea, with an IAM leading from the cochlea, as depicted in Figure 3.17. The highlighted region represents the cross-section of IAM. The current density is simulated at the surface, followed by integration to calculate the total current. When stimulating electrode 11, the proportion of current flowing through IAM is 23.4%, while the surface area occupied by IAM constitutes only 4.6% of the entire sphere. The remaining current dissipates through the surrounding bone, accounting for 95.4% of the

surface area. It is crucial to note that all components in the head model outside the sphere are included in the simulation, but are hidden in the figure to emphasize the boundary.

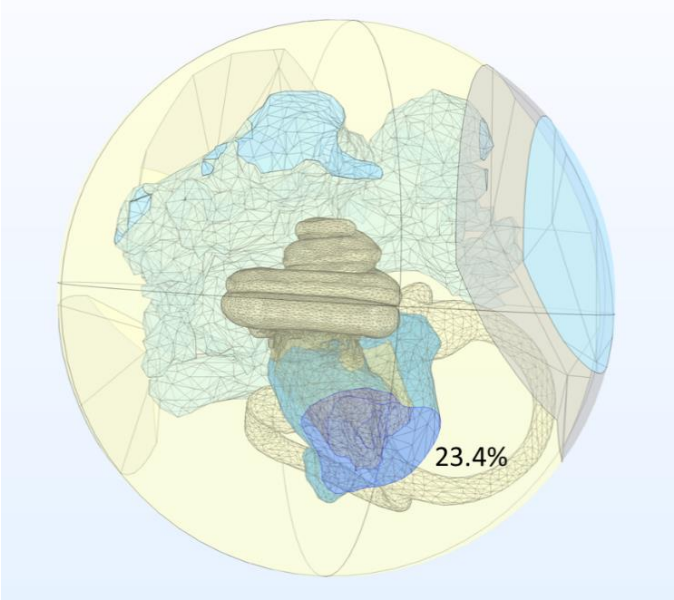

Figure 3.17: Current proportion flows through IAM. A sphere boundary is shown, intersecting with IAM (highlighted area). In total, 23.4% of the CI current flows through this 4.6% of physical area. Components outside this sphere are hidden.

3.3.2 Voltage on neural trajectories, activating functions and polarities

In this section, the interaction between the CI and neurons is explored using the neural trajectories introduced earlier. With 800 trajectories, each containing 200 points (a total of 16,000 points), the voltages on these points are extracted using the *mphinterp* function in MATLAB after importing the trajectories into COMSOL and computing. The voltage on each "node" (as mentioned in Figure 3.12) is then sampled, and the activating function is calculated based on these sampled voltages.

As a starting point, anodic stimulation is examined. Taking electrode 11 (in the middle of CI) in CI622, stimulating with a 500 µA current as an example, Figure 3.18A displays the 3D pattern of voltages on each node in all trajectories. The bold arrow indicates the region of high voltage. However, 3D plots can be challenging to interpolate, so a 2D version based on the actual trajectory length is shown in Figure 3.18B. This conversion involves aligning every single trajectory from 0 to 800 degrees on the Y-axis, essentially displaying each curved trajectory as a straight horizonal line. The X-axis represents the

distance of each node to the soma (soma position fixed at 0), with irregularities on the left side due to varying dendrite lengths. The right part shows uniformly long axons. The regions of dendrites and axons, along with the soma's position and the angular depth of the stimulating electrode, are noted.

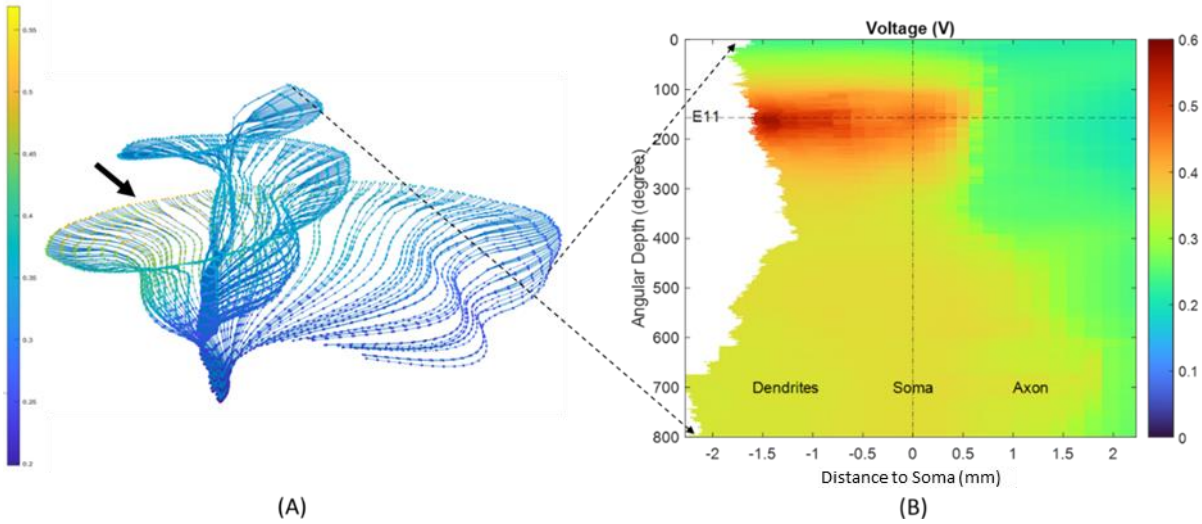

Figure 3.18: 3D and 2D views of the voltage along trajectories, assuming we are stimulating electrode 11. (A) The 3D view of the voltage on each node. The high-voltage region near the stimulating electrode is marked by the bold arrow. (B) The converted 2D plot is based on the soma position, node distance, and trajectory angular depth. All somas are aligned at 0 mm. The dendrites are longer at the apex and shorter near the base.

From the figure, it's apparent that the voltage spread is around 100 degrees, with the voltage changing rapidly at approximately +0.8 mm in this case.

Activating functions, effectively the second derivative of voltage along distance in this chapter (equation 1.7), are also plotted in the same 2D manner. To investigate the impact of stimulation polarities, this section employs both anodic and cathodic stimuli to study their influences on axons and dendrites, respectively. This study starts with the anodic stimulation. Figure 3.19 shows the voltage and activating function under different electrode stimulations across CI622 (lateral wall CI) and CI632 (peri-modiolar CI) under anodic stimulation. Due to page limits, only 5 electrodes are shown from apical to basal, respectively: E22, E16, E11, E6, and E1. Electrode 1 is the most apical, while electrode 22 is the most basal, unlike the numbering used by Cochlear Corp themselves. The stimulation current amplitudes are all set to be 500 µA. It is worth noting that the scales for the plotted heat maps of activating functions differ from base to apex.

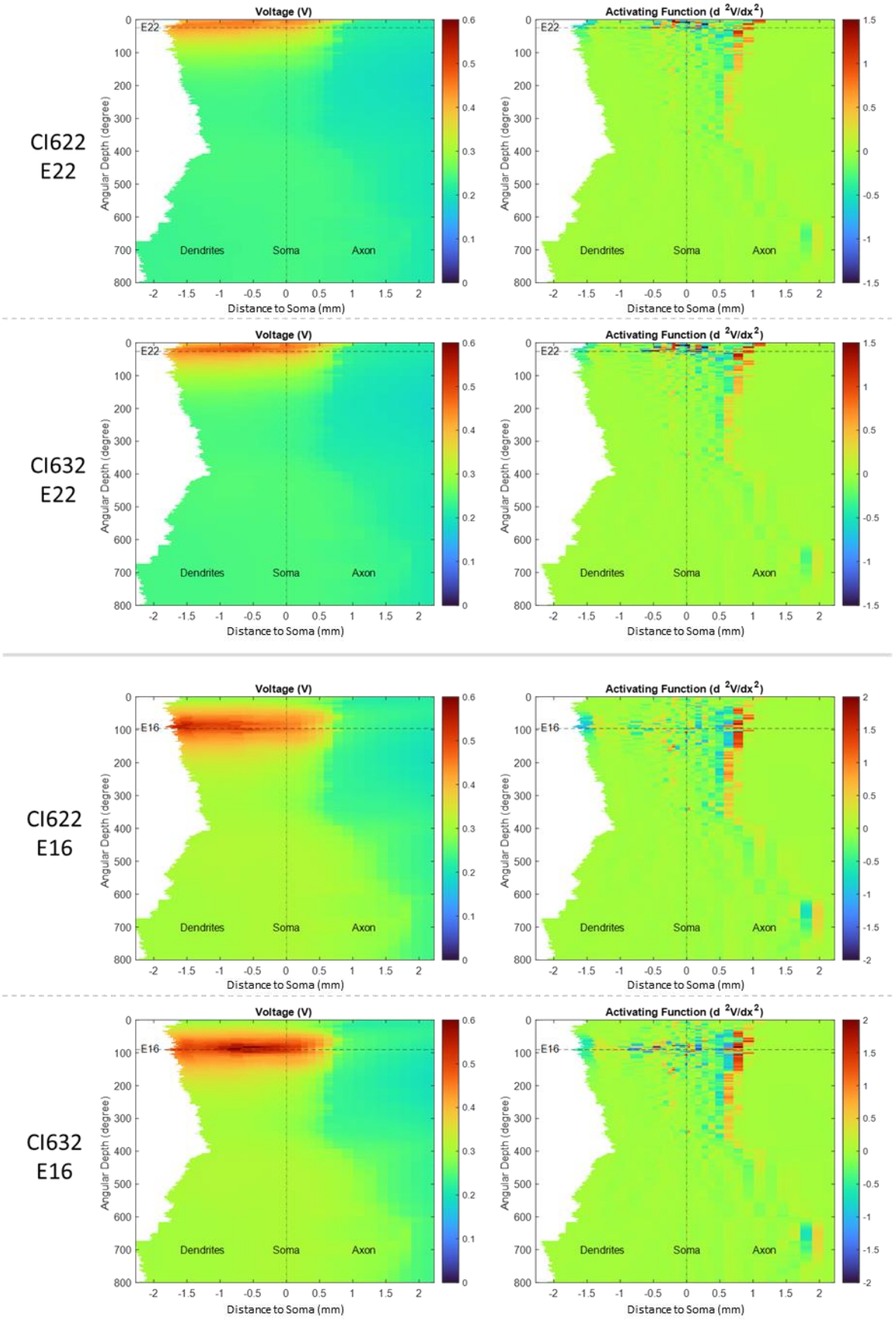

Figure 3.19: Voltage and activating functions on trajectories by anodic CI stimulations. This page shows the results of E22 (most basal) and E16 of both CI622 and CI632 for comparison. The left column is voltage, and the right is activating function. Note that the scales of the activating function are different.

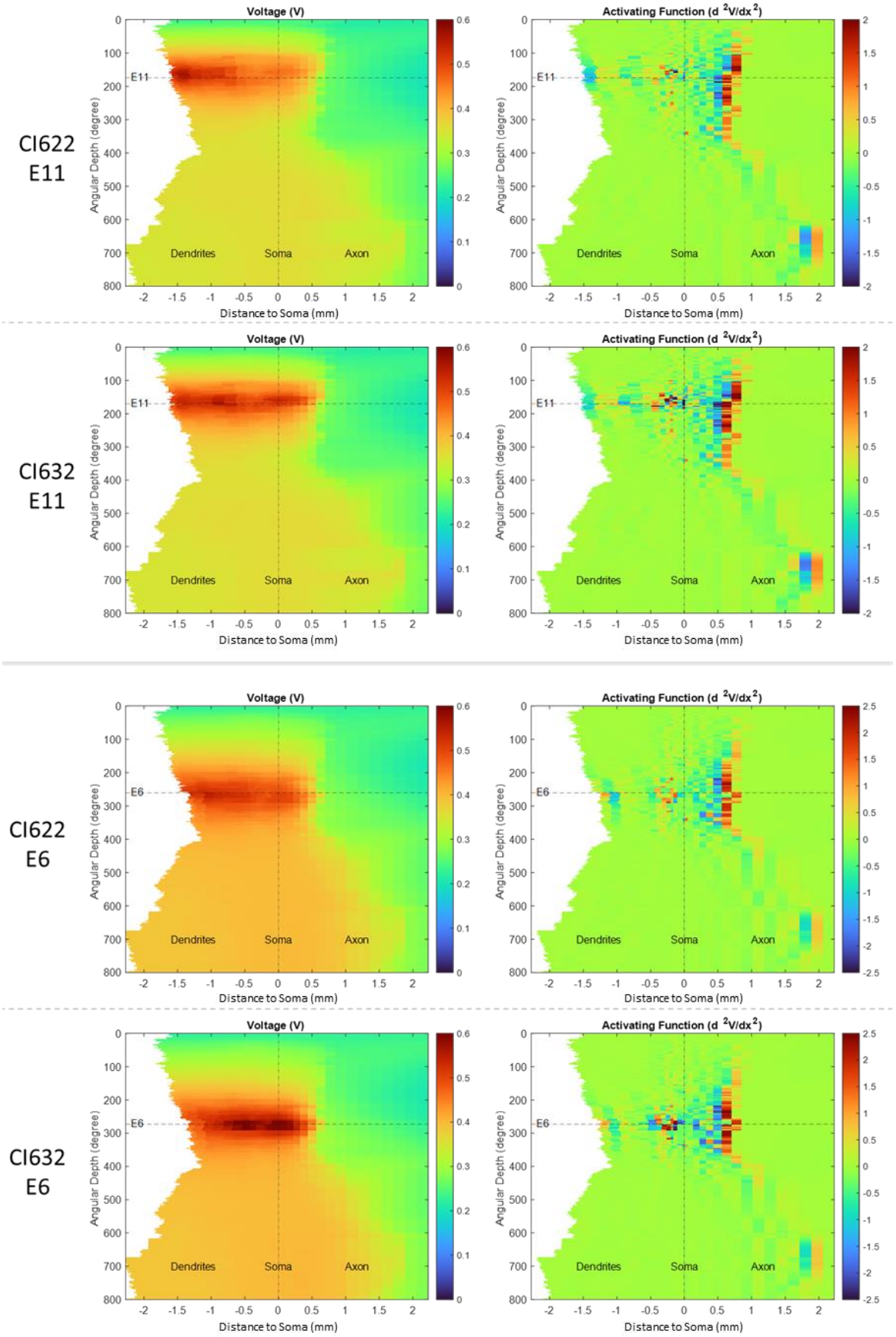

Figure 3.19 (Continued): Voltage and activating functions on trajectories by anodic CI stimulations. This page shows the results of E11 and E6 of both CI622 and CI632 for comparison. Note that the scales of activating function are different.

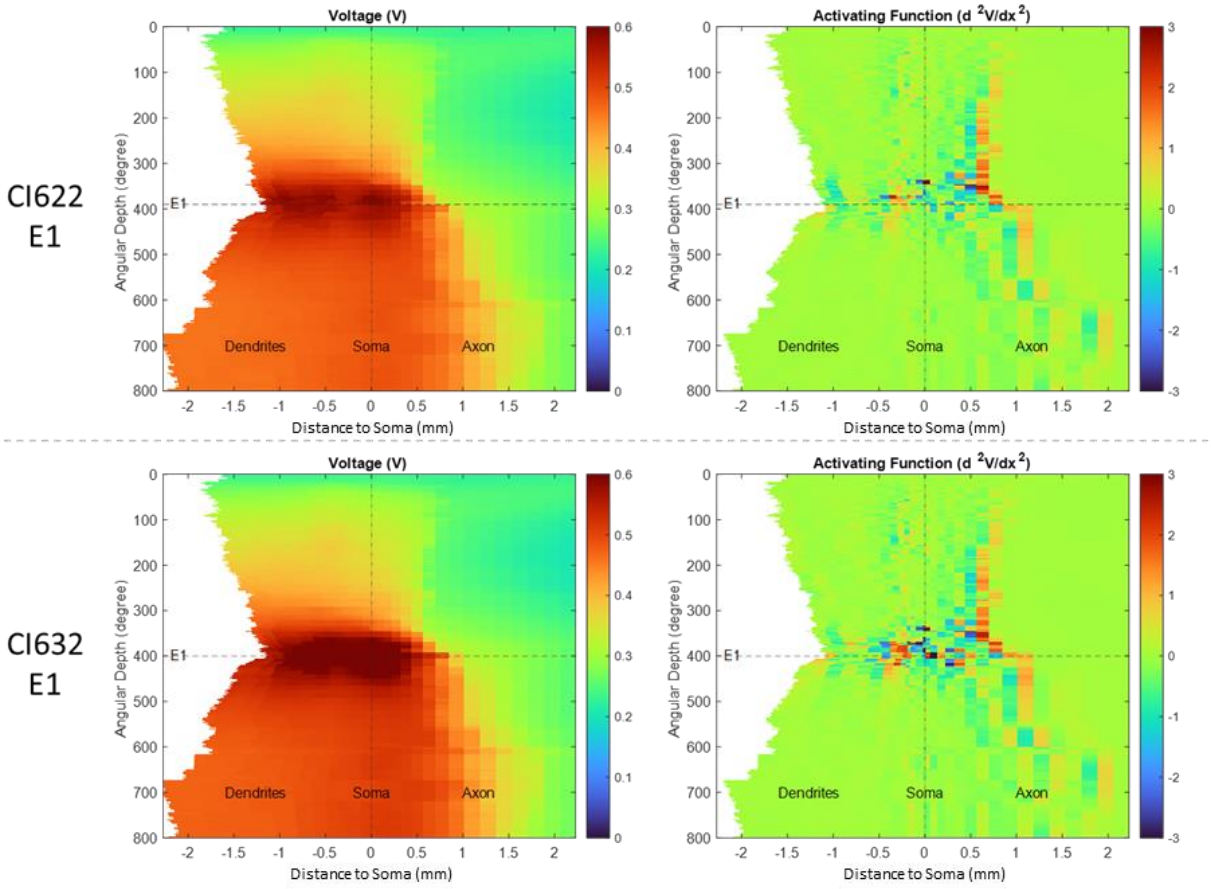

Figure 3.19 (Continued): Voltage and activating functions on trajectories by anodic CI stimulations. This page shows the results of E1 (most apical) of both CI622 and CI632 for comparison. Note that the scales of activating function are different.

The figures provide a wealth of information. Firstly, the voltage patterns of CI622 and CI632 differ significantly. CI632 causes a "deeper" and higher voltage spread toward the soma, aligning with expectations. Figure 3.20 shows the differences on voltage and activating functions between CI632 and CI622, taking E11 as an example. The amplitude and spread range of activating functions caused by CI632 are very similar to CI622 when examining the full scope of trajectories. The primary difference lies in the dendrite and soma regions, where CI632 induces activating functions, while CI622 does not. Additionally, for both CIs in Figure 3.19, the activating function in apical regions is notably higher than in basal regions, consistent with the fact that basal electrodes have a higher threshold of activation than apical ones[23,105].

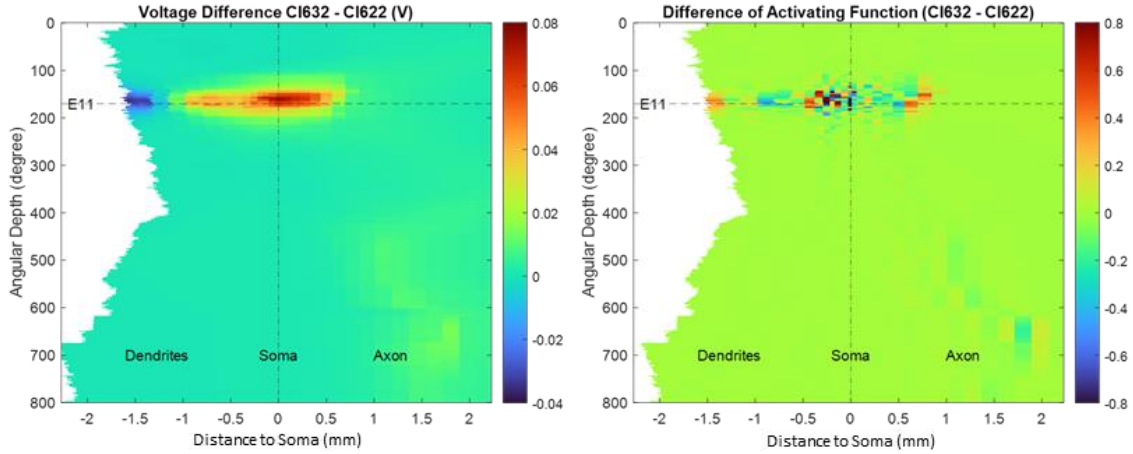

Figure 3.20: Voltage and activating function difference between CI632 and CI622 when E11 stimulates. The differences are mostly near soma and on dendrites, indicating that CI632 has better stimulation outcomes on soma and dendrites than CI622.

The most notable result is that the main activations occur at the axon across the entire array for anodic stimulation. This aligns with the assumption of the polarity effect, but the question remains—why does this polarity effect occur? To delve deeper into this, a typical voltage and activating function profile of a single curve is shown in Figure 3.21, taken from the trajectory at 140 degrees when E11 in a CI622 is stimulating.

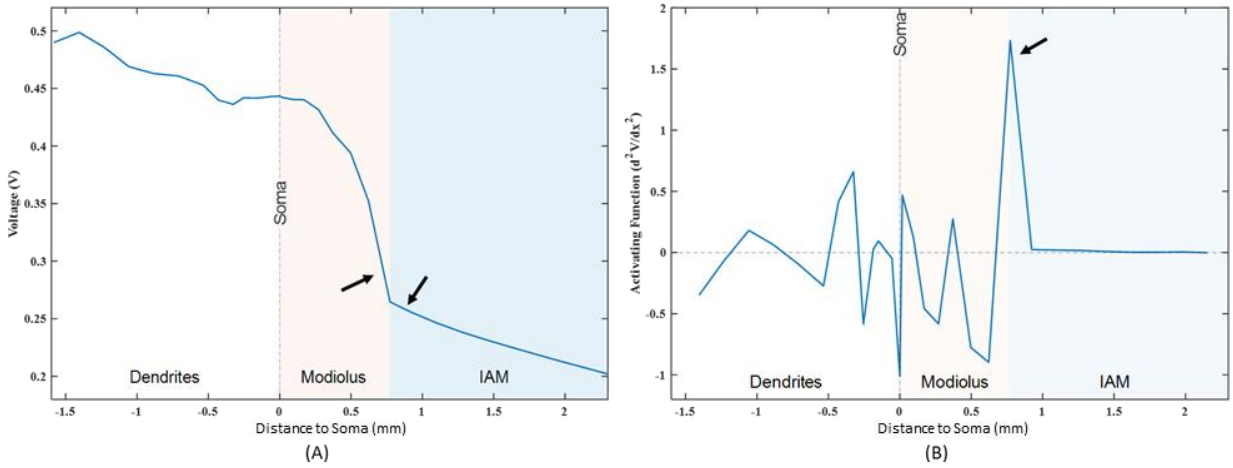

Figure 3.21: Voltage and activating function profile of a single trajectory under E11 anodic stimulation. (A) The voltage profile. Positions of soma, dendrite, and axon in modiolus and internal auditory meatus (IAM) are marked. The change in the voltage change rate is indicated by bold arrows. (B) The activating function calculated from figure A. The peak between IAM and modiolus is noted.

A rapid change in voltage dropping rate can be observed in Figure 3.21A, which is effectively the second derivative of voltage. This change is caused by the IAM. In the modiolus, the nerve is surrounded by bone (and some nerve tissue), which has much lower conductivity than cerebrospinal fluid and nerve tissue in IAM (the conductivities

are in Table 2.3, and the structures of IAM and modiolus could refer to Figure 3.2 and 3.8). Therefore, the voltage along the trajectory drops rapidly in the modiolus but the rate of drop becomes much slower in IAM. The resulting positive peak in the activating function is also marked in Figure 3.21B. Additionally, the voltage fluctuations in the dendrites are caused by the porous structure of the modiolus, as the conductivity changes between bone and nerve tissue (pores). This also causes some activating functions on dendrites; however, it is not as significant as the modiolus-IAM interface.

Notably, based on the activating function theory, a positive activating function will cause depolarization and therefore activation; a negative activating function will tend to cause hyperpolarization, which is related to inhibition[40,41]. In Figure 3.21B, the positive high peak at the axon indicates strong activation, while the mostly negative values at dendrites may not be able to cause activation.

In exploring the effects of cathodic stimulation, a diverse and intricate activation pattern emerges. Figure 3.22 provides a detailed depiction of voltage and activating function patterns for electrodes E22, E16, E11, E6, and E1. It is important to note that, in our resistive model, cathodic results mirror the opposite values observed in anodic stimulation shown in Figure 3.19.

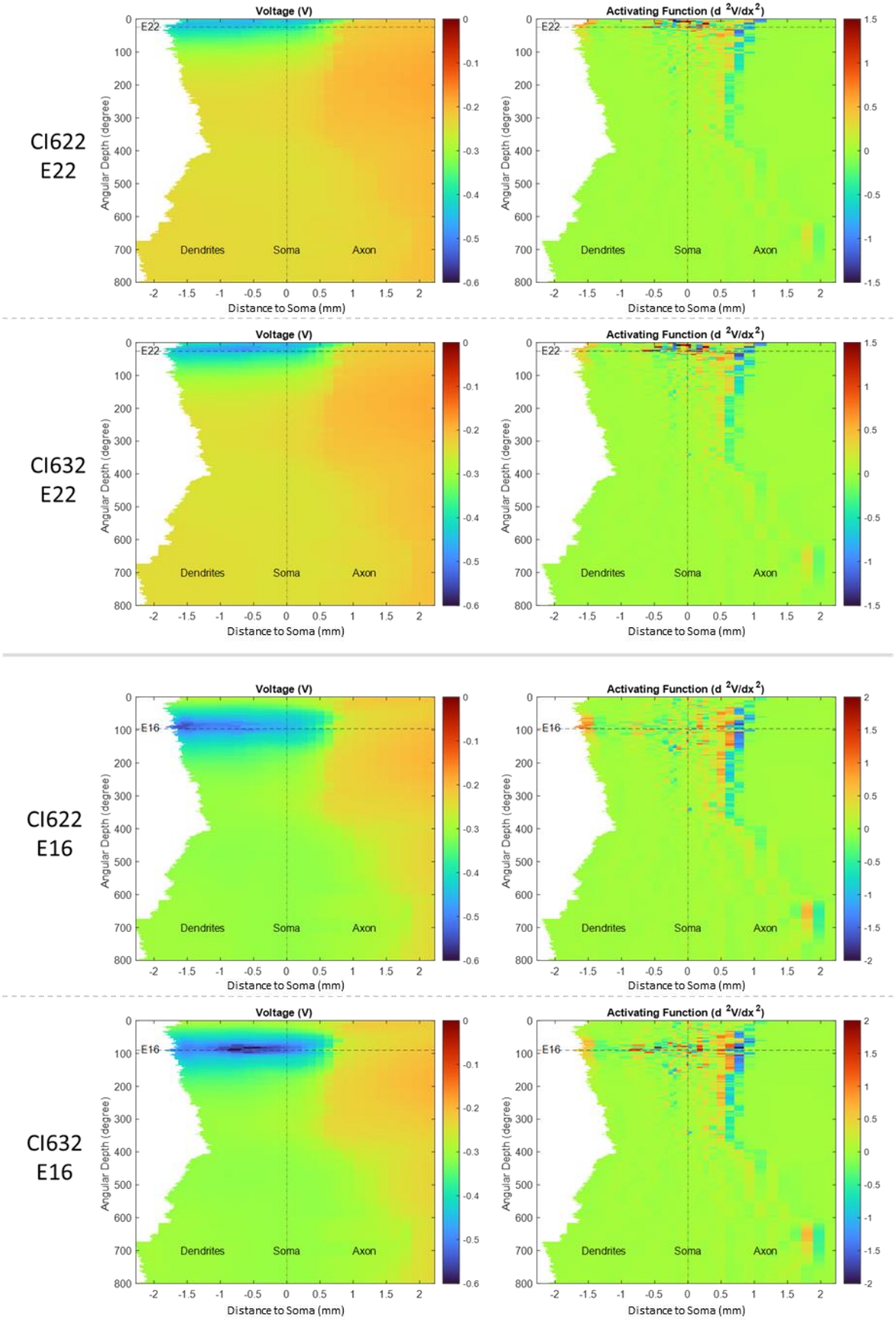

Figure 3.22: Voltage and activating functions on trajectories by cathodic CI stimulations. This page shows the results of E22 (most basal) and E16 of both CI622 and CI632 for comparison. Note that the scales of activating function are different.

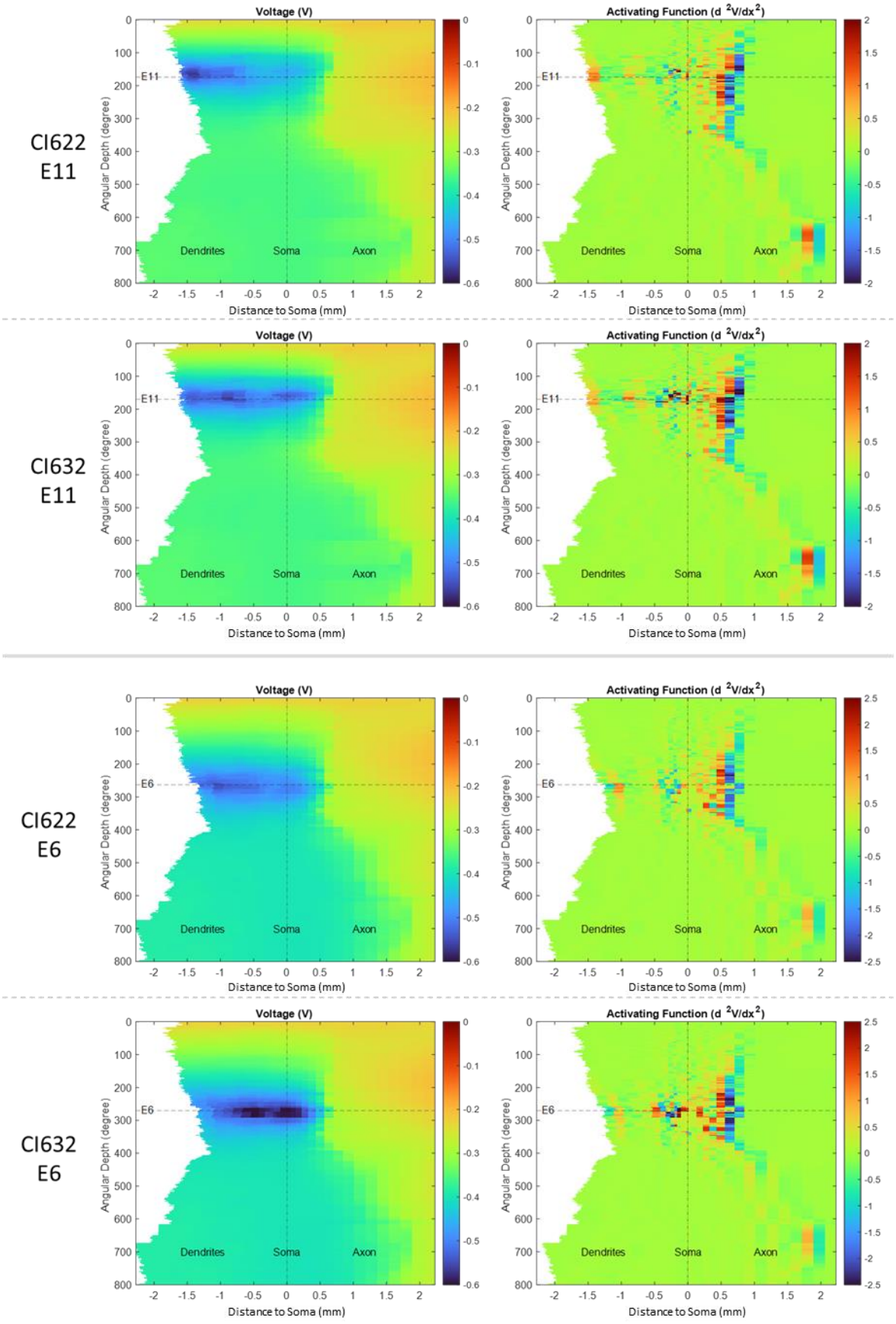

Figure 3.22 (Continued): Voltage and activating functions on trajectories by cathodic CI stimulations. This page shows the results of E11 and E6 of both CI622 and CI632 for comparison. Note that the scales of activating function are different.

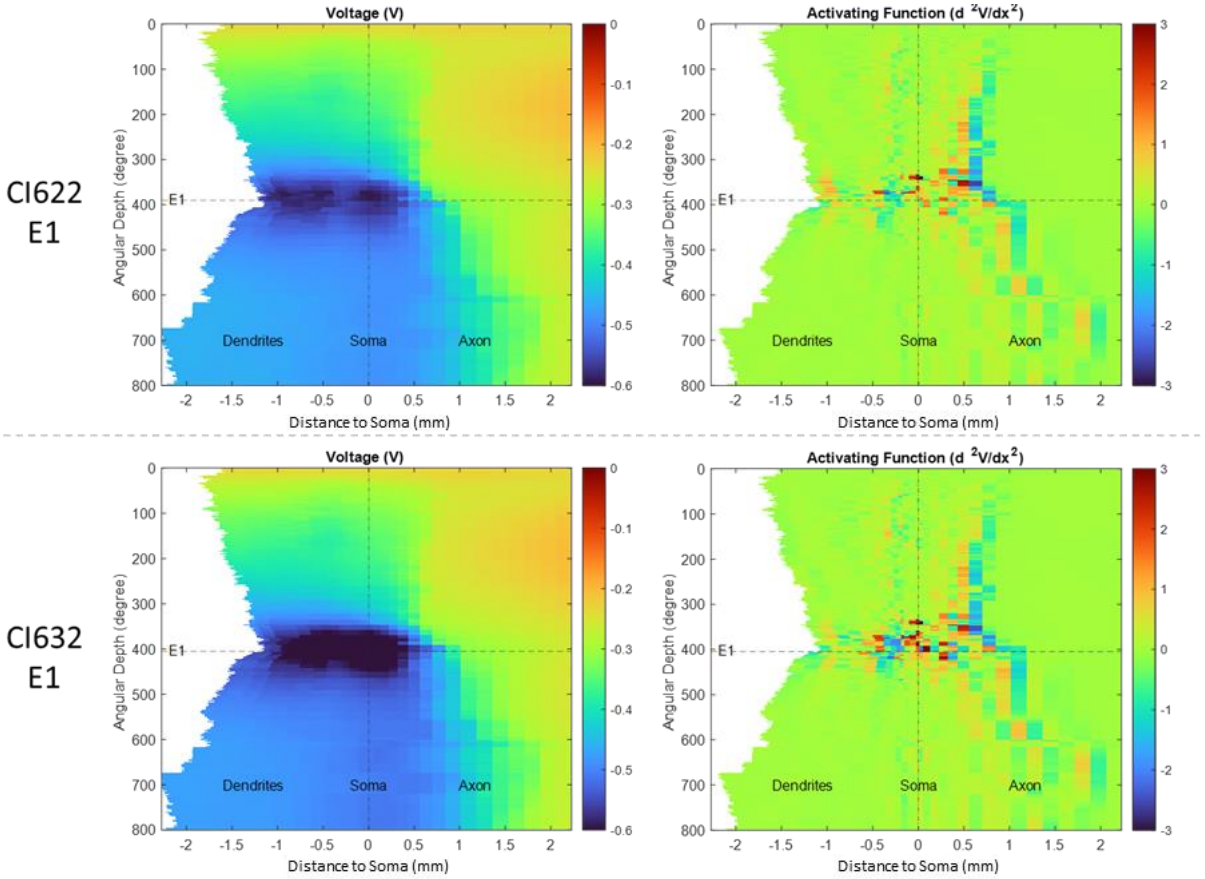

Figure 3.22 (Continued): Voltage and activating functions on trajectories by cathodic CI stimulations. This page shows the results of E1 (most apical) of both CI622 and CI632 for comparison. Note that the scales of activating function are different.

Figure 3.22 presents the effects of cathodic CI stimulations. The activating functions exhibit notable peaks at the tip of dendrites, near the soma, and at the axon immediately after the soma. To delve deeper, Figure 3.23 showcases a trajectory under cathodic stimulation, with values inverted from the anodic scenario presented in Figure 3.21. At dendrites and the soma, activating functions are predominantly positive. However, at the central axon near the modiolus-IAM interface, a sharp change of the increase rate of the voltage results in a large negative peak in the activating function. This suggests that cathodic stimulations could potentially inhibit neural activity at this location. Essentially, even though portions of the axon exhibit positive activating functions, the significant negative peak at the more central site could potentially prevent the axon from firing. Conversely, the activating functions at the dendrites and soma are mostly positive, suggesting a higher possibility of neural firing at these sites. It's also possible that soma positions may vary among neuron groups or clusters, with some soma strategically positioned closer to the modiolus-IAM interface, making them more susceptible to

stimulation. In either case, dendrites and soma consistently emerge as preferential sites for activations.

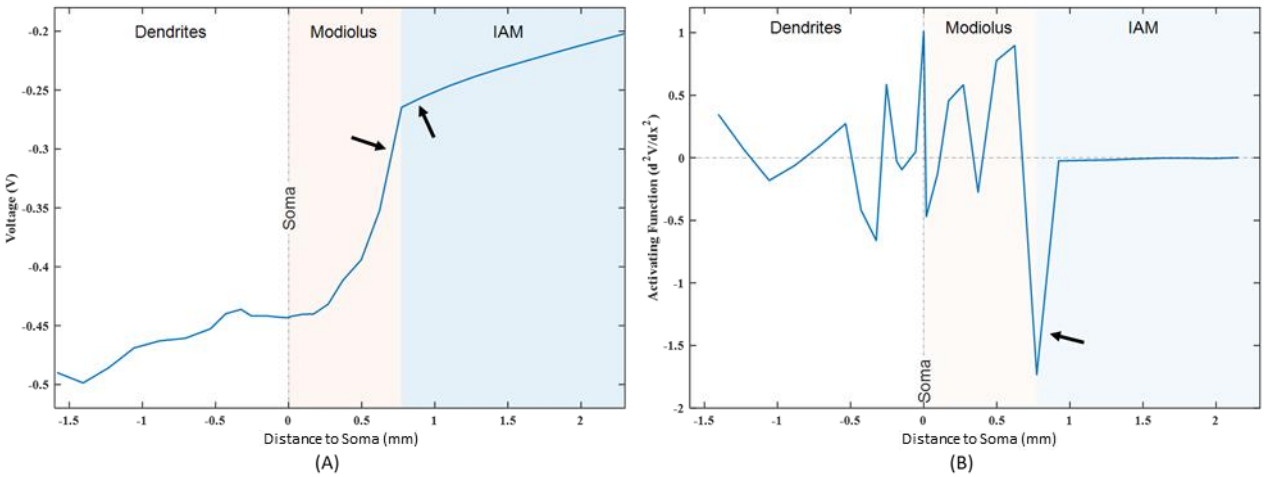

Figure 3.23: Voltage and activating function profile of a single trajectory under E11 cathodic stimulation. (A) The voltage profile. (B) The activating function calculated from figure A. The negative peak between IAM and modiolus is noted.

3.4 Discussion and hypothesis proposal

This study introduces a fresh perspective on neural activation principles in cochlear implants by underscoring the significance of the IAM. Unlike many computational studies that focus solely on the cochlea's spiral shape, our exploration sheds light on the overlooked role of the IAM. Additionally, we also examine the impact of the porous modiolus structure on dendrite activations. To encapsulate our findings, put forward a hypothesis to explain some longstanding observations, and acknowledge the study's limitations, I discuss the findings in the next section.

3.4.1 The hypothesis, polarity effects and CI positions

Current modelling studies underscore the role of the natural structure of the IAM in neural activations. As a spacious canal filled with cerebrospinal fluid, the IAM serves as a highly conductive pathway for CI stimulations, leading to a rapid change in voltage. This results in a positive or negative peak in the second derivative of voltage along the central axon.

The CI polarity effect, where anodic pulses tend to stimulate the axon while cathodic pulses tend to stimulate the dendrites and soma, can be explained by the presence of the

IAM. Anodic pulses generate a high activating function peak at the modiolus-IAM interface, suggesting this is the site of activations. On the other hand, cathodic pulses yield positive activating functions at dendrites and soma but encounter a large negative peak at the axon due to IAM. Thus, the IAM promotes axon activation in anodic cases but hinders it in cathodic cases. The possibility of neural axons to be stimulated at the IAM site was discussed, as some unexpected neural responses were observed in patients[106]. Regretfully, no further research on this topic has been reported.

Recent computational studies addressing the polarity effect have yet to reach a clear conclusion. It is suggested that our more precise and comprehensive model, incorporating all relevant natural structures, may offer a more straightforward explanation. The IAM and porous modiolus, often simplified or overlooked, could play important roles in CI activation of neural structures.

Regarding CI placements, such as peri-modiolar and lateral wall CIs, the theory discussed has important implications. In anodic scenarios, if activations occur predominantly at the IAM-modiolus interface, the precise proximity of the CI to the modiolus or Rosenthal's canal becomes of not great importance. In contrast, cathodic stimulations highlight the potential superiority of peri-modiolar CIs due to their enhanced activating functions on dendrites and soma. Nevertheless, their efficacy might be reduced in instances of significant dendritic degeneration in patients, which might account for the discordant results reported in studies.

Additionally, variations in the positions of "nodes" in different nerve models may introduce some uncertainty in the calculated activating function values. However, the key point is that as long as a rapid voltage change occurs at the modiolus-IAM interface, there will always be a node located closest to that interface, resulting in a substantial peak in the activating function. This phenomenon stems directly from the anatomy of the IAM and cochlea.

After proposing the core hypothesis about site of activation, I would like to briefly address two additional intriguing questions that have been raised. First, despite my hypothesis that lateral wall and peri-modiolar cochlear implants activate the auditory nerve similarly, ECAP recordings show that peri-modiolar implants can yield a clearer neuronal response

pattern given identical stimulation parameters[56]. To explore this, I created a rough simulation of ECAP recording with two somas (20 μm diameter spheres in Rosenthal's canal) emitting 100 nA each to mimic action potentials from soma as an example. Using this model, peri-modiolar implants recorded higher amplitude ECAP peaks compared to lateral wall implants. Therefore, while both implant types may activate the auditory nerve equivalently, peri-modiolar CIs could yield a clearer ECAP pattern due to their better recording capability.

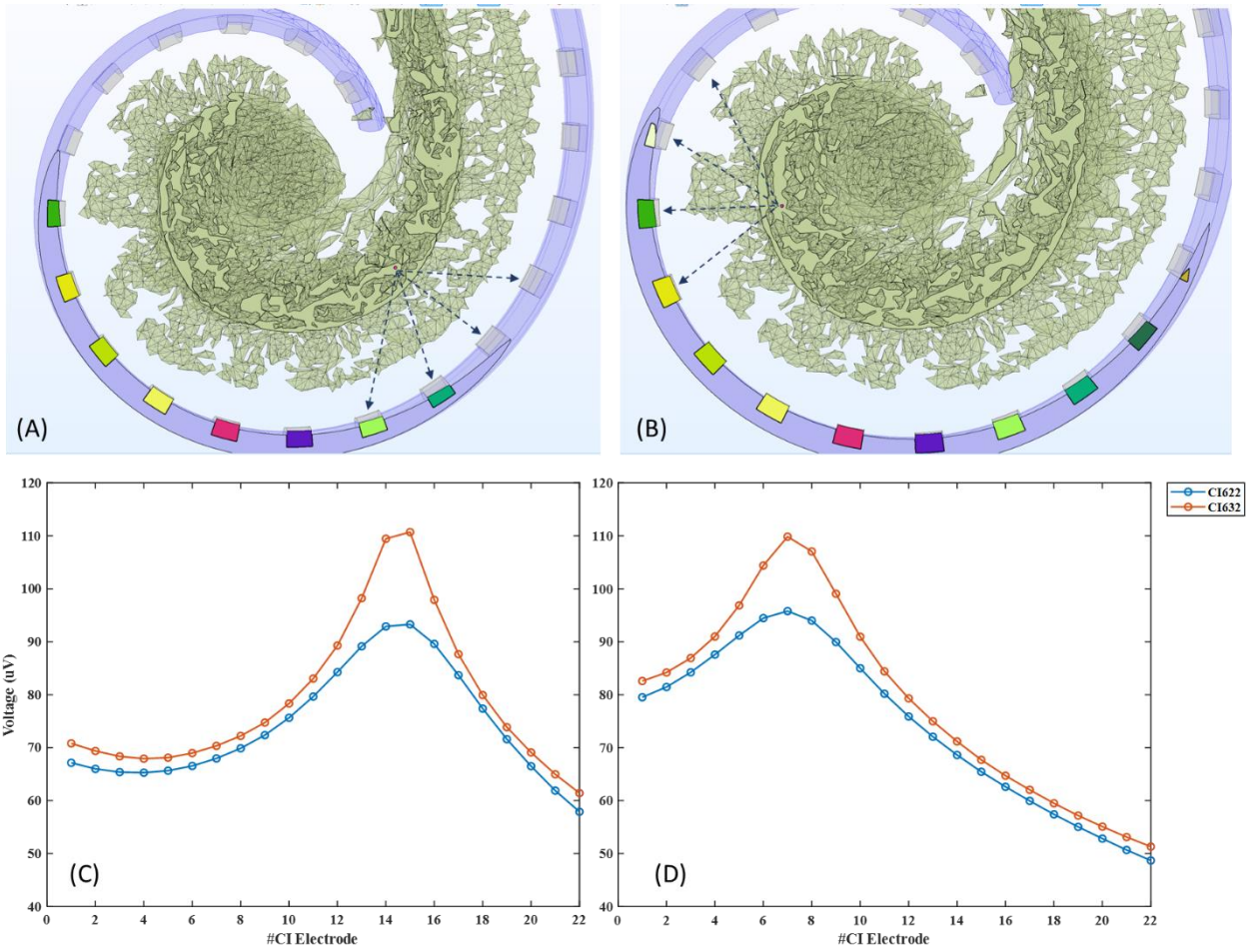

Figure 3.24: ECAP recording simulation of two CI types. (A) and (B) depict the positions of two somas emitting current to mimic action potentials. (C) and (D) represent the recorded voltage from CI electrodes corresponding to the two somas, respectively.

The second question relates to the spread of excitation. In my results in Figures 3.19 and 3.22, the spread of excitation can reach 100 degrees or more for each electrode. This seems to be quite high, but when checking the spread of excitation measured with ECAP results[11,107], the spread can vary significantly between patients. Some excitations could usig this method seem to spread across nearly the whole array, while others are confined

to just a few adjacent electrodes. This variability might be related to the specific cochlear structure of each patient, and to the population variations in residual spiral ganglion cells.

3.4.2 Limitations of this study

This work proposes a new hypothesis about site of activation of neural tissue, based on computational methods with more precise models and anatomical structures that are normally not included in models. However, there are a few limitations that need to be acknowledged and are summarized in this section.

The first limitation concerns the prediction of site activation. This work used the activating function as the indicator. In further work, not performed here, voltages or activating functions could be imported into a separate nerve model to better simulate neural activation predictions. However, current auditory nerve models may also not accurately represent reality, and are themselves based on many assumptions. Different models tend to use different parameters, leading to a variety of results. This is the problem I wanted to avoid by using calculated only the activating functions, as it would be more consistent across all nerve models. Different axon or dendrite diameters, neuron positions, etc., will also affect the resulting activation, but these are too complex to consider exhaustively in this thesis.

The second limitation is that only one cochlea model is used. In theory, different cochleae could be placed in the head model for comparison studies. However, porous modiolus segmentations require high-resolution scans such as the synchrotron imaging, of which we only had access to one raw data file, and segmentation of the pores etc is a very time consuming and laborious. The effect of the IAM is quite large, however, and I would expect the generalizability of these results to persist across cochleae. In addition, here different parts of the model also come from different scans and are placed in the correct position based on reconstructing normal anatomy. There could still be some small deviations in positions and size mismatch, but these are considered to be minor.

Other limitations also exist. The model is purely resistive due to the significantly increased complexity when considering temporal effects. However, the results of this model could be considered as a simulation of steady-state results when applying

stimulation pulses. Additionally, the conductivity of each component comes from the most commonly used values, but it may deviate and differ between patients.

3.5 Tripolar and Bipolar Stimulations

In the pursuit of enhancing Cochlear Implant (CI) performance, various strategies have been developed to mitigate voltage spread. One such is tripolar stimulation, a relatively mature technique, which has demonstrated efficacy in some studies for low-intensity sounds[108]. Studies have underscored the influence of CI positioning on hearing outcomes, with tripolar stimulation, which is a departure from the dynamics observed in monopolar stimulations[109,110]. However, the widespread adoption of tripolar stimulation has been hindered by its large power consumption. Similarly, bipolar stimulation has been explored, yet it remains less favoured due to its power consumption and lack of proven ability to limit electrical spread.

Within this section, we delve into the neural activation outcomes of both tripolar and bipolar stimulations using a head model. The results aim to explain how the positioning of CIs influences the spread of excitations, and we also examine the effectiveness of polarities.

3.5.1 Results on tripolar and bipolar simulations

In the anodic case of tripolar stimulation, the Nth electrode's stimulation current is set at 500 µA (N ranging from 2 to 21), while electrodes N-1 and N+1 are set at -250 µA. The cathodic case mirrors this setup in reverse. Due to space constraints, the results for electrode 11 (stimulating at 500 µA) are depicted in Figure 3.25, with additional data for electrodes 6 and 16 found in Figure A.3 in Appendix 2.

The tripolar results diverge significantly from monopolar outcomes. The overall spread of excitations is notably reduced (typically around 30 degrees compared to 100 degrees in monopolar). The mechanisms of stimulation also differ, with tripolar primarily targeting dendrites and soma, unrelated to the IAM. Electrode positions further increase these differences, with peri-modiolar CI (CI632) causing approximately 50% higher

voltage amplitude than lateral wall CI (CI622), resulting in activating functions around 100% higher. The figure scales illustrate these distinctions.

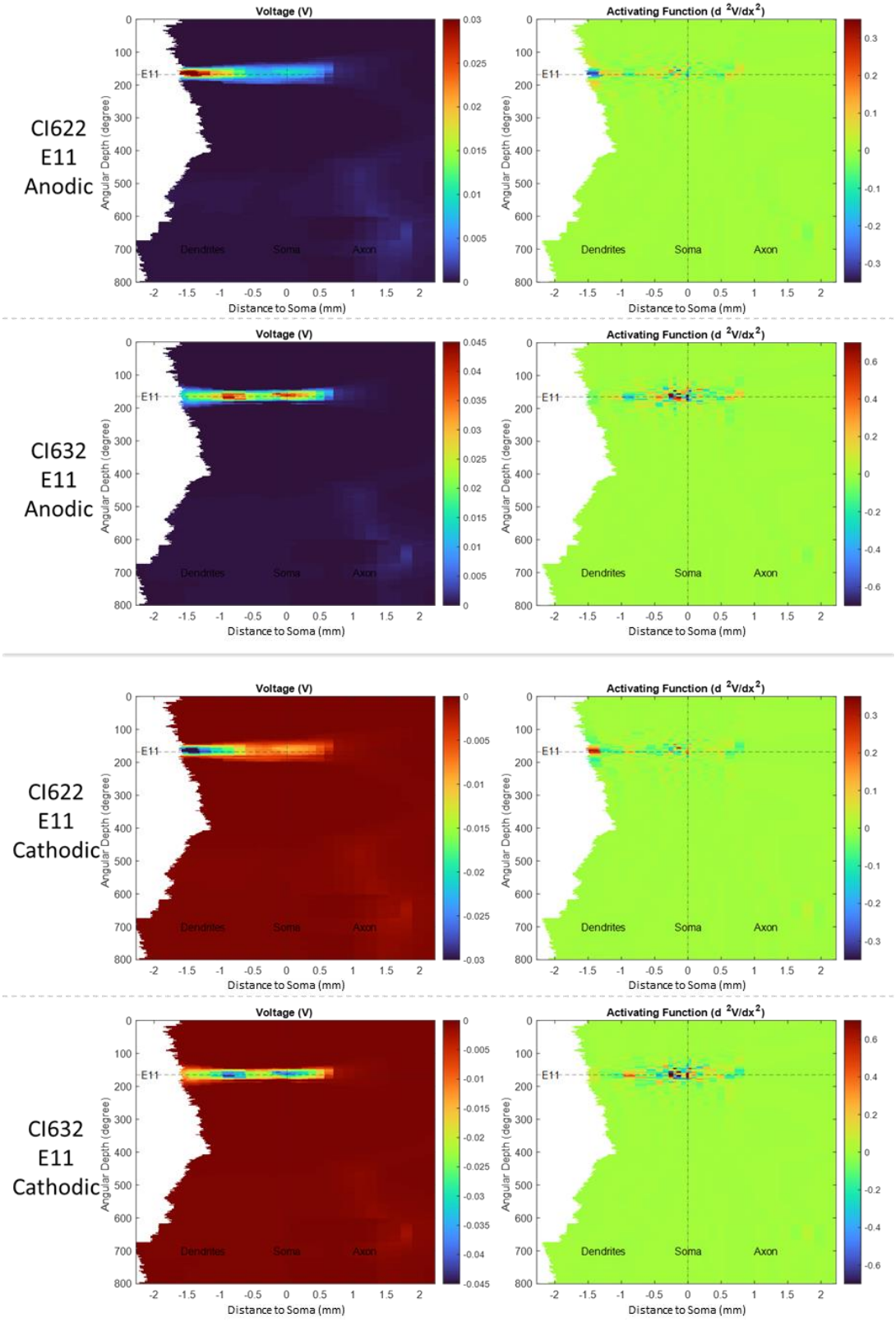

Figure 3.25: Voltage and activating functions on trajectories by tripolar stimulations. Figures show both anodic and cathodic stimulations of electrode 11. Please note that the scales are different in CI622 and CI632. Results for more electrodes are in appendix 2.

It's noteworthy that, compared to monopolar stimulation, tripolar activating functions exhibit a markedly lower amplitude (approximately 5 to 10 times). This aligns with the fact that tripolar stimulations demand significantly larger current stimuli and, consequently, higher power consumption, reflecting the trade-off of achieving highly focused stimulation. The overall amplitude of the activating functions for CI632 is notably higher than that of CI622, particularly concentrated near the soma region. In contrast, CI622 tends to stimulate the tips of the dendrites, as evidenced by its activating functions. Figure 3.26 illustrates the differences in voltage and activating functions when electrode E11 stimulates anodic pulses. It shows that CI632 results in a narrower voltage spread, as indicated by the angular width and amplitude of the voltage differences, and primarily targets the soma region.

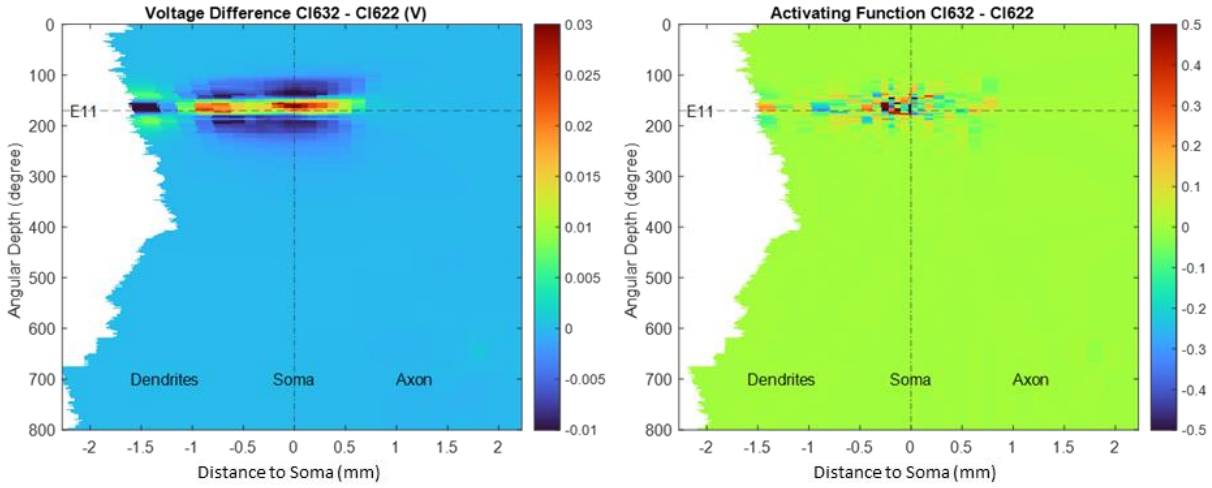

Figure 3.26: Differences of voltage and activating functions on of tripolar stimulations when E11 stimulates anodic pulses. The differences are mostly at soma and dendrites. The CI632 are shown to have less voltage spread and much higher activating functions.

For bipolar stimulation, in the anodic case, the Nth electrode's stimulation current is set at 500 µA (N from 1 to 21), and electrode N+1 is set at -500 µA. The cathodic case mirrors this configuration. Due to space constraints, results for electrode 11 (stimulating at +500 µA) are presented in Figure 3.27, with additional data for electrodes 6 and 16 in Figure A.4 in Appendix 2.

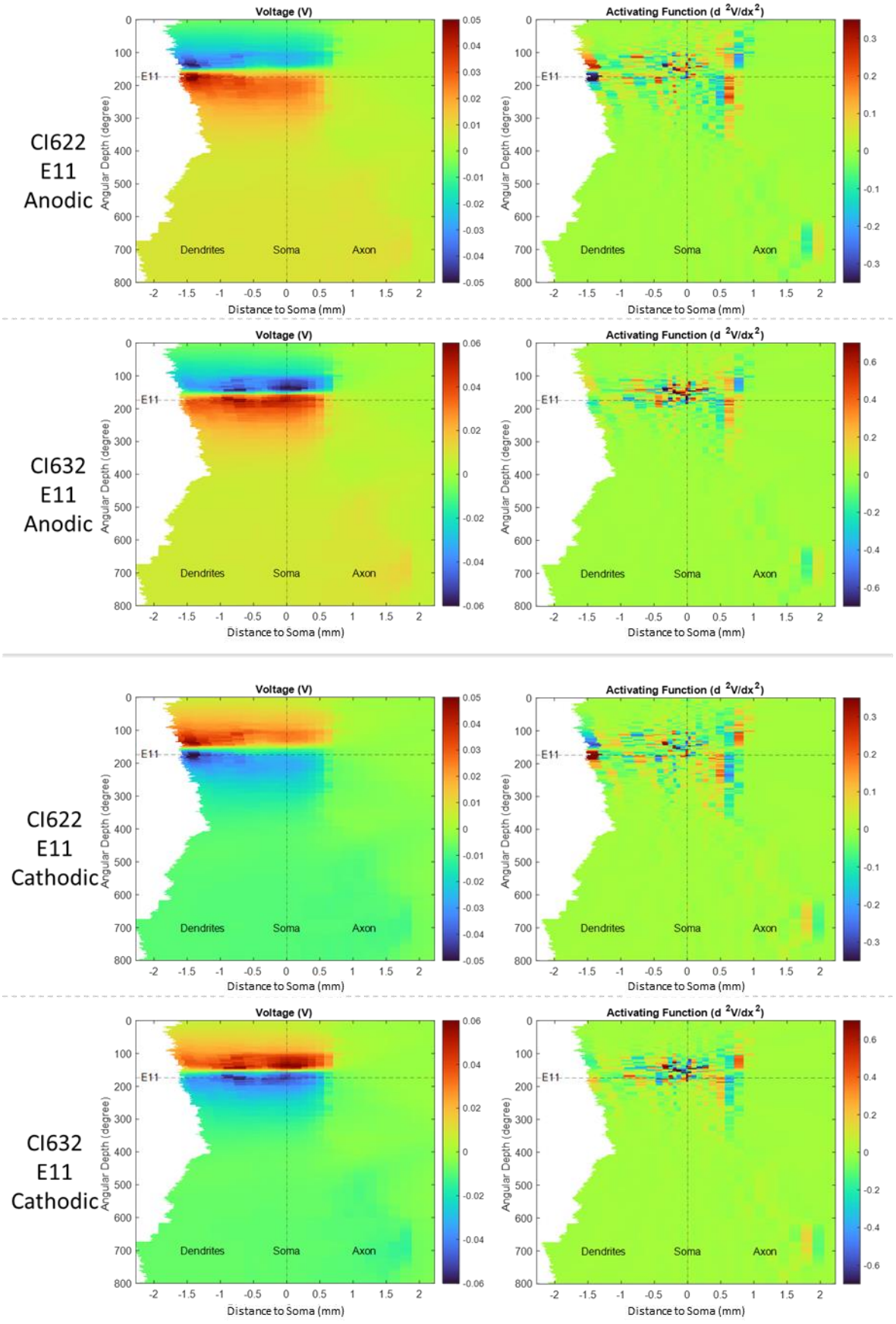

Figure 3.27: Voltage and activating functions on trajectories by bipolar stimulations. Figures show both anodic and cathodic stimulations of electrode 11. Please note that the scales are different in CI622 and CI632. Results of more electrodes are in appendix 2.

Unfortunately, bipolar results combine the drawbacks of both monopolar and tripolar approaches—large activation spreads with small activating function amplitudes. Symmetric voltage patterns and significant CI position influence characterize these outcomes, where activations occur in both axons and dendrites, presenting a hybrid of monopolar and tripolar characteristics.

3.5.2 Discussion

The tripolar stimulation method reveals a distinct mechanism compared to monopolar stimulation, operating independently of the IAM due to highly localized voltage generation near electrodes. The study suggests that the lateral wall CI tends to stimulate axon tips, with outcomes influenced by polarity. In contrast, peri-modiolar CI exhibits superior performance, generating higher activating functions without evident polarity effects. However, it is essential to note that these predictions have not been empirically studied in patients, and remain speculative. Additionally, the reported "sidelobe" effect[108], caused by opposing stimuli from adjacent electrodes, is not observed in the results presented.

Tripolar stimulation has several theoretical benefits, though high power consumption remains an issue. However, in practice, tripolar does not consistently improve outcomes compared to monopolar[28]. This may stem from relying on local dendrites near the electrodes, which are often degraded in patients. Also, practically, tripolar stimulation leads to much weaker stimulation of neurons, necessitating a significant increase in current amplitude. However, this increased current will, in turn, result in a larger spread of stimulation.

Bipolar stimulation seems to blend the mechanisms and drawbacks of both monopolar and tripolar modes. The results help illustrate why bipolar has been gradually abandoned to garner significant interest.

3.6 Conclusions and Future Work

This section proposes a novel hypothesis for site of activation and the polarity effect based on computational modelling studies. Precise cochlear models were constructed, incorporating a porous modiolus. Inclusion of additional cochlea-related components, such as the internal auditory meatus (IAM), yielded new insights. The IAM, as a major electrically conductive pathway beneath the modiolus, causes rapid voltage gradient changes along the neural axis. Consequently, anodic stimulation preferentially activates axons near the IAM-modiolus interface, while cathodic stimulation biases towards dendrites and somas. To my knowledge, this conclusion has not been reported in other CI research.

CI performance has plateaued over the past 20-30 years, implying overlooked theories and unexplained observations exist. Some attribute this to electrode-neuron mismatch[2], but effective CI information channels are usually thought to be around 8 in speech in quiet[111]. Adding electrodes or shifting positions may provide minimal benefits. Others cite incomplete brain models[112], but the huge variability between patients, from immediate success to years of struggle, implies differences in brain function alone cannot account for this.

Validating the hypotheses in this chapter in vivo or in vitro remains challenging without altering cochlear structures. Direct physical measurement of the encased auditory nerve is difficult. Even accessing the cochlea/IAM in cadavers would permanently change anatomy and voltage distribution. However, physical confirmation is essential to substantiate the computational findings. If validated, this hypothesis could transform cochlear implant design. Rather than a curved electrode in the scala tympani, new designs could be inspired to interface with the cochlea in novel ways that utilize the IAM effects on voltage gradients and neural activation.

4 APPLICATIONS OF HEAD MODEL TO PREDICT AND UNDERSTAND CLINICAL MEASUREMENTS

This section presents some applications of the head model as an extension of the previous chapter. This chapter presents work on simulating detection of extra-cochlear electrodes, detecting CI partial shorts, and the scalp voltages expected from CI stimulations, which could be used diagnostically and clinically. Clinical data are included as validation of the results and also as a method to validate the head model. Specifically, the detection of one extra-cochlear electrode was studied, and cadaveric experiments we have performed in the lab were compared to simulations.

To compare with simulation data, the clinically measured living human data of scalp voltage and extra-cochlear EFIs for validations were de-identified data from the clinical cochlear implant centre as part of an ethics approved human research study, and the cadaveric extra-cochlear EFIs are from Dr. Simone de Rijk.

4.1 Introduction

To enhance the validation of our computational head model and gain deeper insights into important clinical issues, this chapter simulates of extra-cochlear electrodes, scalp voltage, and partial shorts of Cochlear Implants (CIs).

Extra-cochlear electrodes (EEs) are estimated to occur in over 10% of patients[113], stemming from factors such as incomplete insertion during surgery or CI migrations after insertion[114]. This reduction in effective number of CI channels and lack of apical stimulation may lead to re-implantation surgery[115]. Others in the SENSElab have shown previously that EFI measurements are very effective in detecting 3 or more extra-cochlear electrodes[47,116], However, detecting only 1 extra-cochlear electrode has been challenging. Notably, the most basal electrode near the round window, even when extracochlear, exhibits EFI data closely resembling that of intra-cochlear electrodes.

Another CI failure mode is that of partial short-circuits, referring to electrodes being shorted to ground or shorted to each other[117]. Although clinically detectable through EFI, this study simulates this phenomenon to validate the computational model. Furthermore, we explore the simulation of scalp voltage induced by cochlear implant stimulations, a diagnostically easily measured parameter that holds potential clinical applications[118-120]. Recent research has demonstrated the feasibility of leveraging scalp voltage to identify issues such as extra-cochlear electrodes or partial shorts[121]. In line with this, our work also includes simulations of scalp voltage under various conditions within the head model.

4.2 Effects on Extra-cochlear Electrodes (EEs)

4.2.1 EE Simulations and clinical results validations

To further understand the intricacies of a scenario where an electrode has "slipped out" of the cochlea, the head model was adjusted to represent this situation. Figure 4.1 visually captures a model encompassing four extra-cochlear electrodes (4EE). For this chapter, the lateral wall CI type has been utilized, given its prevalent use and because we have more clinical data for this type.

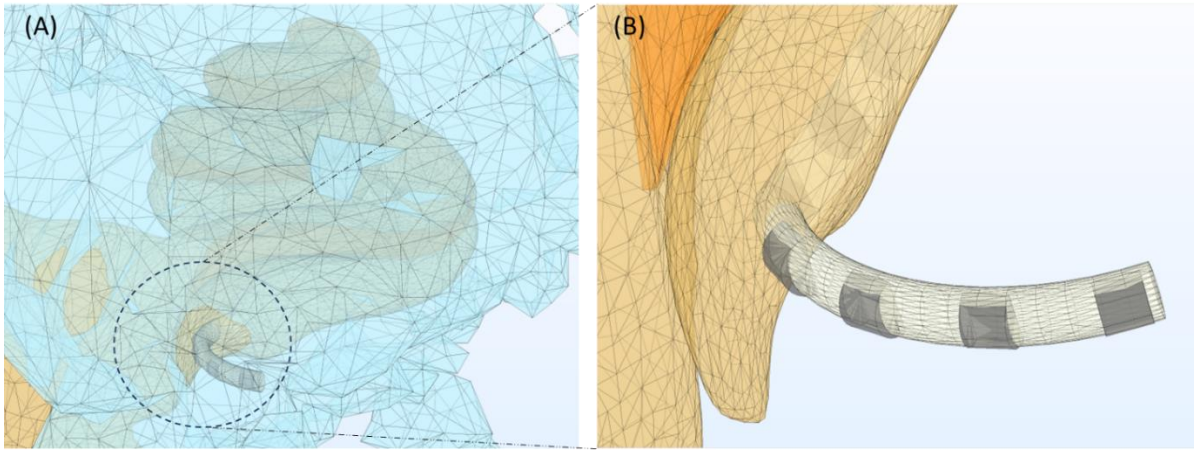

Figure 4.1: Model of 4 extra-cochlear electrodes. (A) Four electrodes are positioned outside the round window inside the middle ear. The round window area is visible in the figure. (B) A detailed view of the CI model with other components of the head model hidden.

From a clinical standpoint, the external portion of the CI is often encased in soft tissue, such as the temporal muscle or blood[47], certainly during surgery and afterwards as well if there is fibrosis. Given that the middle ear is predominantly air-filled, external electrodes in air are easy to detect because of the high impedance. However, those that are surrounded by saline, blood or soft-tissue at the end of surgery, or soft-tissue later post-operatively are much harder to detect using impedances, as they will often show normal impedances as the tissue or fluid surrounding them also conducts electricity well.

Our group's prior cadaveric research[47] recorded EFIs and electrode impedances under varied extra-cochlear electrode scenarios using human cadaveric heads. During these tests, a substantial amount of saline was introduced into the middle ear to saturate the middle ear. This can be the case at the end of surgery too, where saline or blood fills the area of the middle ear surrounding the electrodes. Reflecting this procedure, a saline filled middle ear model was developed. Figure 4.2A shows this saline model, coloured in red, with an electrical conductivity set at 1.8 S/m (parallel to cerebrospinal fluids). The saline volume set in this figure aims to replicate the conditions during the actual physical measurements. Notably, simulations indicate that the quantity of saline or soft tissue in the middle ear surrounding the EE portion of the CI will significantly influence the EFIs. Additional cases demonstrating this effect will be presented in subsequent parts of this section. Based on this configuration, the subsequent EFI and electrode impedances were simulated.

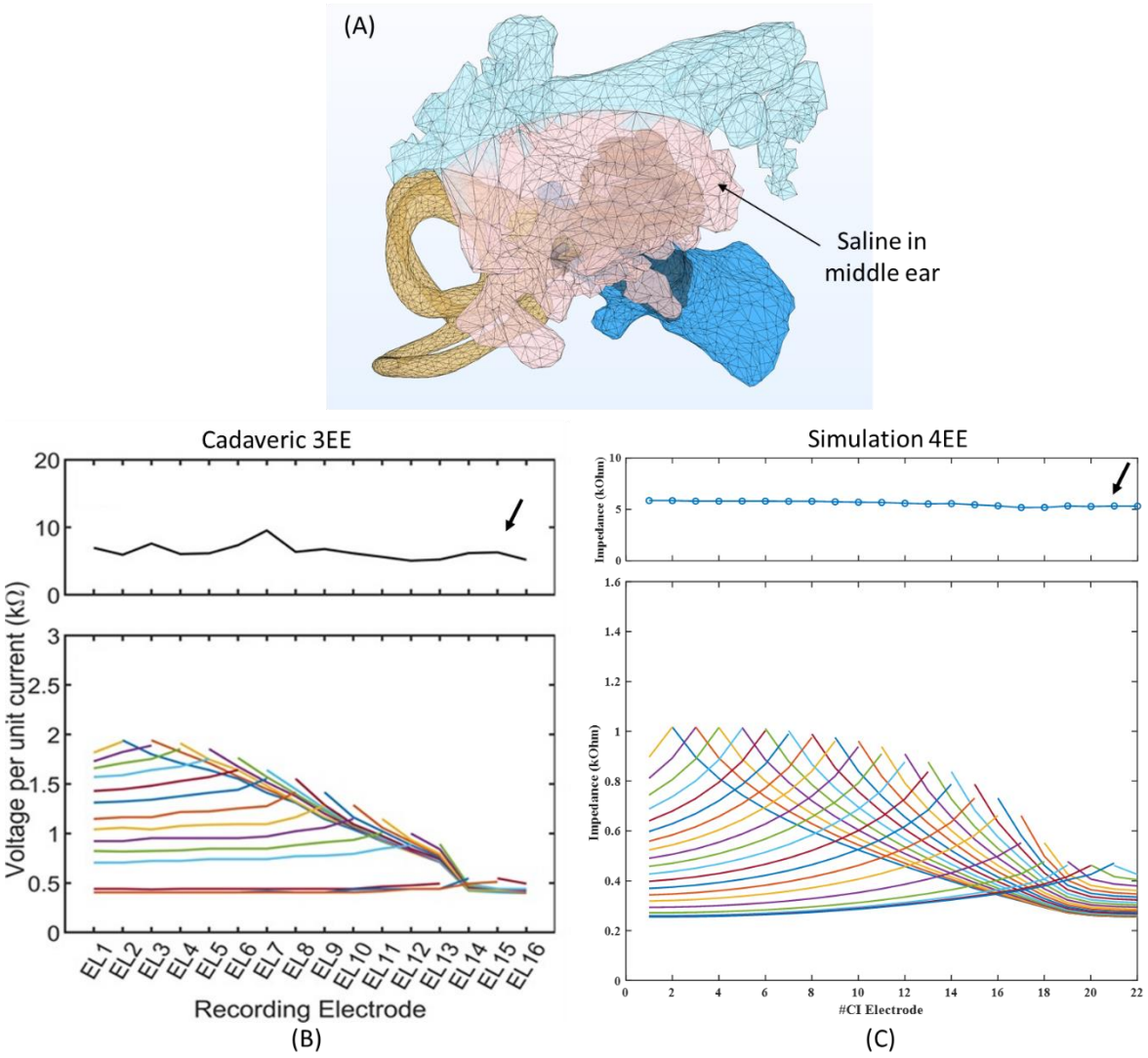

Figure 4.2: Modelling the extra-cochlear electrodes (EEs) cadaveric measurements with saline in middle ear. (A) The model with a relatively large amount of saline filled in the middle ear. (B) The EFI and impedance measurement in the cadaveric study[47]. Figure adapted under CC BY 4.0. (C) The simulated results mimicking the cadaveric conditions. 3EE means 3 extracochlear electrodes, 4EE means 4 extra-cochlear electrodes etc. The bold arrows indicate the impedance having no obvious change in the EE part, and the simulation exhibits the same phenomenon.

Figure 4.2B and C show cadaveric data[47] and my simulation results, respectively. The cadaveric data used a 16-electrode CI with 3 EEs, while the simulation employed a 22-electrode CI with 4 EEs. Despite differing absolute values (attributed to live patients in my simulation versus cadavers in the experiments), both exhibit similar trends. Notably, cadaveric total impedances for extra-cochlear electrodes show negligible change despite collapsing EFIs (bold arrow). My simulations confirm this phenomenon, indicating electrode impedance depends more on the biological pathway through bone to the ground electrode and electrode contact impedance, rather than cochlear electrode position.

In addition to our cadaveric data, de-identified clinical data for EE as part of an ethics approved intraoperative research study in our centre was used for simulation. These clinically acquired EFI readings were performed intraoperatively, with specific numbers of EE left out during the implantation process (all were fully implanted at end of surgery, but in stages), and covered with blood or soft tissue with EFI measurements performed simultaneously. I simulated this with blood or soft tissue covering the EE, similar to the live condition. To be simple, blood is represented by saline in simulations, and will be referred to as saline in the following parts of this section.

To simulate clinical measurements, Figure 4.3 displays models with two different soft tissue or saline sizes. In the simulations, the same models are utilized for both soft tissue and saline, but they are assigned different conductivities, set at 0.46 S/m for soft tissue and 1.8 S/m for saline, respectively[102]. The size of the soft tissue models was estimated by talking to the surgeons involved, as no photos were available from the clinical experiments.

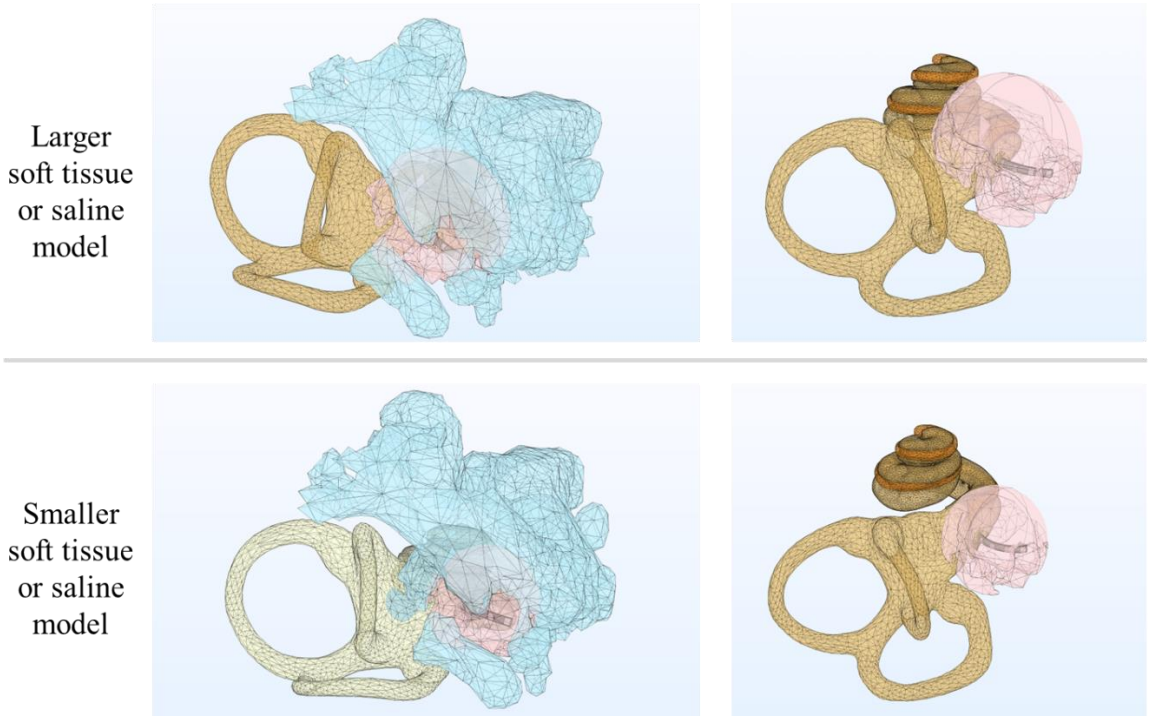

Figure 4.3: Modelling the soft tissue or saline in middle ear during the clinical experiments. Two different sizes are created for EFI simulations. The blue model is the middle ear, while the red model is the blood or soft tissue outside the round window.

Figure 4.4 shows the simulated EFIs compared to clinical measurements from four patients under varying conditions. Unfortunately, no record exists of the blood/muscle

amounts used clinically, only that they completely covered the EE electrodes. However, simulations indicate EFIs correlate with soft tissue size. Conductivity differences between muscle and blood also greatly impact EFIs. By modulating soft tissue size and conductivity, simulations approximate clinical cases. Figure 4.4 displays four such cases. Clinical data reports that the hearing outcome of CI patients will be largely degraded when 4 electrodes are out of cochlea[122]. As a result, simulations in this section used 4EE configurations, while clinical data ranged from 2EE to 4EE. Though the simulation and clinical data used different CI types and were different in EE numbers, the trends of EFI patterns and changes could be studied and are shown to be similar. It should be noted that these implants were done as re-implants, reimplanting normally functioning implants in patients who had had failure of their implant, the recordings are from the normally functioning implants. This was because recordings were performed during the COVID lockdown, when only semi-urgent surgery was permitted.

A clear pattern emerges, in that a reduced soft tissue volume can lead to an obvious shift in the basal EFIs. Intuitively, a smaller soft tissue volume, being a suboptimal conductor, results in increased voltages in those electrodes in the EE part during stimulation, especially when compared with larger soft tissue. In alignment with this, blood, being more conductive, typically leads to lower and flatter basal EFIs compared to the temporal muscle.

The results demonstrate that extra-cochlear electrode (EE) impedance is heavily influenced by soft tissue size and type. Clinically, detection methods cannot readily ascertain the soft tissue conditions around the EEs (except during surgery). The simulations revealed correlations between soft tissue factors and EFIs, providing insights into how to interpret EFIs obtained clinically, despite limitations in clinical knowledge of the EE environment.

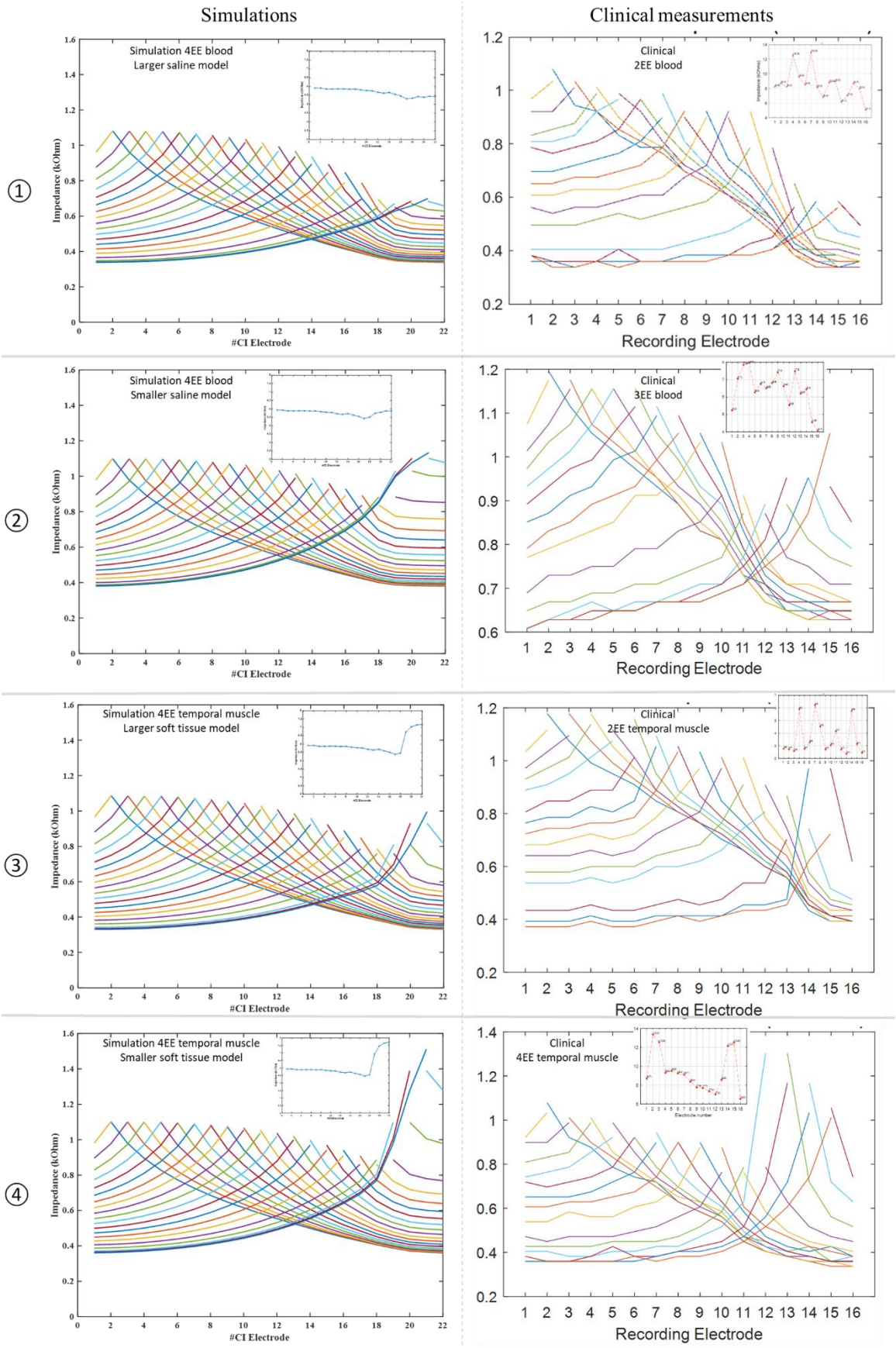

Figure 4.4: Four simulation cases mimicking four clinical measurements. By modulating the soft tissue size and type (blood or temporal muscle), the simulated EFIs can replicate clinical measurements under different conditions.

4.2.2 Potential methods to detect 1EE case: simulations and cadaveric measurements

As previously highlighted, detecting 1 or 2 EEs using EFIs has been notably challenging due to their proximity to the round window, resulting in similar characteristics to the intracochlear electrodes. This section introduces alternative methods, specifically focusing on the proposal of a novel approach — bipolar EFI, which offers potential advantages in discerning 1EE cases without the need for a CT scan.

In standard monopolar EFIs, the stimulating current flows directly to the ground electrode, creating a broader voltage spread along the CI. In contrast, bipolar EFI directs the stimulating current from one electrode to an adjacent electrode, significantly reducing the voltage spread along the CI. While the amplitude of bipolar EFI is smaller than its monopolar counterpart, it exhibits increased sensitivity to local changes in electrode status, making it a promising candidate for detecting 1 or 2EE cases.

This experimental approach was executed through simulations and cadaveric measurements for mutual validation. In the cadaveric experiment, a fresh-frozen human cadaveric head was employed. The fresh-frozen human cadaveric heads were obtained from the Anatomy Gifts Registry (USA) for use in surgical training and research at a well-established surgical training facility within our institution. The execution of this study received approval from our institutional Human Biology Research Ethics Committee, under the project number HBREC.2018.25. A HiFocus 1J lateral-wall electrode Cochlear Implant from Advanced Bionics was inserted into the cochlea, with connection to the HiRes90K receiver stimulator. Monopolar EFIs were measured using the Volta software, while bipolar EFIs were recorded with the BEDCS software, both from Advanced Bionics. Biphasic stimuli with a current amplitude of 50 μA and a single-phase duration of 200.25 μs were utilized for the bipolar EFI measurement. The cochlea was flushed with 1% saline before CI insertion, and excess saline was present in the middle ear outside the round window.

In both simulation and cadaveric experiments, normal monopolar EFIs and bipolar EFIs were measured under three CI insertion scenarios: full insertion, 1EE, and 2EE. For simulations of the 1EE and 2EE cases, corresponding models were constructed with a saline model outside the round window, as depicted in Figure 4.5.

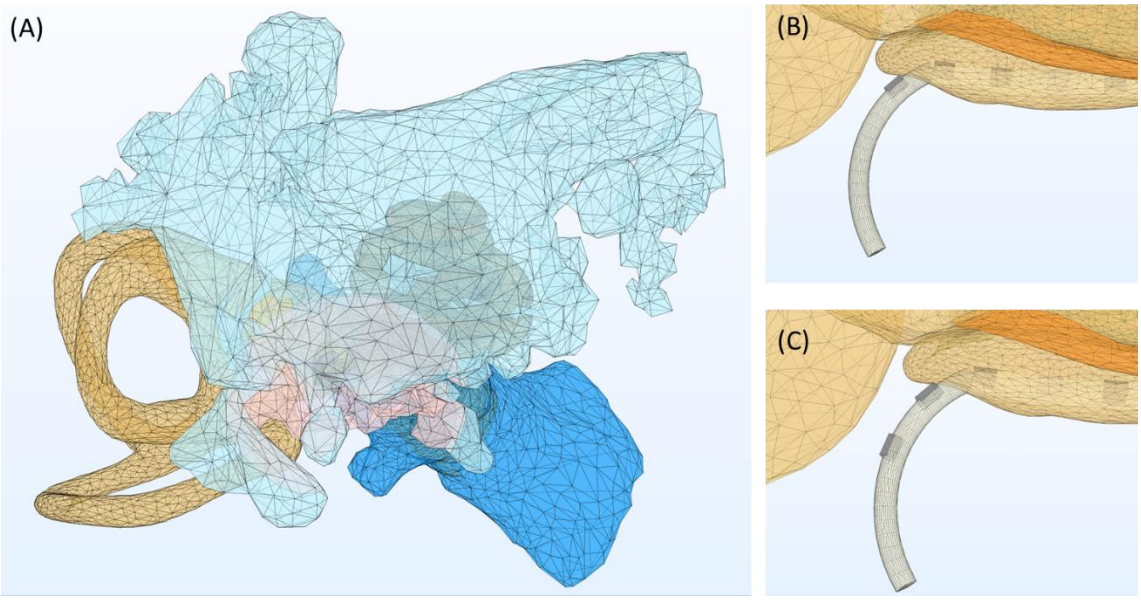

Figure 4.5: Modelling of 1 or 2EE cases. (A) The model of saline inside middle ear. (B) The model of CI with 1EE. (C) The model of CI with 2EE.

Figure 4.6 displays simulated and cadaveric (monopolar) EFIs. Despite different absolute shapes, as expected, both exhibit consistent trends. The 1EE configuration shows minimal detectable features on the 1EE itself. The 2EE results begin exhibiting subtle EE features such as basal crowding of the EFI profiles, but remains difficult to discern.

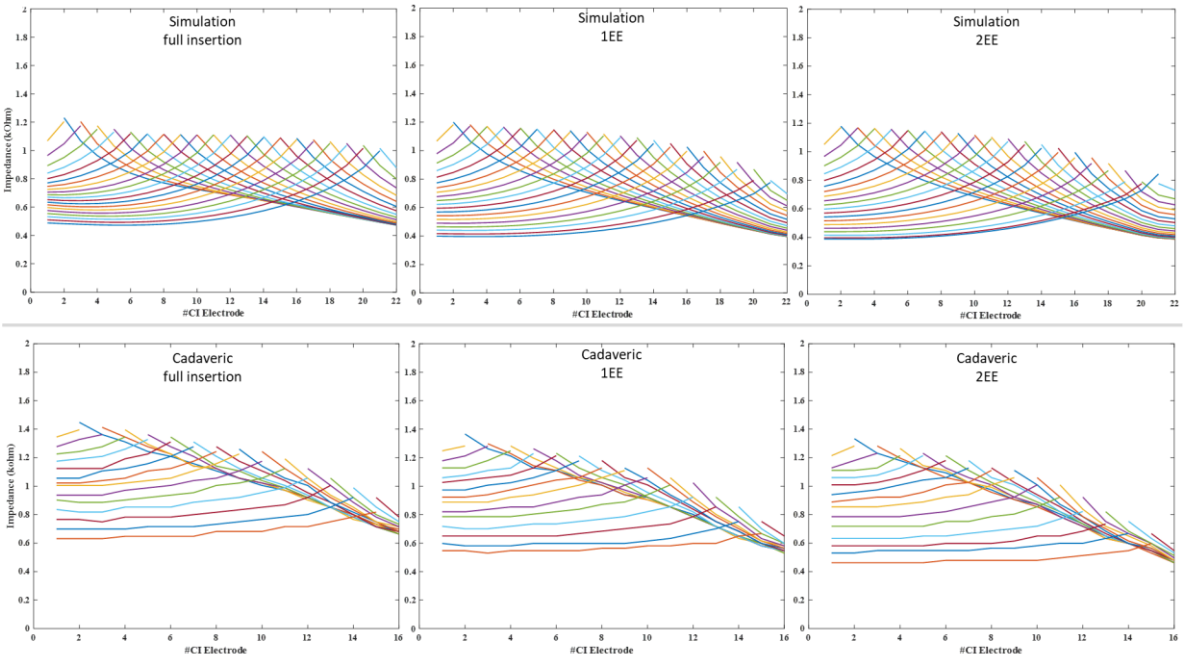

Figure 4.6: EFIs from simulation and cadaveric measurements in 3 cases. The EFIs show a similar trend that 1EE and 2EE cases are relatively identical to full insertion.

The bipolar EFIs in Figure 4.7 show a different perspective. The shape of bipolar EFIs are basically two parts of symmetric curves. The simulation predicts that in the full insertion case, the tip of each curve in both the negative and positive part of bipolar EFI will align uniformly. If 1 or 2 electrodes are extra-cochlear, the corresponding curve will shrink at the basal part, as indicated by the bold arrow.

The simulations tend to show the results in an ideal case. In cadaveric, the results did not turn out to be as perfect. In the 2EE case, this pattern is consistent as in simulation. Comparing to the full insertion case, the curves at the basal part shrank, despite the very similar monopolar EFIs. However, in the 1EE case, this pattern is not as obvious as predicted. This could be caused by the complex environments in real measurements.

Notably, in cadaveric results, the impedances of each electrode vary, causing individual curves to be at different levels. Thus, vertically shifting some curves is necessary to align all curves to match the simulations which assume completely identical impedances. This does not alter the shape of individual curves, so it does not impact the detection of extra-cochlear electrodes.

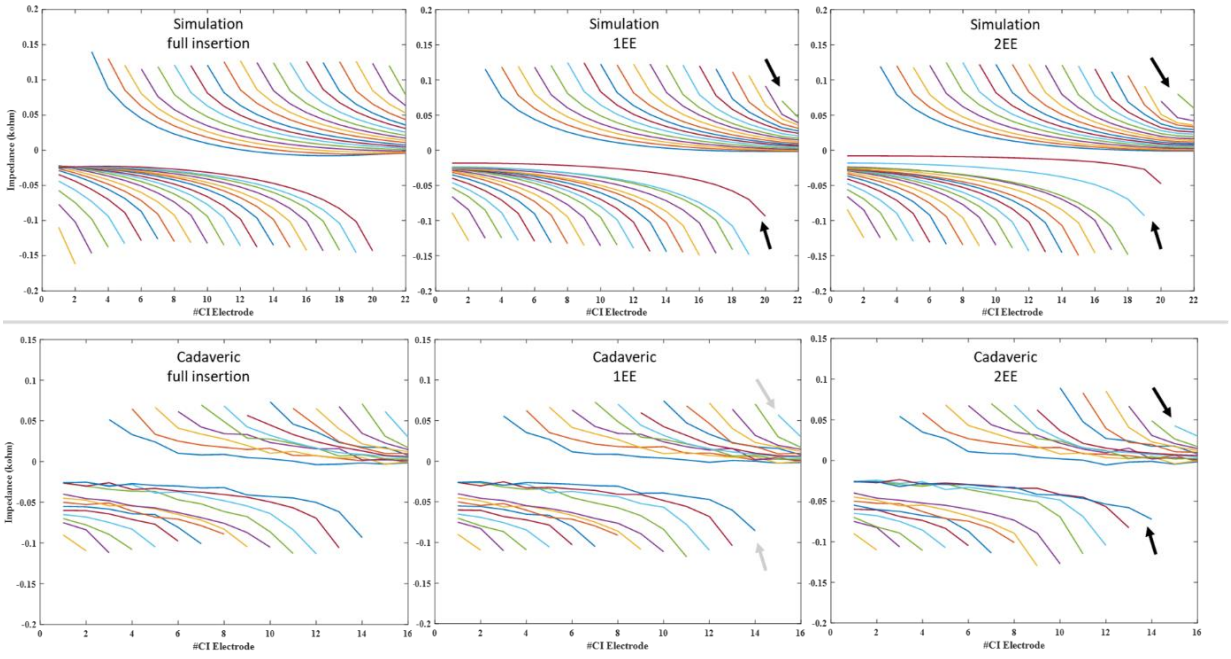

Figure 4.7: Bipolar EFIs from simulation and cadaveric measurements in 3 cases. The simulated EFIs predicts the basal curve shrink when 1EE and 2EE, and the 2EE case in cadaveric is just as predicted. The 1EE cadaveric case did not show obvious shrink.

The detection of 1EE in CI patients has been a significant challenge, necessitating the development of innovative methods. Another promising technique is 4-point impedance measurements. This approach, as outlined in references[123,124], has been developed to monitor CI status in patients, particularly blood around the implant. Essentially, for a group of 4 electrodes, the outermost 2 are the current source and sink and the voltage difference between the two inbetween electrodes (which are not conducting current so are not affected by electrode-electrolyte factors) is measured. Mirroring the principle of using bipolar EFIs, the 4-point impedance measurements focus on amplifying local changes in electrodes, thereby offering enhanced sensitivity.

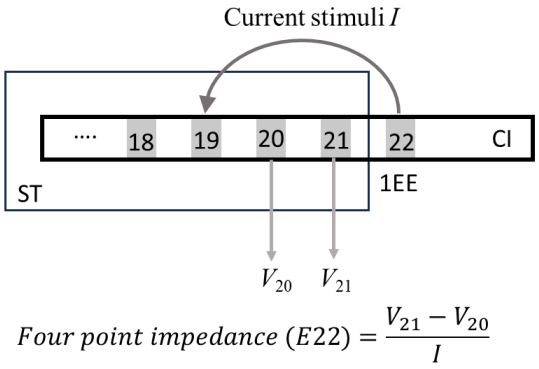

Figure 4.8: Schematic of 4-point impedance measurement. This figure takes E22 as an example of a 1EE case.

For the simulation, impedance measurements spanned the entire array, ranging from E22 to E4. The underpinning models remained consistent with those used for bipolar EFI, as depicted in Figure 4.5. The stimulation current was set at 500 µA, but its amplitude does not influence the calculated 4-point impedance. This is illustrated in Figure 4.9, presenting results across the three insertion scenarios: full, 1EE, and 2EE.

The simulated 4-point impedance yields a scale ranging between 200 to 300 Ω, aligning with reported patient values[124]. Notably, the 1EE and 2EE scenarios exhibit a conspicuous fluctuation, primarily downward, at the basal electrodes, while the full insertion scenario maintains a consistent profile. Unfortunately, due to my limited access to cadaveric resources, this part of the study was not validated with cadaveric experiments. As a result, the effectiveness of this method in real-world measurements, particularly under conditions with noise, remains to be validated.

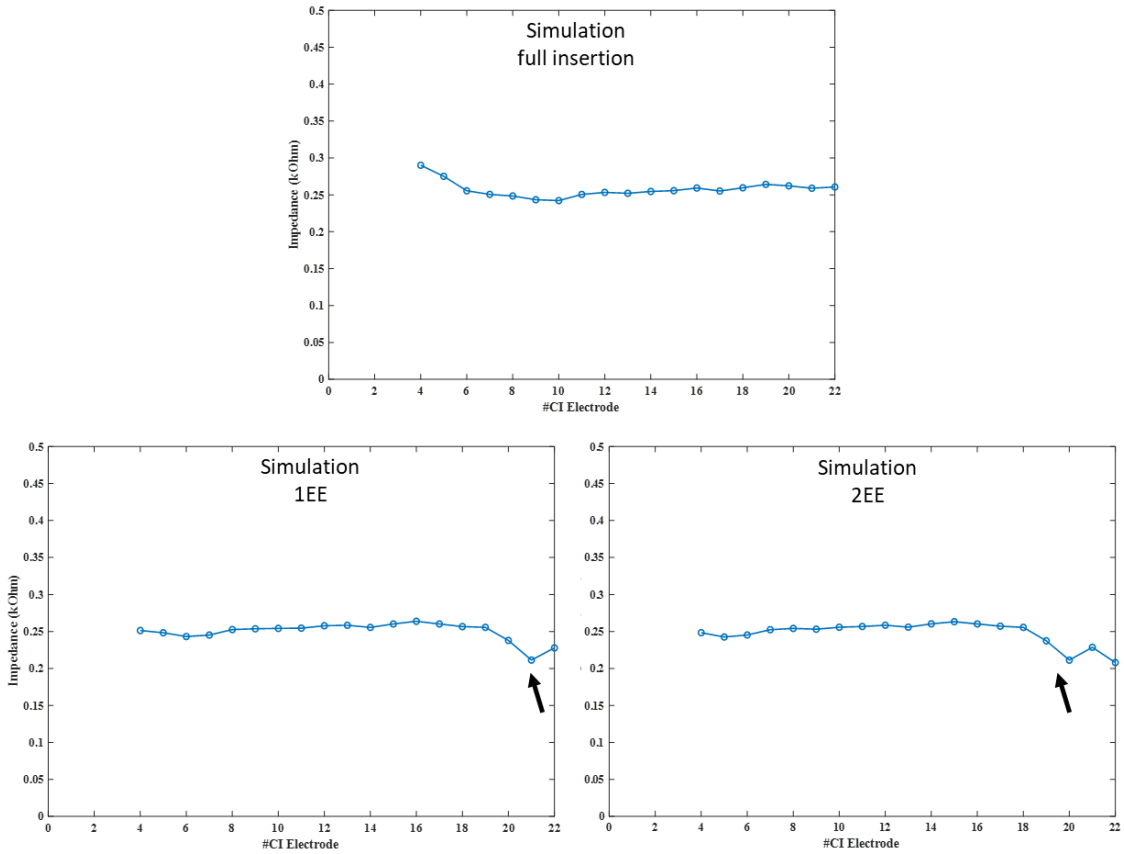

Figure 4.9: Simulation results of 4-point impedance in 3 cases. The 1EE and 2EE cases show an obvious drop at the most basal electrodes, while being flat in full insertion.

In summary, this work introduces and evaluates the potential efficacy of two prospective methodologies for the identification of 1EE in CI recipients. The foundational premise revolves around the amplification and discernment of local voltage or current perturbations induced by EEs. While these simulations offer promise, their translation to clinical viability requires further validations through patient-based investigations.

4.3 Electrode Shortage and CI Induced Scalp Voltage

In this section, I focus on replicating two more clinical measurements — EFIs in the presence of electrode shortages and the scalp voltage resulting from CI stimulations. Scalp voltage has been reported as a diagnostic tool for detecting full insertion, extra-cochlear electrodes, or partial shorts[121]. The simulation in this section aims to validate the computational head model by replicating scalp voltage outcomes in these three distinct cases.

4.3.1 Electrode shorts to ground.

Electrode shorts to ground, either partial (difficult to detect) or full represent a common failure mode in CIs, typically identified through lowered electrode impedances, commonly considered problematic when falling below 1-2 kΩ[125]. Short circuits can manifest as either electrodes being shorted to the ground or to each other. Both scenarios are individually modeled in this section, with simulated EFIs modelled for use as potential clinical tools.

In Figure 4.10A, the modelled CI for electrode shorting simulations incorporates conducting wires connected to the four most basal electrodes to facilitate current conduction between them. Figures B and C illustrate how shorts to the ground or to each other are simulated.

The simulated EFIs and electrode impedances, presented in Figure 4.11, demonstrate clear distinctions between the two shortage cases. Despite exhibiting similar impedance profiles, the EFIs differ significantly. In the short-to-each-other scenario, where the four basal electrodes are interconnected, a distinct bump in EFI occurs when any one of the electrodes is stimulated. Conversely, in the short-to-ground scenario, the EFI collapses due to the voltages of the basal four electrodes converging towards zero. Please note that in scenarios where electrodes are shorted to each other, I have assumed direct contact between the shorted electrodes, resulting in zero impedance. This assumption is made to provide a typical example for reference purposes.

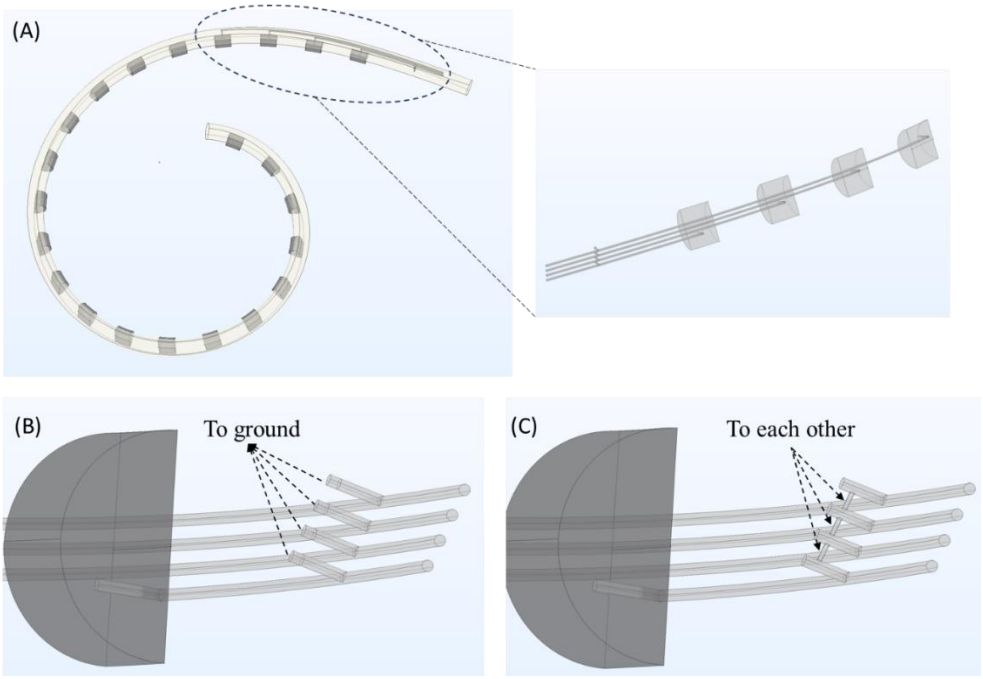

Figure 4.10: Modelling of electrode shortage. (A) The conducting wires connecting the four most basal electrodes. (B) Wires connecting to ground through a shortcut. (C) Wires connecting each other.

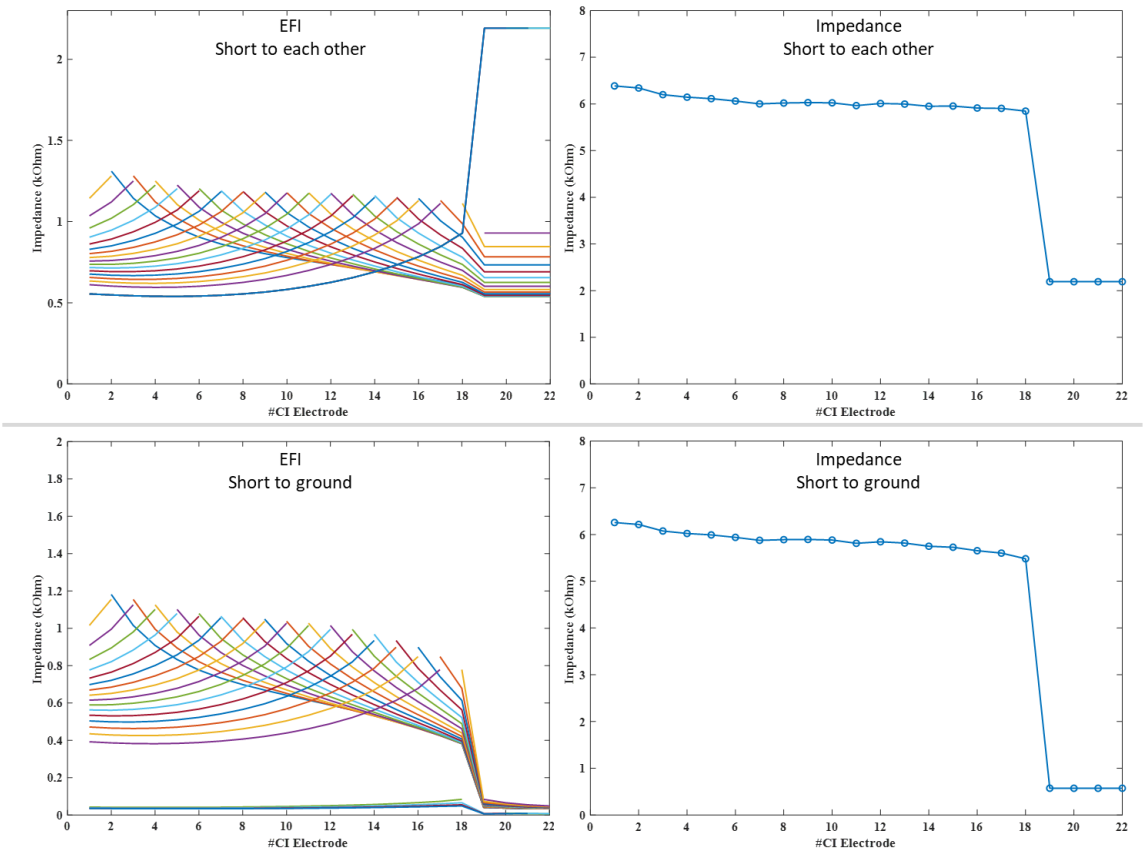

Figure 4.11: Simulated EFIs under electrodes shortage. The upper two figures show the EFI and impedance with the four most basal electrodes shorted to each other. The lower two figures are when the four most basal electrodes are shorted to the ground.

4.3.2 Scalp voltage

This section seeks to simulate real CI stimulation-induced patient scalp voltage measurements previously conducted and published by our group[121], using computational simulations to validate the accuracy and fidelity of the head model. The simulations account for three distinct conditions: a normally functioning CI, the presence of extra-cochlear electrodes, and partial electrode shortages. The resulting simulated scalp voltages are subsequently juxtaposed against the actual clinical measurements to assess alignment and consistency.

To ensure precise replication of clinical measurements, the simulation aligns the positions of the recording electrodes as depicted in Figure 4.12, as they were used clinically. The ground electrode is positioned at the nape, serving as a general reference, while two measuring electrodes (channels) are strategically placed at the forehead and the contra-lateral mastoid. The measured scalp voltage, under this configuration, represents the voltage difference between the forehead and the mastoid. In the clinical measurements, CI stimulation utilized 120 clinical units with a 75 μs pulse, and the conversion equation from Clinical Units (cu) to microamperes (μA) is derived from Advanced Bionics[126]:

$$cu = I(\mu A)/2040 * t(\mu s)/229 * 6000$$

The actual current amplitude is 124.6 μA.

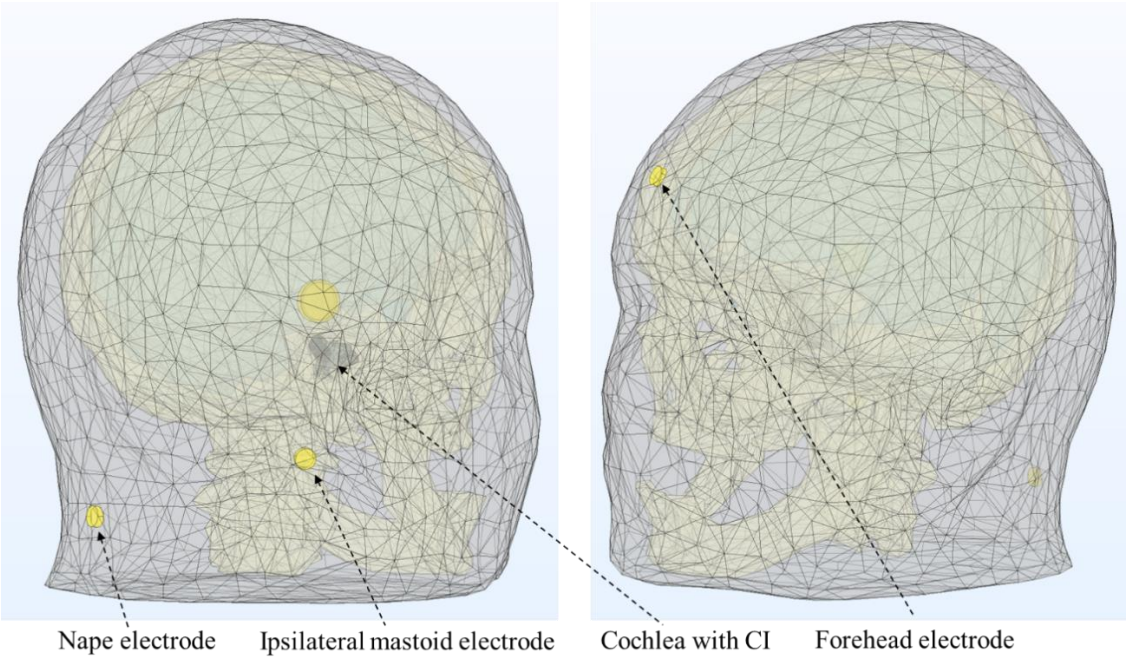

Figure 4.12: Electrodes placed on scalp. The nape electrode is set to be ground. Voltage is measured from the forehead and contralateral mastoid electrode.

Figure 4.13 provides a visual comparison between simulated scalp voltages and clinical measurements across three distinct scenarios: normal CI, CI with known partial short circuiting to ground, and the presence of EEs. These simulation results were derived from the same models as in Figures 4.2, 4.4, and 4.11, with the primary modification being the addition of scalp electrodes onto the model's scalp. The stimulation current for all simulations was set at 124.6 μA, matching the current used in the clinical measurements[121], thereby allowing for direct comparison. Additionally, to align with the patient data—which originated from CIs with 16 electrodes, while the simulations used 22 electrodes—the patient data was appropriately adjusted.

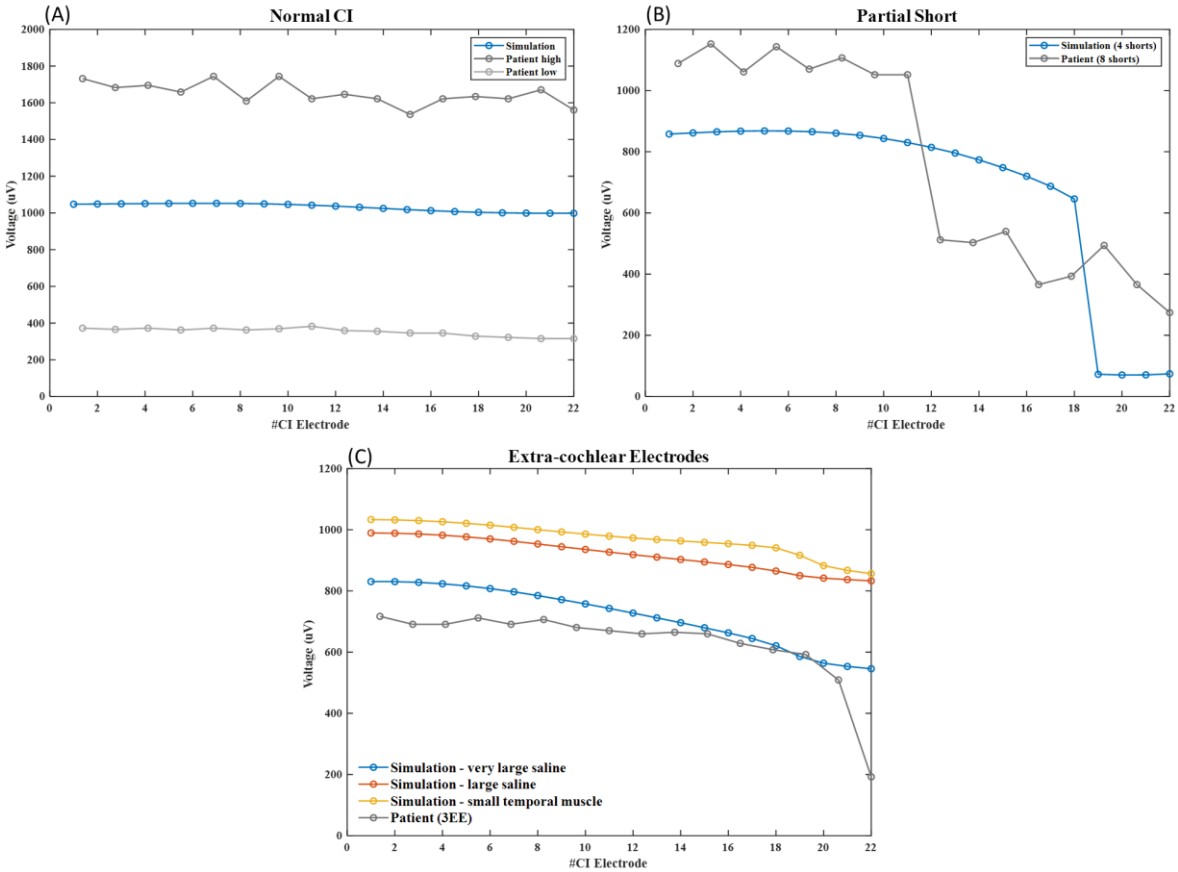

Figure 4.13: Simulated scalp voltage in 3 different cases. (A) Scalp voltage in the normal CI case. Two different patient data sets are shown. (B) Scalp voltage in partial short CIs. The electrodes are shorted to the ground. (C) Scalp voltage in extra-cochlear CIs. Three different simulation cases are shown. All the patient data come from another publication from our group[121].

In the typical CI scenario, scalp voltage amplitudes typically range from a few hundred to two thousand microvolts. The simulated scalp voltage in our study measured around 1000 μV, a range consistent with typical patient values. Notably, when electrodes were shorted to the ground, a substantial decline in voltage was observed at the basal electrodes. Figure 4.13B illustrates this phenomenon, indicating a drop in approximately 8 electrodes

in patient cases. The simulation replicated this effect with 4 shorted electrodes, displaying comparable sharp declines.

The extra-cochlear scenario was more complex. Figure 4.13C presents three simulation cases: one with saline filled the whole middle ear(same saline model as in Figure 4.2, labelled "very large saline"), another with a large saline volume (same saline model as in Figure 4.4 case 1, labelled "large saline"), and a third with a small amount of temporal muscle (same soft tissue model as in Figure 4.4 case 4, labelled "small temporal muscle"). Despite variations, all three extra-cochlear cases exhibited a voltage drop at the basal electrodes. For simulations, this was not as large as that seen in the patient, but shows similar trends. In the other scenarios, the simulated scalp voltages in these diverse conditions closely resembled real-world clinical data.

4.4 Discussion

This chapter delves into specific clinical measurements using the head model, particularly focusing on extra-cochlear electrodes. The EFI in these cases is found to be correlated with the findings in which we have blood, saline or soft tissue surrounding the extra-cochlear part of the CI. The exploration also suggests more sensitive potential methods for detecting only 1EE conditions. In addition, we model scalp voltages to effects expected for extra-cochlear and electrode shortage scenarios. The simulation results exhibit a general similarity in trend and amplitude to clinical measurements, affirming the validity of the head model constructed in Chapter 2 across different aspects of clinical conditions.

Despite these positive outcomes, certain limitations should be acknowledged. In the extra-cochlear study, the simulation relies on estimated amounts of soft tissue in the middle ear, lacking detailed records from the clinical experiment. This absence may introduce inaccuracies, but the primary focus of this simulation work is on understanding basic trends and validating the model. Notably, the overall trend of simulated EFIs in extra-cochlear cases aligns with clinical measurements, suggesting that the detailed amount of soft tissue present may not be crucial.

Another limitation arises from the exploration of two methods to detect 1EE through experiments, with only one cadaveric head included in this study. The cadaveric data, while not as idealized as simulations, points to the need for further validation with a larger sample size, but supports the model findings.

Additionally, the head model's purely resistive nature introduces potential deviations from real patients. While the detailed impacts of not having a dynamic model are challenging to estimate, the study's focus on steady-state clinical EFIs and voltages minimizes concerns about temporal effects.

Future work could expand the applications of the head model. One promising application involves exploring the stimulation of the facial nerve by incorporating a facial nerve model into the head. This could shed light on the presence of facial nerve stimulation in a subset of patients[127]. Other potential applications include investigating CI insertion trauma, the effects of fibrosis, and many other scenarios, providing rich grounds for further exploration.

5 COCHLEA-ON-A-CHIP MODEL FOR IN-VITRO NEURAL STUDIES: A PROOF-OF-CONCEPT DESIGN

This chapter introduces a proof-of-concept design for spiral ganglion neuron studies. Drawing on the simulation results of voltage spread within the head in Chapter 3, a model for in vitro neuron culturing and recording is proposed. The design is grounded in simulation data, and the structures outlined could be implemented in subsequent physical experiments.

5.1 Introduction

Understanding how spiral ganglion neurons (SGNs) respond to electrical stimulation is pivotal for evaluating cochlear implant outcomes[74,128]. However, research in this area faces challenges due to the cochlea's deep embedding in bone making it inaccessible, and the limited number of SGNs compared to other neurons in humans[129]. In vivo studies are invasive and fraught with difficulties, making in vitro studies more feasible[130,131]. Insights into SGN responses can significantly enhance auditory nerve models[132,133].

To observe SGN activities under electrical stimulation in vitro, typical techniques include patch clamping and micro-electrode arrays (MEAs), with rat SGNs frequently used as subjects. Patch clamping, well recognised as the definitive method for analysing neuron activities, has been effective in single SGN studies[134,135]. Nevertheless, this approach becomes laborious when examining larger neuron populations, typically looks at neurons in isolation, and offers mostly intracellular stimulations (or extracellular stimulation with external stimulating electrodes), markedly different from the stimulation mechanisms in CIs. MEAs, alternatively, involve culturing dissected SGNs on substrates embedded with electrodes. These electrodes are capable of both recording spontaneous activities and applying current stimulations[136,137]. For both patch clamp and MEAs, discrepancies remain in fully understanding and replicating the voltage distributions and electrode-neuron interactions they would experience in-vivo.

In light of cochlear anatomy and the findings from Chapter 3, it is clear that the response of SGNs to CI stimulation is largely influenced by the voltage gradient along the neuron, particularly at the peripheral dendrites, soma, and the axon near the internal auditory meatus (IAM). A key question thus emerges: can we replicate in an in vitro setting of the voltage environment experienced by SGNs in the cochlea during CI electrode activation? Such a methodology could enable more accurate investigations into SGN responses for future experiments with cultures of populations of SGNs on MEAs.

A prior study from our group[138] introduced a "cochlea-on-a-chip" concept, involving the culturing of SGNs in a confined chamber and using CIs for stimulation (utilizing MEAs). Although this study proved the viability of culturing SGNs in constrained spaces, it did not incorporate electrical designs to mimic the actual voltage dynamics within the cochlea.

This chapter introduces a novel design focused on electrical modulations. The objective is to ensure that, during CI electrode stimulation, the SGNs experience a voltage spread similar to that encountered along their structure in vivo, from dendrites to axon. This development leverages the model and findings of Chapter 3, seeking to create a more accurate and physiologically relevant environment for studying SGN responses under CI stimulation.

5.2 Model Design

Drawing from the cell culture techniques elucidated in our earlier research[138], we propose culturing SGNs within a model composed of several partitions. I optimised the simpler 2D model dimensions and shapes through numerous iterations over many months to arrive at a model that mimicked the electrical fields in different compartments in the whole head model.

Typically, the cell bodies are positioned in a central chamber that represents Rosenthal's canal (RC). To ensure the unobstructed flow of the cell culture medium and to restrict the migration of cell bodies, small channels are integrated between the compartments. Anchoring the cell bodies within the RC compartment enables us to direct their axons towards the IAM compartment, and the dendrite to the CI compartment using neurotrophic factors. This strategic placement ensures the axons grow in the intended direction, allowing the anatomy-based cell culture model to function optimally. Figure 5.1 offers a foundational representation of the model design, which is inspired by cochlear anatomy. (For details on SGN growth within such models, please refer to our previous work[138].)

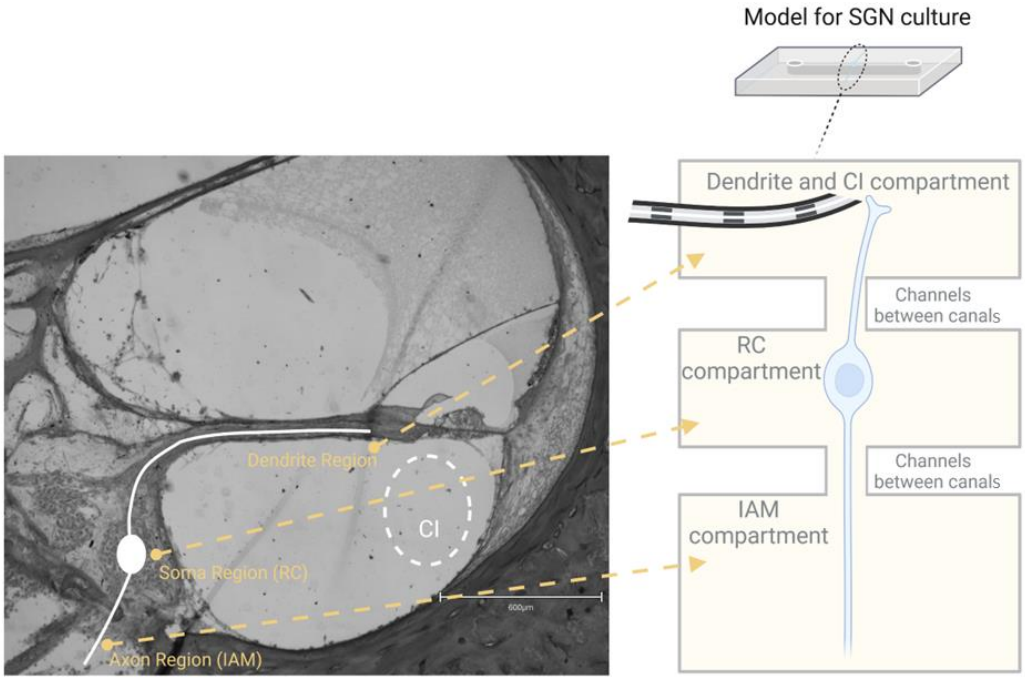

Figure 5.1: Concept of spiral ganglion neuron (SGN) culturing in cell culture models. The left diagram showcases the cochlear anatomy, while the design on the right portrays the model. Channels between the compartments, although just one is depicted, prevent unwanted cell body migration. Figure created using Biorender®.

Though just one small channel is depicted for simplicity in Figure 5.1, these channels are pivotal in determining the voltage spread from the CI to each compartment. The modulation of voltage across the SGNs, spanning from dendrites to axon, heavily depends on the dimensions of these channels. With this design paradigm, our goal is to try to replicate in a realistically constructable in-vitro structure that could host cultures of SGNs, the voltage or currents they would experience derived from the head model, specifically four specific points:

i. The voltage spread along CI (i.e. the EFI) representing the voltage the dendrites would experience.
ii. The voltage in Rosenthal's canal representing the soma voltage experience.
iii. The voltage at the top part of IAM representing the axon voltage experience.
iv. The proportion of current flowing through IAM (shown in Figure 3.17).

These correlations ensure that when the CI stimulates this structure, the SGNs in culture are excited in a manner akin to their natural stimulation within the cochlea, thus enabling a more realistic study of SGN responses.

The accurate replication of current pathways within the cell culture model, derived from the head model, involves several compartments representing the scala, Rosenthal's canal,

the IAM, bone, and a ground electrode. Chapter 3's analysis reveals that the current from the CI predominantly divides into two paths: one through the RC and IAM to the ground, and another through the bone to the ground (approximately 23% and 77%, respectively). The current flowing through the RC and IAM is "effective" for stimulating neurons, whereas the bone path mainly serves as dissipation pathways. When considering the scale of the cell culture model, the actual dimensions of the cochlear anatomy must be kept in mind. For instance, in the cochlea, the scala's diameter is approximately 2 mm[139]. Based on original cochlear scans, the diameter of the RC is around 0.5 mm. While the diameters of other compartments in the model can be more flexible, these measurements provide a guideline for creating a realistic and functionally relevant environment for studying SGN responses to CI stimulation.

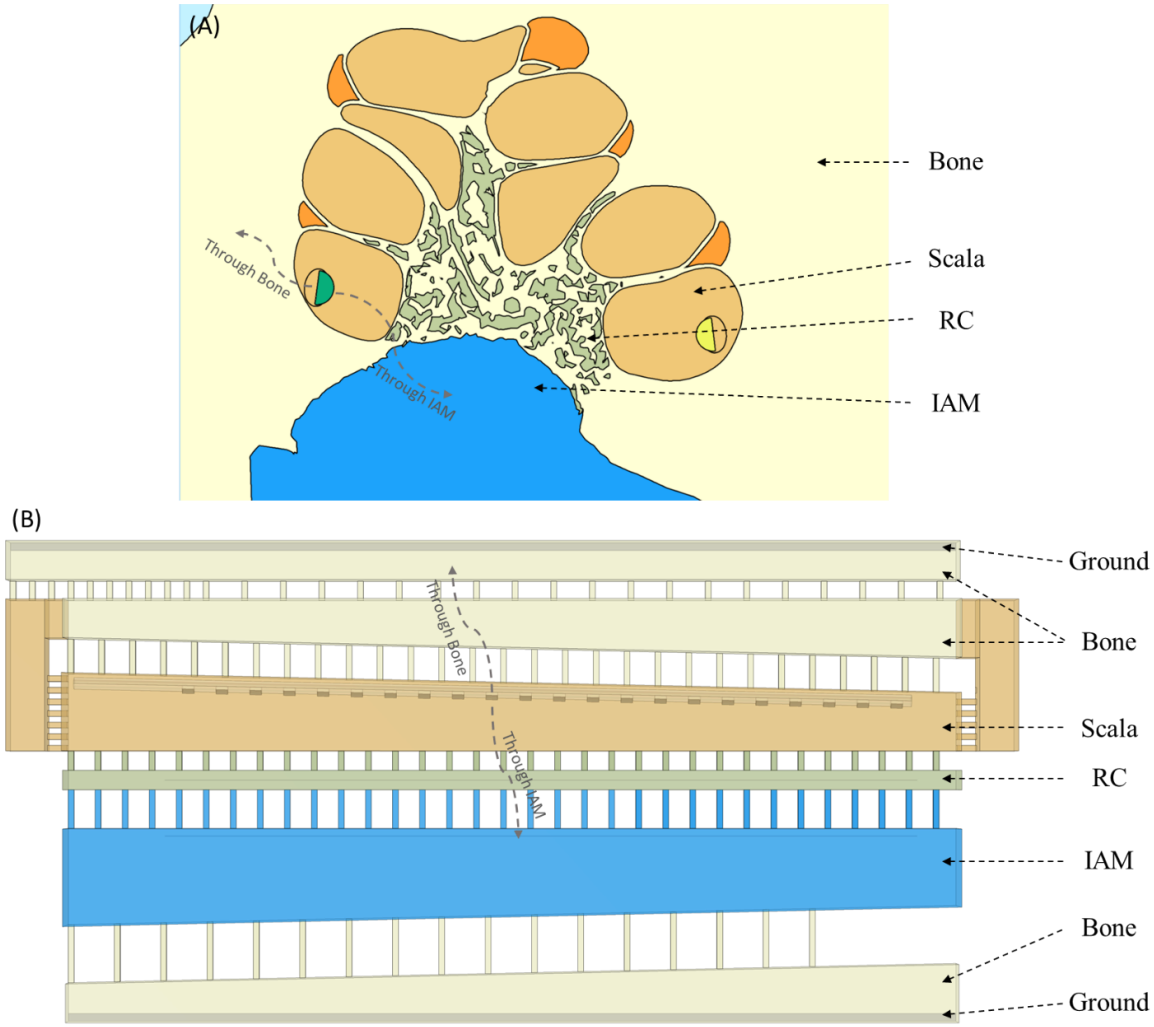

Figure 5.2: The cell culture model design and comparison to the cochlea model. (A) A cross-sectional view of the cochlea model in Chapter 3. (B) The designed cell culture model with 6 compartments representing natural cochlea-related components, also denoted by different colors. The CI is modelled, and the current pathways from CI through bone or IAM to the ground(s) are marked.

We have used simulations of the whole head movement to design this simpler representation, and align it with the current pathways and impedances we might expect in living heads. Figure 5.2 delineates the designed cell culture model and compares it with the "real" cochlea model. The cell culture model is bifurcated into two sections: the upper part signifies the current pathway through bone, while the lower part represents the RC and IAM path. Each compartment in the model corresponds to a distinct component in cochlear anatomy. Neurons will be cultured in the RC canal, and a cochlear implant will be inserted into the scala for stimulations, and for future instantiation. Neuronal activities can be recorded using MEAs or patch clamp techniques with this model. For simpler construction, and to make it compatible with flat MEAs, the cell culture model adopts a linear design as opposed to the spiral shape characteristic of the cochlea.

To physically realize this model, a 3D-printed mold of the designed structure would be created for casting. Polydimethylsiloxane (PDMS) would be used for casting, and the resulting PDMS model will be affixed to a glass substrate or MEA. Once the cell culture medium is added and the CI is inserted, this designed structure becomes ready for cell culture.

Figure 5.3 and Table 5.1 provide a detailed breakdown of the model's dimensions. To accommodate 3D printing and consider resolution limitations, all dimensions, particularly those of the small channels, are integral multiples of 50 µm.

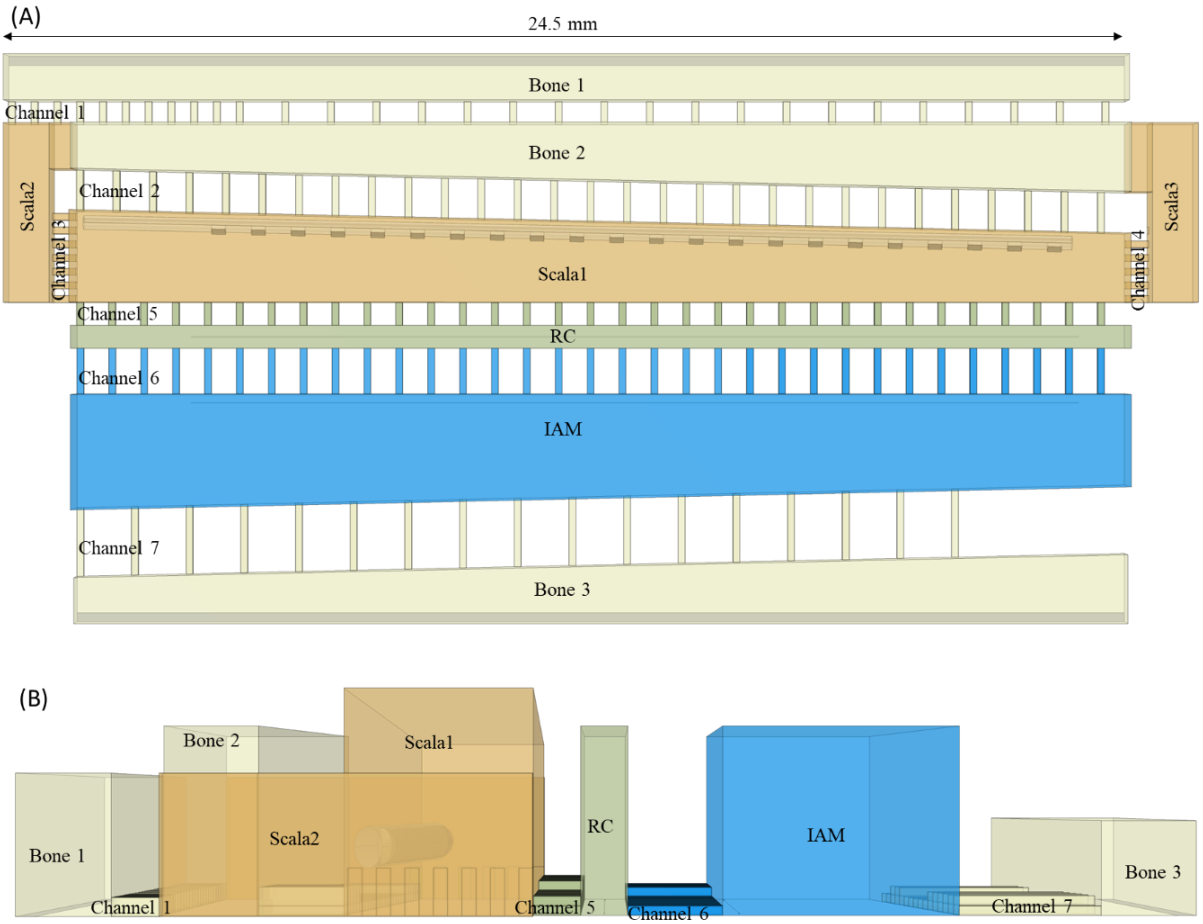

Figure 5.3: Tagged compartments and channels for dimension. (A) Top view with all components tagged. (B) Side view from the left with part of the components tagged. This model contains 6 main compartments, 2 side compartments, and 7 sets of small channels connecting compartments. The detailed dimensions are in Table 5.1.

Table 5.1 Overview of all the dimensions in the cell culture model.

Compartments				
Compartment	Left length (mm)	Right length (mm)	Width (mm)	Height (mm)
Bone 1	1	1	24.5	1.5
Bone 2	1	1.5	23	1.5
Bone 3	1	1.5	23	1
Scala 1	2	1.5	23	Left 2.4 Right 1.9
Scala 2	3.9	3.9	1	1.5
Scala 3	3.9	3.9	1	1.5
RC	0.5	0.5	23	2
IAM	2.5	2.5	23	2

Table 5.1(Continued) Overview of all the dimensions in the cell culture model.

Channels					
Channel	Number of channels	Length (μm)	Width (μm)	Gap (μm)	Height (μm)
1	30	500	150	First 11: 350 Last 19: 850	200
2	29	900	150	650	First 6: 300 Middle 17: 100 Last 6: 200
3	7	150	500	150	500
4	5	150	500	150	400
5	33	500	150	550	First 15: 200 Last 18: 300
6	33	1000	150	550	First 21: 100 Last 12: 300
7	17	1500	150	1050	1st, 8th to 12th, 16^{th,} 17th: 100 2nd to 7th, 13rd to 15th: 200

The parameters of these complex channels are fine-tuned based on the results from simulations. The first channel in the table denotes the leftmost one. The conductivity parameters are shown in Table 5.2, which are the same as in chapter 3. All the parameters of the small channels modulating the whole voltage spread is adjusted and optimized manually by many iterations of simulations. The conductivity of cell culture media is reported to be between 1.5 to 2 S/m[140]. This work takes an approximate median value 1.8 S/m. The simulation results of cell culture model in comparison with head model are presented in the next section.

Table 5.2 Overview electrical conductivities in the cell culture model.

Model	Material	Conductivity (S/m)
Compartments	Cell culture media	1.8
Channels		
CI body	Silicone	0
CI electrode	Platinum	9.4E6

5.3 Simulation Results

Examining the outcomes of the cell culture model, the simulated voltage spreads along the cochlear implant (CI), in Rosenthal's canal (RC), the top part of the internal auditory meatus (IAM), and the current proportion through IAM are evaluated across all 22 CI electrodes. These results are presented alongside those from the head model for comprehensive comparison.

Figure 5.4 showcases the EFIs of the simulated CI in the cell culture model in contrast to the head model. While the EFIs in the cell culture model have been adjusted to approximate those in the head model, the linear nature of the cell culture model contrasts with the curved EFIs in the head model, reflecting the spiral shape of the natural cochlea.

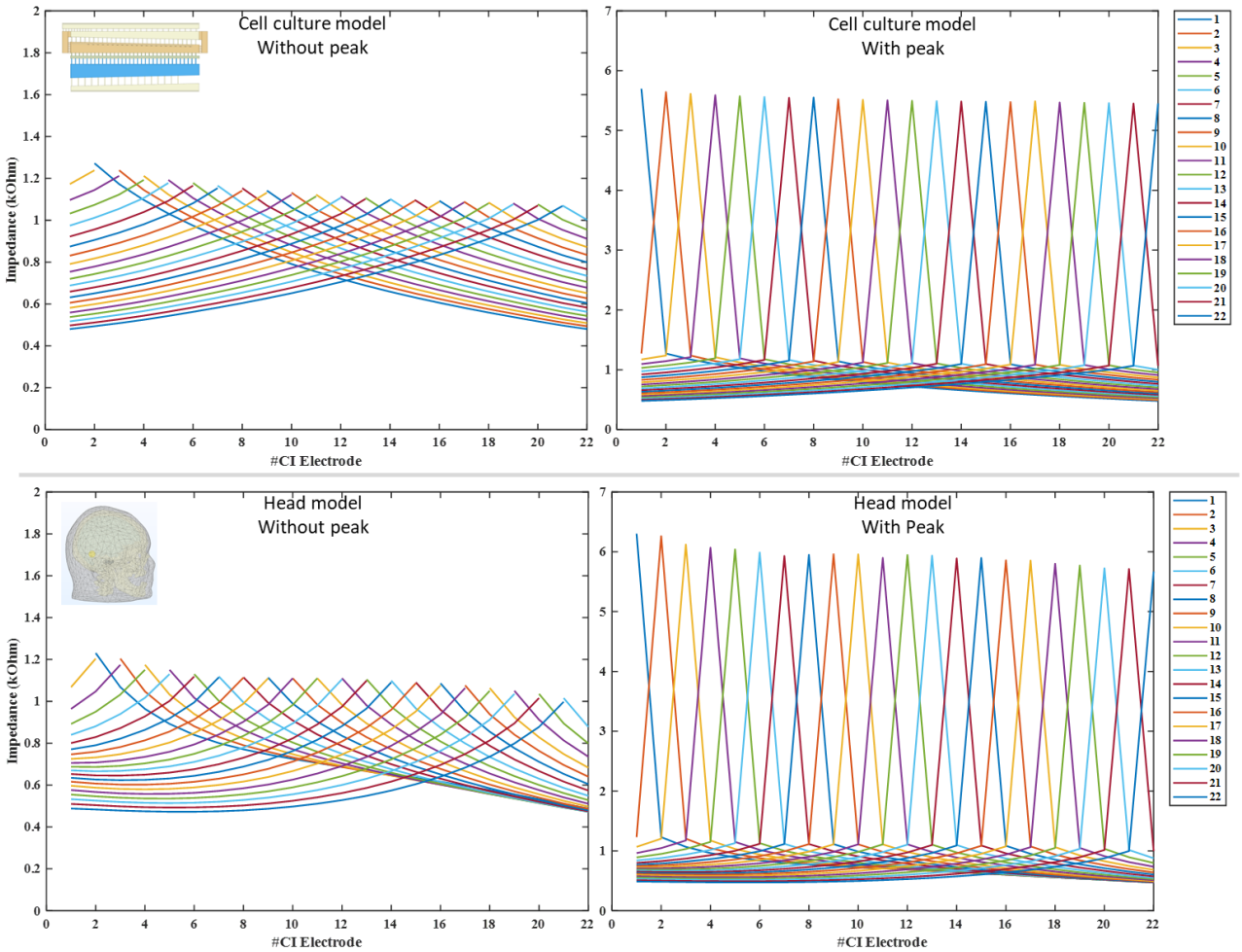

Figure 5.4: Simulated EFIs of the cell culture model in comparison to the head model. The EFIs include both with and without peaks (the impedance of electrodes).

Moving to RC compartment voltages, Figure 5.5 illustrates the defined postion curves used to extract the expected RC voltage in both models. In the head model, the curve follows the spiral shape and stays in the middle of the RC model. In the cell culture model, the voltage curves align with the center of the RC canal.

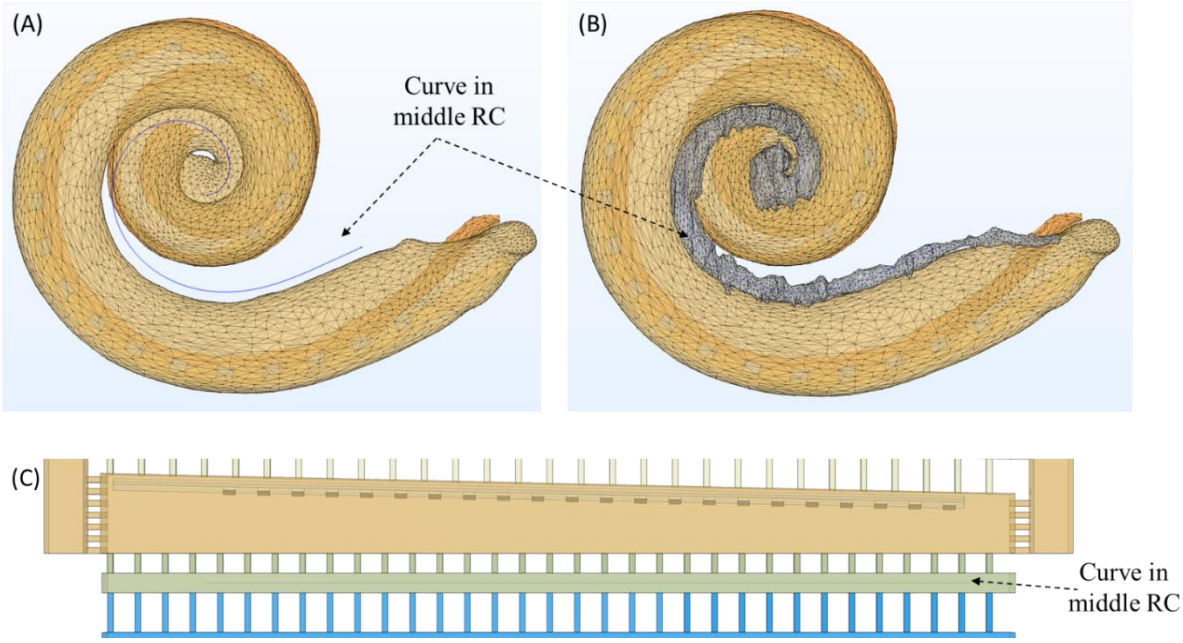

Figure 5.5: Defined RC curves for extracting RC voltage. (A) The RC curve along the spiral shape in the head model. (B) The RC curve overlaps with the RC model. (C) The RC curve in the cell culture model.

The extracted voltages along these RC curves are compared in Figure 5.6. Stimulation currents are set at 500 µA for each individual CI electrode. The voltages exhibit similar shapes (envelopes) and amplitudes, with smoother results in the cell culture model, attributed to the absence of porous modiolus-induced fluctuations seen in the head model. Importantly, due to the length discrepancy of the curves in the head model and the cell culture model, the results are plotted with relative distances. This approach is also applied to the results in IAM voltage.

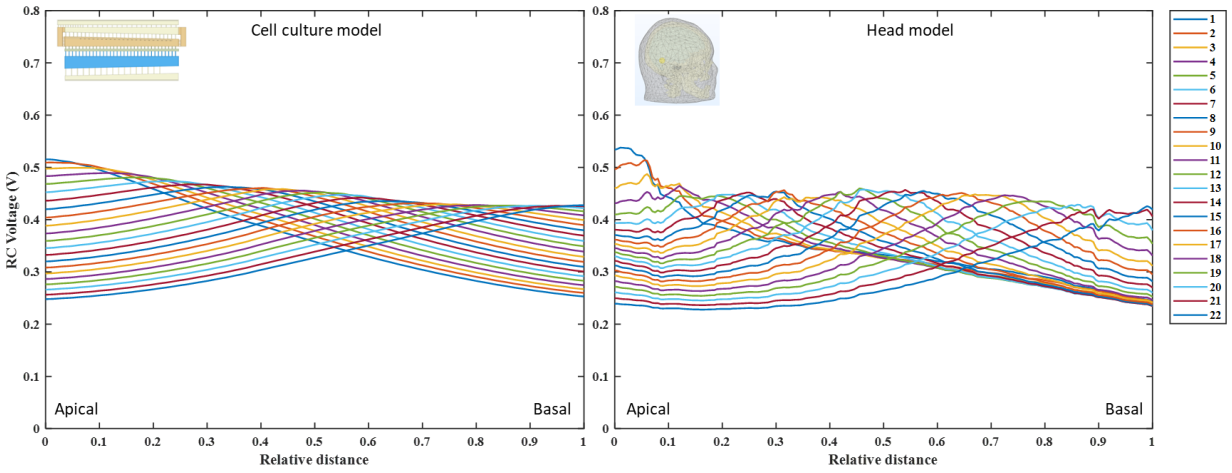

Figure 5.6: RC voltages in cell culture model and head model. Both voltages are similar in amplitude range and trend.

Continuing the analysis, the third segment involves fitting voltages at the top part of the internal auditory meatus (IAM). Similar to the approach with RC, curves are defined in both models to extract voltages. Figure 5.7A depicts the curve beneath the modiolus in the head model (IAM hidden for clarity), while Figure 5.7B provides a bottom view, including IAM. In the cell culture model, the curve is within the IAM canal and in close proximity to the RC canal.

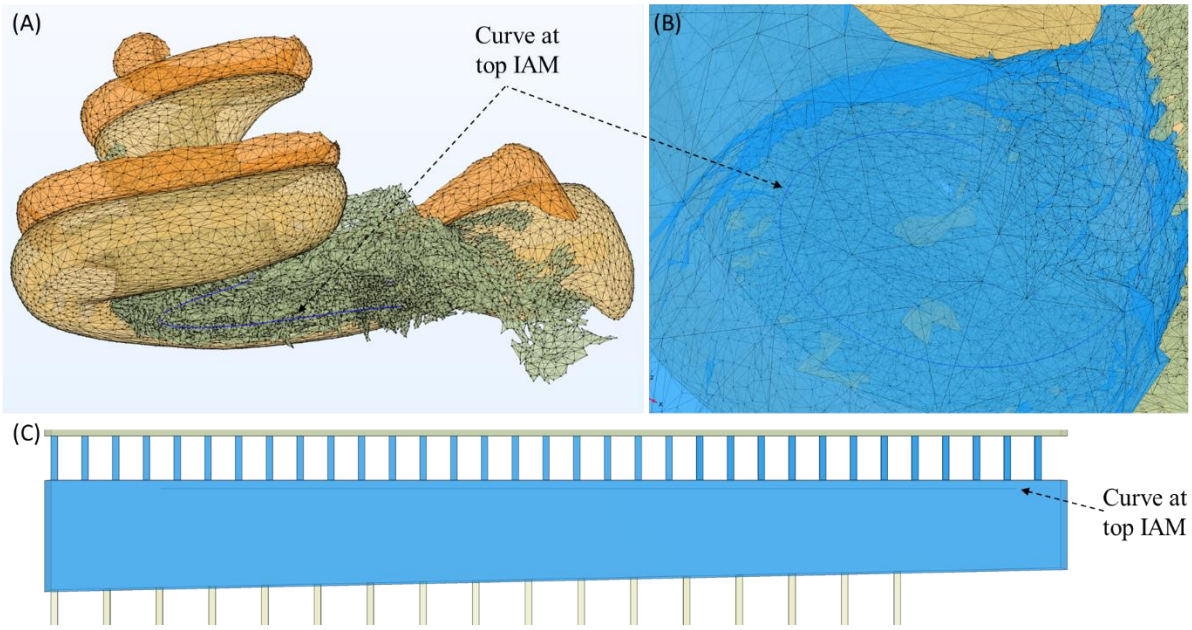

Figure 5.7: Defined top IAM curves for extracting IAM voltage. (A) The top IAM curve beneath modiolus in the head model. (B) The top IAM curve viewed from the bottom with IAM included. (C) The IAM curve in the cell culture model.

Figure 5.8 shows the simulated IAM voltages, with stimulation currents set at 500 µA from each CI electrode. The fluctuations in the cell culture model are attributed to small

discrete channels that conduct ionic currents from one compartment to anothers, near the IAM curve, an inevitable but minor issue. While the voltages in the head model exhibit a rapid change in the apical part that is challenging to replicate in the cell culture model, both voltages fall within the same amplitude range and demonstrate a similar trend.

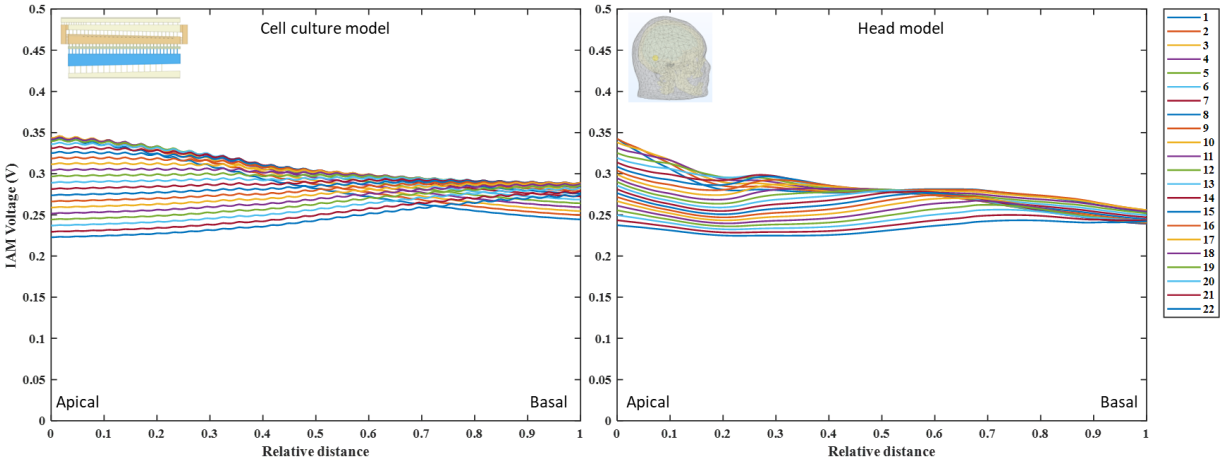

Figure 5.8: IAM top part voltages in cell culture model and head model. Both voltages are similar in amplitude range and trend.

The final step involves fitting the proportions of current through IAM. To calculate this, two boundaries are chosen, one in the cell culture model and another in the head model. In the cell culture model, the upper surface of the IAM canal, connecting to the RC canal through channels (Figure 5.9A), serves as the boundary. The current flow through these channels is calculated. In the head model, the results align with those presented in Figure 3.17, indicating that roughly 23.4% of the current from the CI flows through IAM. Comparatively, in the cell culture model, approximately 21.4% of the current flows through the IAM canal. The results demonstrate a close match between the two models.

5.4 Discussion

The exploration and presentation of the cochlea-on-a-chip concept underscores the continual advancements being made in the realms of biomedical engineering and neuroscience. This chapter has indeed provided insight into the development of a completely novel cell culture model that has the potential to emulate the electrical responses of Spiral Ganglion Neurons (SGNs) when exposed to Cochlear Implant (CI) stimulations.

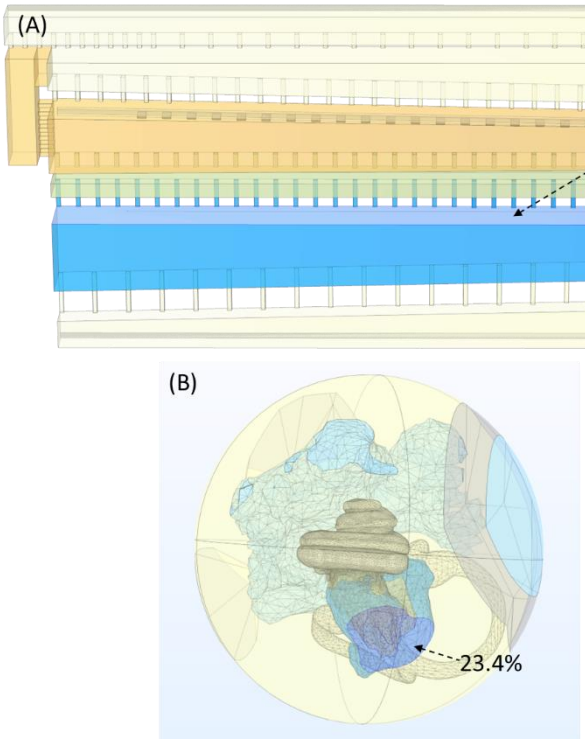

Figure 5.9: Current proportions through IAM. (A) The boundary defined at the upper IAM is highlighted. Current through all the connected channels is calculated to be 21.4%. (B) Boundary at IAM in head model is highlighted. Current through this boundary is 23.4%.

While this work provides insights into in vitro SGN studies, a few limitations should be acknowledged. Firstly, the current findings are based solely on simulations, although the head model has been validated against human and cadaveric data, the 2D model has not, and physical measurements are left for future development. The detailed voltage values may vary between simulation and physical measurements, but the presented method serves as a universal proof-of-concept design, allowing for individual modifications in channels and compartments design, possibily to mimic patient differences or cochlear malformations. Additionally, in order to optimize the 2D model, particularly the dimensions of the small channels that modulate the voltage distribution, the process still relies heavily on manual works. In theory, this optimization could be automated by inputting a few target voltage distributions into some program. However, as this task will be labor-intensive, I was unable to complete the automation process.

Another limitation lies in the feasibility of physical processing. While the design accommodates the resolutions of 3D printing, certain channels, being thin, long, and high, might pose challenges for common printers, potentially leading to deviations in electrical properties. Additive printing is advancing rapidly though, and it would be possible to

refine the techniques to print the small channels accurately (we have shown printing resolutions already of 30um in our lab). Additionally, the two ground electrodes on the upper and lower sides, being thin and wide due to space constraints, might see changes in voltage outcomes if they were changed to fit other dimensions.

For future endeavors, while SGNs have demonstrated the potential to survive in small canals and extend neurites through channels[138], the challenge lies in obtaining a sufficiently large number of SGNs, especially when dissecting from sources like rats. Patch clamp recording, accessed from the top of the RC canal with the CI inserted for stimulation, is considered the most feasible way to use this model. This approach offers a unique opportunity to study the true SGN response to CI extracellular stimulations, representing a valuable advancement in comparison to conventional SGN patch clamp studies involving intracellular stimulation.

6 DISCUSSIONS

6.1 Summary of Finding

This thesis harnesses computational techniques as its foundational approach, supplementing it with insights from cadaveric and clinical studies to validate the findings. The research delves deep into the mechanics of cochlear implants and offers explanations to address some unresolved clinical conundrums. Notably, this work stands out as the first to incorporate models of the internal auditory meatus (IAM) and precise porous modiolus. Moreover, it presents a pioneering effort in precisely replicating temporal bone specimens and their physical measurement conditions through computational models. The detailed findings are succinctly summarized below:

Chapter 2 pioneers the direct validation of computational cochlear models by comparing simulation outputs with physical measurements from replicated human temporal bone specimens in simulations. Utilizing micro-CT scans, this research studied the electrical field imaging (EFIs) and wire-recorded voltages between the simulated and physical environments. This chapter establishes a foundational groundwork for subsequent chapters.

Chapter 3 built an accurate cochlea model based on high-resolution synchrotron scans. The models of the human head, skull, IAM, etc., are from other open CT databases. Including the IAM in the model made a great change to the simulation result, which might be an important factor but has been ignored by nearly all related works. The conductivity change from the bony modiolus to the hollow IAM will cause a rapid voltage change along the neurons (or auditory nerve fibers). Combining with the basic principles of activating functions, this voltage change causes different effects on the neurons when stimulating anodic or cathodic pulses from CI. This provides one explanation (or hypothesis) explaining how CI works in stimulating neurons, particularly for site and polarity responses. The anodic stimulations tend to stimulate central axons near the modiolus-IAM interface, while the cathodic stimulations will work best at the dendrites. Further based on this, the CI position in the scala tympani will not obviously affect CI outcomes as all CIs work at the modiolus-IAM interface for anodic stimulation. However, the peri-modiolar CIs show a slightly better performance when stimulating the dendrites. The "uncertain" improvement of peri-modiolar CIs and the polarity effect in simulations comply with clinical outcomes. This new hypothesis of site of stimulation and might

provide new insights to further understanding CIs (as results have been mostly unchanged for more than 20 years).

Chapter 4 shows the applications of the head model from the clinical aspect. By comparing the simulation results to clinical or cadaveric data, this chapter is also a validation of the head model. One major focus of this chapter is to study extra-cochlear (EE) electrodes. Two potential methods to detect 1EE clinically are proposed based on simulations. One of the methods is validated in a cadaveric head. The CI partial short case and stimulation-induced scalp voltages are also simulated and compared to clinical data. The simulations all show similar trends and amplitudes as in physical measurements, which is also additional proof of accuracy for the head model.

Chapter 5 proposed a proof-of-concept design for studying spiral ganglion neurons (SGNs) using an in vitro model. This model aims to replicate the voltage spread along SGNs upon cochlear implant (CI) stimulation, providing a tool for studying SGN responses. The design incorporates features such as compartments representing cochlear structures, allowing for MEA or patch clamp recordings of cultured SGNs. The detailed simulations demonstrate the feasibility of this in vitro model in replicating voltage patterns observed in the head model during CI stimulation.

In summary, the thesis combines computational modelling with cadaveric and clinical data to advance our understanding of cochlear implants. It introduces novel elements, such as the inclusion of the IAM in cochlear models and proposes a hypothesis explaining CI principles based on detailed simulations. The validation of the head model in clinical scenarios and the exploration of potential clinical applications, such as detecting extra-cochlear electrodes, contribute to the relevance and reliability of the models. Additionally, the thesis presents a forward-looking approach with the in vitro model, offering a potential tool for studying SGN responses to CI stimulation.

6.2 Future directions

The computational approach has demonstrated considerable efficacy in advancing our understanding of the cochlear structure and function. The hypotheses generated from

computational methodologies offer potentially groundbreaking insights into cochlear implant (CI) mechanisms. However, the validation of the hypothesis through cadaveric or animal models remains a crucial next step. This validation process includes examining spiral ganglion neuron (SGN) responses to external voltage stimulations, particularly the voltage profiles along trajectories as presented in Chapter 3. Such investigations could refine auditory nerve models, and when integrated with computational models, yield more accurate predictions.

Practically, some patients could understand CI induced hearing within weeks of usage, while some could hardly understand what they hear with CI even after a few years. Apart from the difference in neural health status, I would believe that the cochlear (including modiolus and IAM) structures of different patients will largely affect the CI stimulation outcomes, including the spread of excitations and stimulation thresholds. This thesis was only able to fully study the CI stimulation-induced neural activations in one cochlea. Despite the existence of potential clinical data indicating the importance of IAM in patients[106], it still remains as a hypothesis and might be hard to be accepted or proved in the foreseeable future.

For future works, it would be valuable to study and compare multiple cochleae with diverse structures to investigate how these variations impact neural activations. This could be beneficial for patients as we could assess or predict the CI outcomes of them based on examining their cochlear structures with possible CT scans prior to surgical implantations.

Moreover, the proposed computational models and methods could contribute to future CI research. The head model, containing extensive cochlear-related structures, paves the way for diverse applications across various research domains. The precise construction of these models ensures that simulation results not only reflect the trends of potential physical outcomes. The pursuit of increasingly refined models will continually enhance the accuracy of simulation results.

It is my aspiration that this thesis casts a new light on the enigmatic question of how CIs function. Should the hypothesis prove valid in future studies, it holds the potential to inform the design of the next generations of CIs. It has been proved that changing CI

positions, increasing electrode numbers, or deepening CI insertions are not effective in terms of pursuing better performance. I would tend to believe that this reflects the limitation of CI insertions in the scala tympani. However, surgically, CI insertion into the scala tympani through round window may still be the easiest way for clinical practice, as the access to IAM will be much more complicated. Foreseeing the future directions could be hard, but building reliable models for now will always be helpful.

REFERENCES

1 Zeng, F. G. Celebrating the one millionth cochlear implant. *JASA Express Lett* **2**, 077201, doi:10.1121/10.0012825 (2022).

2 Zeng, F. G. Challenges in Improving Cochlear Implant Performance and Accessibility. *IEEE Trans Biomed Eng* **64**, 1662-1664, doi:10.1109/TBME.2017.2718939 (2017).

3 Moser, T., Predoehl, F. & Starr, A. Review of Hair Cell Synapse Defects in Sensorineural Hearing Impairment. *Otology & Neurotology* **34**, doi:10.1097/MAO.0b013e3182814d4a (2013).

4 Takeno, S., Wake, M., Mount, R. J. & Harrison, R. V. Degeneration of Spiral Ganglion Cells in the Chinchilla afterInner H air Cell Loss Induced by Carboplatin. *Audiology and Neurotology* **3**, 281-290 (1998).

5 Sharon, G. K. & Liberman, M. C. Adding Insult to Injury: Cochlear Nerve Degeneration after "Temporary" Noise-Induced Hearing Loss. *The Journal of Neuroscience* **29**, 14077, doi:10.1523/JNEUROSCI.2845-09.2009 (2009).

6 Lei, I. M. *et al.* 3D printed biomimetic cochleae and machine learning co-modelling provides clinical informatics for cochlear implant patients. *Nat Commun* **12**, 6260, doi:10.1038/s41467-021-26491-6 (2021).

7 Zeng, F. G., Rebscher, S., Harrison, W., Sun, X. & Feng, H. Cochlear Implants: System Design, Integration, and Evaluation. *IEEE Reviews in Biomedical Engineering* **1**, 115-142, doi:10.1109/RBME.2008.2008250 (2008).

8 Clark, G. M. *et al.* The University of Melbourne--nucleus multi-electrode cochlear implant. *Advances in oto-rhino-laryngology* **38**, V-IX (1987).

9 Wilson, B. S. *et al.* Better speech recognition with cochlear implants. *Nature* **352**, 236-238 (1991).

10 Jiang, C. *et al.* An Instrumented Cochlea Model for the Evaluation of Cochlear Implant Electrical Stimulus Spread. *IEEE Trans Biomed Eng* **68**, 2281-2288, doi:10.1109/TBME.2021.3059302 (2021).

11 Soderqvist, S. *et al.* Intraoperative transimpedance and spread of excitation profile correlations with a lateral-wall cochlear implant electrode array. *Hear Res* **405**, 108235, doi:10.1016/j.heares.2021.108235 (2021).

12 Biesheuvel, J. D., Briaire, J. J., de Jong, M. A. M., Boehringer, S. & Frijns, J. H. M. Channel discrimination along all contacts of the cochlear implant electrode array and its relation to speech perception. *Int J Audiol* **58**, 262-268, doi:10.1080/14992027.2019.1573384 (2019).

13 Joly, C.-A. *et al.* Intra-Cochlear Current Spread Correlates with Speech Perception in Experienced Adult Cochlear Implant Users. *Journal of Clinical Medicine* **10** (2021).

14 Parkinson, A. J. *et al.* The Nucleus® 24 Contour™ Cochlear Implant System: Adult Clinical Trial Results. *Ear and Hearing* **23** (2002).

15 Dhanasingh, A. & Jolly, C. An overview of cochlear implant electrode array designs. *Hear Res* **356**, 93-103, doi:10.1016/j.heares.2017.10.005 (2017).

16 Hughes, M. L. & Abbas, P. J. Electrophysiologic channel interaction, electrode pitch ranking, and behavioral threshold in straight versus perimodiolar cochlear

implant electrode arraysa). *The Journal of the Acoustical Society of America* **119**, 1538-1547, doi:10.1121/1.2164969 (2006).
17 Lee, J. Y. *et al.* Effect of Cochlear Implant Electrode Array Design on Electrophysiological and Psychophysical Measures: Lateral Wall versus Perimodiolar Types. *J Audiol Otol* **23**, 145-152, doi:10.7874/jao.2019.00164 (2019).
18 De Seta, D. *et al.* Five-Year Hearing Outcomes in Bilateral Simultaneously Cochlear-Implanted Adult Patients. *Audiol Neurootol* **21**, 261-267, doi:10.1159/000448582 (2016).
19 Esquia Medina, G. N. *et al.* Is electrode-modiolus distance a prognostic factor for hearing performances after cochlear implant surgery? *Audiol Neurootol* **18**, 406-413, doi:10.1159/000354115 (2013).
20 van der Beek, F. B., Briaire, J. J. & Frijns, J. H. Population-based prediction of fitting levels for individual cochlear implant recipients. *Audiol Neurootol* **20**, 1-16, doi:10.1159/000362779 (2015).
21 Jwair, S. *et al.* Scalar Translocation Comparison Between Lateral Wall and Perimodiolar Cochlear Implant Arrays - A Meta-Analysis. *Laryngoscope* **131**, 1358-1368, doi:10.1002/lary.29224 (2021).
22 Basta, D., Todt, I. & Ernst, A. Audiological outcome of the pull-back technique in cochlear implantees. *Laryngoscope* **120**, 1391-1396, doi:10.1002/lary.20942 (2010).
23 Greisiger, R. *et al.* Effect of Proximity to the Modiolus for the Cochlear CI532 Slim Modiolar Electrode Array on Evoked Compound Action Potentials and Programming Levels. *Audiol Neurootol* **27**, 397-405, doi:10.1159/000524256 (2022).
24 Todt, I., Basta, D. & Ernst, A. Helix electrode pull back: electrophysiology and surgical results. *Cochlear Implants Int* **12 Suppl 1**, S73-75, doi:10.1179/146701011X13001035752930 (2011).
25 Eitutis, S. T. *et al.* A Multicenter Comparison of 1-yr Functional Outcomes and Programming Differences Between the Advanced Bionics Mid-Scala and SlimJ Electrode Arrays. *Otology & Neurotology* **44** (2023).
26 Luo, X. & Wu, C.-C. Symmetric Electrode Spanning Narrows the Excitation Patterns of Partial Tripolar Stimuli in Cochlear Implants. *Journal of the Association for Research in Otolaryngology* **17**, 609-619, doi:10.1007/s10162-016-0582-8 (2016).
27 Tang, Q., Benítez, R. & Zeng, F.-G. Spatial channel interactions in cochlear implants. *Journal of Neural Engineering* **8**, 046029, doi:10.1088/1741-2560/8/4/046029 (2011).
28 Carlyon, R. P. & Goehring, T. Cochlear Implant Research and Development in the Twenty-first Century: A Critical Update. *J Assoc Res Otolaryngol* **22**, 481-508, doi:10.1007/s10162-021-00811-5 (2021).
29 Macherey, O., Van Wieringen, A., Carlyon, R. P., Deeks, J. M. & Wouters, J. Asymmetric pulses in cochlear implants: effects of pulse shape, polarity, and rate. *Journal of the Association for Research in Otolaryngology* **7**, 253-266 (2006).
30 Carlyon, R. P., Deeks, J. M. & Macherey, O. Polarity effects on place pitch and loudness for three cochlear-implant designs and at different cochlear sites. *The Journal of the Acoustical Society of America* **134**, 503-509 (2013).
31 He, S., Teagle, H. F. B. & Buchman, C. A. The Electrically Evoked Compound Action Potential: From Laboratory to Clinic. *Front Neurosci* **11**, 339, doi:10.3389/fnins.2017.00339 (2017).

32 Undurraga, J. A., Carlyon, R. P., Macherey, O., Wouters, J. & van Wieringen, A. Spread of excitation varies for different electrical pulse shapes and stimulation modes in cochlear implants. *Hearing Research* **290**, 21-36, doi:10.1016/j.heares.2012.05.003 (2012).
33 Undurraga, J. A., Carlyon, R. P., Wouters, J. & van Wieringen, A. The polarity sensitivity of the electrically stimulated human auditory nerve measured at the level of the brainstem. *J Assoc Res Otolaryngol* **14**, 359-377, doi:10.1007/s10162-013-0377-0 (2013).
34 Leake, P. A. & Hradek, G. T. Cochlear pathology of long term neomycin induced deafness in cats. *Hearing research* **33**, 11-33 (1988).
35 Briaire, J. J. & Frijns, J. H. M. Unraveling the electrically evoked compound action potential. *Hearing research* **205**, 143-156 (2005).
36 Resnick, J. M., O'Brien, G. E. & Rubinstein, J. T. Simulated auditory nerve axon demyelination alters sensitivity and response timing to extracellular stimulation. *Hear Res* **361**, 121-137, doi:10.1016/j.heares.2018.01.014 (2018).
37 Joshi, S. N., Dau, T. & Epp, B. A Model of Electrically Stimulated Auditory Nerve Fiber Responses with Peripheral and Central Sites of Spike Generation. *J Assoc Res Otolaryngol* **18**, 323-342, doi:10.1007/s10162-016-0608-2 (2017).
38 Mesnildrey, Q., Venail, F., Carlyon, R. P. & Macherey, O. Polarity Sensitivity as a Potential Correlate of Neural Degeneration in Cochlear Implant Users. *Journal of the Association for Research in Otolaryngology* **21**, 89-104, doi:10.1007/s10162-020-00742-7 (2020).
39 Goehring, T., Archer-Boyd, A., Deeks, J. M., Arenberg, J. G. & Carlyon, R. P. A Site-Selection Strategy Based on Polarity Sensitivity for Cochlear Implants: Effects on Spectro-Temporal Resolution and Speech Perception. *Journal of the Association for Research in Otolaryngology* **20**, 431-448, doi:10.1007/s10162-019-00724-4 (2019).
40 Rattay, F., Lutter, P. & Felix, H. A model of the electrically excited human cochlear neuron: I. Contribution of neural substructures to the generation and propagation of spikes. *Hearing Research* **153**, 43-63, doi:10.1016/S0378-5955(00)00256-2 (2001).
41 Rattay, F. The basic mechanism for the electrical stimulation of the nervous system. *Neuroscience* **89**, 335-346, doi:10.1016/S0306-4522(98)00330-3 (1999).
42 Joshi, S. N., Dau, T. & Epp, B. A Model of Electrically Stimulated Auditory Nerve Fiber Responses with Peripheral and Central Sites of Spike Generation. *Journal of the Association for Research in Otolaryngology* **18**, 323-342, doi:10.1007/s10162-016-0608-2 (2017).
43 Goehring, J. L., Hughes, M. L., Baudhuin, J. L. & Lusk, R. P. How well do cochlear implant intraoperative impedance measures predict postoperative electrode function? *Otology & neurotology* **34**, 239 (2013).
44 Mesnildrey, Q., Macherey, O., Herzog, P. & Venail, F. Impedance measures for a better understanding of the electrical stimulation of the inner ear. *Journal of Neural Engineering* **16**, 016023 (2019).
45 Oberhoffner, T. *et al.* Effects of Intraoperative Cochlear Implant Electrode Conditioning on Impedances and Electrically Evoked Compound Action Potentials. *IEEE Transactions on Biomedical Engineering*, 1-10, doi:10.1109/TBME.2023.3313198 (2023).
46 Vanpoucke, F. J., Zarowski, A. J. & Peeters, S. A. Identification of the impedance model of an implanted cochlear prosthesis from intracochlear potential measurements. *IEEE Transactions on Biomedical Engineering* **51**, 2174-2183, doi:10.1109/TBME.2004.836518 (2004).

47 de Rijk, S. R., Tam, Y. C., Carlyon, R. P. & Bance, M. L. Detection of Extracochlear Electrodes in Cochlear Implants with Electric Field Imaging/Transimpedance Measurements:: A Human Cadaver Study. *Ear and hearing* **41**, 1196 (2020).
48 Zuniga, M. G. *et al.* Tip Fold-over in Cochlear Implantation: Case Series. *Otology & Neurotology* **38** (2017).
49 Schraivogel, S. *et al.* Postoperative Impedance-Based Estimation of Cochlear Implant Electrode Insertion Depth. *Ear Hear*, doi:10.1097/AUD.0000000000001379 (2023).
50 Aebischer, P., Meyer, S., Caversaccio, M. & Wimmer, W. Intraoperative Impedance-Based Estimation of Cochlear Implant Electrode Array Insertion Depth. *IEEE Trans Biomed Eng* **68**, 545-555, doi:10.1109/TBME.2020.3006934 (2021).
51 Soderqvist, S., Sivonen, V., Koivisto, J., Aarnisalo, A. & Sinkkonen, S. T. Spread of the intracochlear electrical field: Implications for assessing electrode array location in cochlear implantation. *Hear Res* **434**, 108790, doi:10.1016/j.heares.2023.108790 (2023).
52 Cosentino, S., Gaudrain, E., Deeks, J. M. & Carlyon, R. P. Multistage Nonlinear Optimization to Recover Neural Activation Patterns From Evoked Compound Action Potentials of Cochlear Implant Users. *IEEE Transactions on Biomedical Engineering* **63**, 833-840, doi:10.1109/TBME.2015.2476373 (2016).
53 Kopsch, A. C., Rahne, T., Plontke, S. K. & Wagner, L. Influence of the spread of electric field on neural excitation in cochlear implant users: Transimpedance and spread of excitation measurements. *Hear Res* **424**, 108591, doi:10.1016/j.heares.2022.108591 (2022).
54 Biesheuvel, J. D., Briaire, J. J., Kalkman, R. K. & Frijns, J. H. M. The effect of stimulus level on excitation patterns of individual electrode contacts in cochlear implants. *Hear Res* **420**, 108490, doi:10.1016/j.heares.2022.108490 (2022).
55 Skidmore, J. *et al.* A Broadly Applicable Method for Characterizing the Slope of the Electrically Evoked Compound Action Potential Amplitude Growth Function. *Ear Hear* **43**, 150-164, doi:10.1097/AUD.0000000000001084 (2022).
56 Garcia, C. *et al.* The Panoramic ECAP Method: Estimating Patient-Specific Patterns of Current Spread and Neural Health in Cochlear Implant Users. *J Assoc Res Otolaryngol* **22**, 567-589, doi:10.1007/s10162-021-00795-2 (2021).
57 Saeed, S. R. *et al.* The Use of Cone-Beam Computed Tomography to Determine Cochlear Implant Electrode Position in Human Temporal Bones. *Otology & Neurotology* **35** (2014).
58 Gee, A. H., Zhao, Y., Treece, G. M. & Bance, M. L. Practicable assessment of cochlear size and shape from clinical CT images. *Sci Rep* **11**, 3448, doi:10.1038/s41598-021-83059-6 (2021).
59 Elfarnawany, M. *et al.* Micro-CT versus synchrotron radiation phase contrast imaging of human cochlea. *J Microsc* **265**, 349-357, doi:10.1111/jmi.12507 (2017).
60 Mei, X. *et al.* Vascular Supply of the Human Spiral Ganglion: Novel Three-Dimensional Analysis Using Synchrotron Phase-Contrast Imaging and Histology. *Sci Rep* **10**, 5877, doi:10.1038/s41598-020-62653-0 (2020).
61 Bellos, C. *et al.* Reconstruction of Cochlea Based on Micro-CT and Histological Images of the Human Inner Ear. *BioMed Research International* **2014**, 485783, doi:10.1155/2014/485783 (2014).

62 Rask-Andersen, H., Schrott-Fischer, A., Pfaller, K. & Glueckert, R. Perilymph/Modiolar Communication Routes in the Human Cochlea. *Ear and Hearing* **27** (2006).
63 Wright, C. G. & Roland, P. S. *Cochlear Anatomy via Microdissection with Clinical Implications: an Atlas*. (Springer, 2018).
64 Orzan, E. *et al.* Correlation of cochlear aperture stenosis with cochlear nerve deficiency in congenital unilateral hearing loss and prognostic relevance for cochlear implantation. *Scientific Reports* **11**, 3338, doi:10.1038/s41598-021-82818-9 (2021).
65 Frijns, J. H. M., Briaire, J. J. & Grote, J. J. The Importance of Human Cochlear Anatomy for the Results of Modiolus-Hugging Multichannel Cochlear Implants. *Otology & Neurotology* **22** (2001).
66 Frijns, J. H. M., Briaire, J. J. & Schoonhoven, R. Integrated use of volume conduction and neural models to simulate the response to cochlear implants. *Simulation Practice and Theory* **8**, 75-97, doi:10.1016/S0928-4869(00)00008-2 (2000).
67 Rattay, F., Leao, R. N. & Felix, H. A model of the electrically excited human cochlear neuron. II. Influence of the three-dimensional cochlear structure on neural excitability. *Hearing Research* **153**, 64-79, doi:10.1016/S0378-5955(00)00257-4 (2001).
68 Frijns *et al.* Simultaneous and non-simultaneous dual electrode stimulation in cochlear implants: evidence for two neural response modalities. *Acta Oto-Laryngologica* **129**, 433-439, doi:10.1080/00016480802610218 (2009).
69 Kalkman, R. K., Briaire, J. J., Dekker, D. M. & Frijns, J. H. Place pitch versus electrode location in a realistic computational model of the implanted human cochlea. *Hear Res* **315**, 10-24, doi:10.1016/j.heares.2014.06.003 (2014).
70 Kalkman, R. K., Briaire, J. J. & Frijns, J. H. Current focussing in cochlear implants: an analysis of neural recruitment in a computational model. *Hear Res* **322**, 89-98, doi:10.1016/j.heares.2014.12.004 (2015).
71 van Gendt, M. J., Briaire, J. J., Kalkman, R. K. & Frijns, J. H. M. A fast, stochastic, and adaptive model of auditory nerve responses to cochlear implant stimulation. *Hear Res* **341**, 130-143, doi:10.1016/j.heares.2016.08.011 (2016).
72 Dickinson, E. J. F., Ekström, H. & Fontes, E. COMSOL Multiphysics®: Finite element software for electrochemical analysis. A mini-review. *Electrochemistry communications* **40**, 71-74 (2014).
73 Neufeld, E., Cassará, A. M., Montanaro, H., Kuster, N. & Kainz, W. Functionalized anatomical models for EM-neuron Interaction modeling. *Physics in Medicine & Biology* **61**, 4390, doi:10.1088/0031-9155/61/12/4390 (2016).
74 Boulet, J., White, M. & Bruce, I. C. Temporal Considerations for Stimulating Spiral Ganglion Neurons with Cochlear Implants. *J Assoc Res Otolaryngol* **17**, 1-17, doi:10.1007/s10162-015-0545-5 (2016).
75 Heshmat, A. *et al.* Dendritic Degeneration of Human Auditory Nerve Fibers and Its Impact on the Spiking Pattern Under Regular Conditions and During Cochlear Implant Stimulation. *Front Neurosci* **14**, 599868, doi:10.3389/fnins.2020.599868 (2020).
76 Nogueira, W., Schurzig, D., Buchner, A., Penninger, R. T. & Wurfel, W. Validation of a Cochlear Implant Patient-Specific Model of the Voltage Distribution in a Clinical Setting. *Front Bioeng Biotechnol* **4**, 84, doi:10.3389/fbioe.2016.00084 (2016).
77 Ceresa, M., Mangado, N., Andrews, R. J. & Gonzalez Ballester, M. A. Computational Models for Predicting Outcomes of Neuroprosthesis Implantation:

the Case of Cochlear Implants. *Mol Neurobiol* **52**, 934-941, doi:10.1007/s12035-015-9257-4 (2015).
78 Potrusil, T. *et al.* Finite element analysis and three-dimensional reconstruction of tonotopically aligned human auditory fiber pathways: A computational environment for modeling electrical stimulation by a cochlear implant based on micro-CT. *Hear Res* **393**, 108001, doi:10.1016/j.heares.2020.108001 (2020).
79 Tran, P., Sue, A., Wong, P., Li, Q. & Carter, P. Development of HEATHER for cochlear implant stimulation using a new modeling workflow. *IEEE Trans Biomed Eng* **62**, 728-735, doi:10.1109/TBME.2014.2364297 (2015).
80 Malherbe, T. K., Hanekom, T. & Hanekom, J. J. The effect of the resistive properties of bone on neural excitation and electric fields in cochlear implant models. *Hear Res* **327**, 126-135, doi:10.1016/j.heares.2015.06.003 (2015).
81 Malherbe, T. K., Hanekom, T. & Hanekom, J. J. Constructing a three-dimensional electrical model of a living cochlear implant user's cochlea. *Int J Numer Method Biomed Eng* **32**, doi:10.1002/cnm.2751 (2016).
82 Mangado, N. *et al.* Computational Evaluation of Cochlear Implant Surgery Outcomes Accounting for Uncertainty and Parameter Variability. *Front Physiol* **9**, 498, doi:10.3389/fphys.2018.00498 (2018).
83 Mangado, N. *et al.* Towards a Complete In Silico Assessment of the Outcome of Cochlear Implantation Surgery. *Mol Neurobiol* **55**, 173-186, doi:10.1007/s12035-017-0731-z (2018).
84 Brochier, T. *et al.* From Microphone to Phoneme: An End-to-End Computational Neural Model for Predicting Speech Perception with Cochlear Implants. *IEEE Trans Biomed Eng* **69**, 3300 - 3312, doi:10.1109/TBME.2022.3167113 (2022).
85 Bai, S. *et al.* Electrical Stimulation in the Human Cochlea: A Computational Study Based on High-Resolution Micro-CT Scans. *Front Neurosci* **13**, 1312, doi:10.3389/fnins.2019.01312 (2019).
86 Croner, A. M. *et al.* Effects of Degrees of Degeneration on the Electrical Excitation of Human Spiral Ganglion Neurons Based on a High-Resolution Computer Model. *Front Neurosci* **16**, 914876, doi:10.3389/fnins.2022.914876 (2022).
87 Liu, W., Glueckert, R., Schrott-Fischer, A. & Rask-Andersen, H. Human cochlear microanatomy – an electron microscopy and super-resolution structured illumination study and review. *Hearing, Balance and Communication* **18**, 256-269, doi:10.1080/21695717.2020.1807259 (2020).
88 Bachmaier, R., Encke, J., Obando-Leiton, M., Hemmert, W. & Bai, S. Comparison of Multi-Compartment Cable Models of Human Auditory Nerve Fibers. *Front Neurosci* **13**, 1173, doi:10.3389/fnins.2019.01173 (2019).
89 Hodgkin, A. L. & Huxley, A. F. A quantitative description of membrane current and its application to conduction and excitation in nerve. *The Journal of Physiology* **117**, 500-544, doi:10.1113/jphysiol.1952.sp004764 (1952).
90 Briaire, J. J. & Frijns, J. H. M. Unraveling the electrically evoked compound action potential. *Hearing Research* **205**, 143-156, doi:10.1016/j.heares.2005.03.020 (2005).
91 Rusznák, Z. & Szűcs, G. Spiral ganglion neurones: an overview of morphology, firing behaviour, ionic channels and function. *Pflügers Archiv - European Journal of Physiology* **457**, 1303-1325, doi:10.1007/s00424-008-0586-2 (2009).
92 McNeal, D. R. Analysis of a Model for Excitation of Myelinated Nerve. *IEEE Transactions on Biomedical Engineering* **BME-23**, 329-337, doi:10.1109/TBME.1976.324593 (1976).

93 Lertmanorat, Z. & Durand, D. M. A novel electrode array for diameter-dependent control of axonal excitability: a Simulation study. *IEEE Transactions on Biomedical Engineering* **51**, 1242-1250, doi:10.1109/TBME.2004.827347 (2004).
94 Schuman, T. A. *et al.* Anatomic verification of a novel method for precise intrascalar localization of cochlear implant electrodes in adult temporal bones using clinically available computed tomography. *Laryngoscope* **120**, 2277-2283, doi:10.1002/lary.21104 (2010).
95 Ergun, O. *et al.* The hidden cochlear implant. *The Journal of Laryngology & Otology*, 1-8, doi:10.1017/S0022215123000130 (2023).
96 Jwair, S., Versnel, H., Stokroos, R. J. & Thomeer, H. The effect of the surgical approach and cochlear implant electrode on the structural integrity of the cochlea in human temporal bones. *Sci Rep* **12**, 17068, doi:10.1038/s41598-022-21399-7 (2022).
97 Jiang, C., de Rijk, S. R., Malliaras, G. G. & Bance, M. L. Electrochemical impedance spectroscopy of human cochleas for modeling cochlear implant electrical stimulus spread. *APL Mater* **8**, 091102, doi:10.1063/5.0012514 (2020).
98 Kashikar, T. S., Kerwin, T. F., Moberly, A. C. & Wiet, G. J. A review of simulation applications in temporal bone surgery. *Laryngoscope Investig Otolaryngol* **4**, 420-424, doi:10.1002/lio2.277 (2019).
99 Anschuetz, L. *et al.* Cochlear Implant Insertion Depth Prediction: A Temporal Bone Accuracy Study. *Otology & Neurotology* **39** (2018).
100 Treece, G. M., Prager, R. W., Gee, A. H. & Berman, L. Surface interpolation from sparse cross sections using region correspondence. *IEEE Transactions on Medical Imaging* **19**, 1106-1114, doi:10.1109/42.896787 (2000).
101 Sauerheber, R. & Heinz, B. Temperature effects on conductivity of seawater and physiologic saline, Mechanism and Significance. *Chem. Sci. J* **6**, 4172 (2015).
102 Hasgall, P. A., Neufeld, E., Gosselin, C., Klingenb, M.A., Kuster, N. *IT'IS Database for thermal and electromagnetic parameters of biological tissues*, <www.itis.ethz.ch/database> (2015).
103 Sieber, D. *et al.* The OpenEar library of 3D models of the human temporal bone based on computed tomography and micro-slicing. *Sci Data* **6**, 180297, doi:10.1038/sdata.2018.297 (2019).
104 Tykocinski, M., Cohen, L. T. & Cowan, R. S. Measurement and Analysis of Access Resistance and Polarization Impedance in Cochlear Implant Recipients. *Otology & Neurotology* **26** (2005).
105 Bierer, J. A., Deeks, J. M., Billig, A. J. & Carlyon, R. P. Comparison of signal and gap-detection thresholds for focused and broad cochlear implant electrode configurations. *J Assoc Res Otolaryngol* **16**, 273-284, doi:10.1007/s10162-015-0507-y (2015).
106 Finley, C. C., Holden, L. K., Holden, T. A. & Firszt, J. B. in *Conference on Implantable Auditory Prostheses (CIAP)* 54 (Lake Tahoe, CA, 2013).
107 Busby, P. A., Battmer, R. D. & Pesch, J. Electrophysiological Spread of Excitation and Pitch Perception for Dual and Single Electrodes Using the Nucleus Freedom Cochlear Implant. *Ear and Hearing* **29** (2008).
108 Litvak, L. M., Spahr, A. J. & Emadi, G. Loudness growth observed under partially tripolar stimulation: model and data from cochlear implant listeners. *J Acoust Soc Am* **122**, 967-981, doi:10.1121/1.2749414 (2007).
109 Caswell-Midwinter, B. & Arenberg, J. G. Comparing Fixed and Individualized Channel Interaction Coefficients for Speech Perception With Dynamic Focusing Cochlear Implant Strategies. *Trends Hear* **27**, 23312165231176157, doi:10.1177/23312165231176157 (2023).

110 Bierer, J. A. & Litvak, L. Reducing Channel Interaction Through Cochlear Implant Programming May Improve Speech Perception: Current Focusing and Channel Deactivation. *Trends Hear* **20**, doi:10.1177/2331216516653389 (2016).
111 Croghan, N. B. H., Duran, S. I. & Smith, Z. M. Re-examining the relationship between number of cochlear implant channels and maximal speech intelligibilitya). *The Journal of the Acoustical Society of America* **142**, EL537-EL543, doi:10.1121/1.5016044 (2017).
112 Glennon, E. *et al.* Locus coeruleus activity improves cochlear implant performance. *Nature* **613**, 317-323, doi:10.1038/s41586-022-05554-8 (2023).
113 Holder, J. T., Kessler, D. M., Noble, J. H., Gifford, R. H. & Labadie, R. F. Prevalence of Extracochlear Electrodes: Computerized Tomography Scans, Cochlear Implant Maps, and Operative Reports. *Otol Neurotol* **39**, e325-e331, doi:10.1097/MAO.0000000000001818 (2018).
114 Dietz, A., Wennstrom, M., Lehtimaki, A., Lopponen, H. & Valtonen, H. Electrode migration after cochlear implant surgery: more common than expected? *Eur Arch Otorhinolaryngol* **273**, 1411-1418, doi:10.1007/s00405-015-3716-4 (2016).
115 Lane, C., Zimmerman, K., Agrawal, S. & Parnes, L. Cochlear implant failures and reimplantation: A 30-year analysis and literature review. *The Laryngoscope* **130**, 782-789, doi:10.1002/lary.28071 (2020).
116 de Rijk, S. R. *et al.* Detection of Extracochlear Electrodes Using Stimulation-Current- Induced Non-Stimulating Electrode Voltage Recordings With Different Electrode Designs. *Otol Neurotol* **43**, e548-e557, doi:10.1097/MAO.0000000000003512 (2022).
117 Newbold, C., Risi, F., Hollow, R., Yusof, Y. & Dowell, R. Long-term electrode impedance changes and failure prevalence in cochlear implants. *International Journal of Audiology* **54**, 453-460, doi:10.3109/14992027.2014.1001076 (2015).
118 Tran, P., Richardson, M. L. & Zeng, F. G. Input-Output Functions in Human Heads Obtained With Cochlear Implant and Transcranial Electric Stimulation. *Neuromodulation* **24**, 1402-1411, doi:10.1111/ner.13065 (2021).
119 Grasmeder, M. *et al.* Piloting the recording of electrode voltages (REVS) using surface electrodes as a test to identify cochlear implant electrode migration, extra-cochlear electrodes and basal electrodes causing discomfort. *Cochlear Implants Int* **22**, 157-169, doi:10.1080/14670100.2020.1863701 (2021).
120 Gilley, P. M. *et al.* Minimization of cochlear implant stimulus artifact in cortical auditory evoked potentials. *Clin Neurophysiol* **117**, 1772-1782, doi:10.1016/j.clinph.2006.04.018 (2006).
121 Eitutis, S. T. *et al.* Detecting and managing partial shorts in Cochlear implants: A validation of scalp surface potential testing. *Clin Otolaryngol* **47**, 641-649, doi:10.1111/coa.13963 (2022).
122 Hilly, O. *et al.* Depth of Cochlear Implant Array Within the Cochlea and Performance Outcome. *Annals of Otology, Rhinology & Laryngology* **125**, 886-892, doi:10.1177/0003489416660111 (2016).
123 Sijgers, L. *et al.* Predicting Cochlear Implant Electrode Placement Using Monopolar, Three-Point and Four-Point Impedance Measurements. *IEEE Trans Biomed Eng* **69**, 2533-2544, doi:10.1109/TBME.2022.3150239 (2022).
124 Razmovski, T., Bester, C., Collins, A. & O'Leary, S. J. Four-point Impedance Changes in the Early Post-Operative Period After Cochlear Implantation. *Otol Neurotol* **43**, e730-e737, doi:10.1097/MAO.0000000000003592 (2022).
125 Goehring, J. L., Hughes, M. L., Baudhuin, J. L. & Lusk, R. P. How Well Do Cochlear Implant Intraoperative Impedance Measures Predict Postoperative Electrode Function? *Otology & Neurotology* **34** (2013).

126 *Target CI Fitting Guide CI-6057-001*, <https://www.advancedbionics.com/content/dam/advancedbionics/ifus/en_us/TargetCI%20FittingGuide.pdf> (2020).
127 Van Horn, A., Hayden, C., Mahairas, A. D., Leader, P. & Bush, M. L. Factors Influencing Aberrant Facial Nerve Stimulation Following Cochlear Implantation: A Systematic Review and Meta-analysis. *Otology & Neurotology* **41** (2020).
128 Leake, P. A., Hradek, G. T. & Snyder, R. L. Chronic electrical stimulation by a cochlear implant promotes survival of spiral ganglion neurons after neonatal deafness. *Journal of Comparative Neurology* **412**, 543-562 (1999).
129 Dhanasingh, A., C, N. J., Rajan, G. & van de Heyning, P. Literature Review on the Distribution of Spiral Ganglion Cell Bodies inside the Human Cochlear Central Modiolar Trunk. *J Int Adv Otol* **16**, 104-110, doi:10.5152/iao.2020.7510 (2020).
130 Guo, R. *et al.* Development and Application of Cochlear Implant-Based Electric-Acoustic Stimulation of Spiral Ganglion Neurons. *ACS Biomater Sci Eng* **5**, 6735-6741, doi:10.1021/acsbiomaterials.9b01265 (2019).
131 Meas, S. J., Nishimura, K., Scheibinger, M. & Dabdoub, A. In vitro Methods to Cultivate Spiral Ganglion Cells, and Purification of Cellular Subtypes for Induced Neuronal Reprogramming. *Front Neurosci* **12**, 822, doi:10.3389/fnins.2018.00822 (2018).
132 Mark, A. R., Nikolai, M. C. & Tobias, M. Spike Encoding of Neurotransmitter Release Timing by Spiral Ganglion Neurons of the Cochlea. *The Journal of Neuroscience* **32**, 4773, doi:10.1523/JNEUROSCI.4511-11.2012 (2012).
133 Skidmore, J., Ramekers, D., Bruce, I. C. & He, S. Comparison of response properties of the electrically stimulated auditory nerve reported in human listeners and in animal models. *Hearing Research* **426**, 108643, doi:10.1016/j.heares.2022.108643 (2022).
134 Reijntjes, D. O. J. & Pyott, S. J. The afferent signaling complex: Regulation of type I spiral ganglion neuron responses in the auditory periphery. *Hearing Research* **336**, 1-16, doi:10.1016/j.heares.2016.03.011 (2016).
135 Reid, M. A., Flores-Otero, J. & Davis, R. L. Firing patterns of type II spiral ganglion neurons in vitro. *J Neurosci* **24**, 733-742, doi:10.1523/JNEUROSCI.3923-03.2004 (2004).
136 Radotić, V., Braeken, D., Drviš, P., Mattotti, M. & Kovačić, D. Advantageous environment of micro-patterned, high-density complementary metal–oxide–semiconductor electrode array for spiral ganglion neurons cultured in vitro. *Scientific Reports* **8**, 7446, doi:10.1038/s41598-018-25814-w (2018).
137 Hahnewald, S. *et al.* Response profiles of murine spiral ganglion neurons on multi-electrode arrays. *Journal of Neural Engineering* **13**, 016011, doi:10.1088/1741-2560/13/1/016011 (2016).
138 Sevgili, I., Roberts, I. & Bance, M. *Spiral Ganglion-On-A-Chip*, <https://vepimg.b8cdn.com/uploads/vjfnew/content/files/16258514301307-poster-pdf1625851430.pdf> (2021).
139 Erixon, E., Högstorp, H., Wadin, K. & Rask-Andersen, H. Variational Anatomy of the Human Cochlea: Implications for Cochlear Implantation. *Otology & Neurotology* **30** (2009).
140 Lang, Q. *et al.* AC Electrothermal Circulatory Pumping Chip for Cell Culture. *ACS Appl Mater Interfaces* **7**, 26792-26801, doi:10.1021/acsami.5b08863 (2015).

APPENDICES

Appendix 1. Models of Human Temporal Bone Specimens

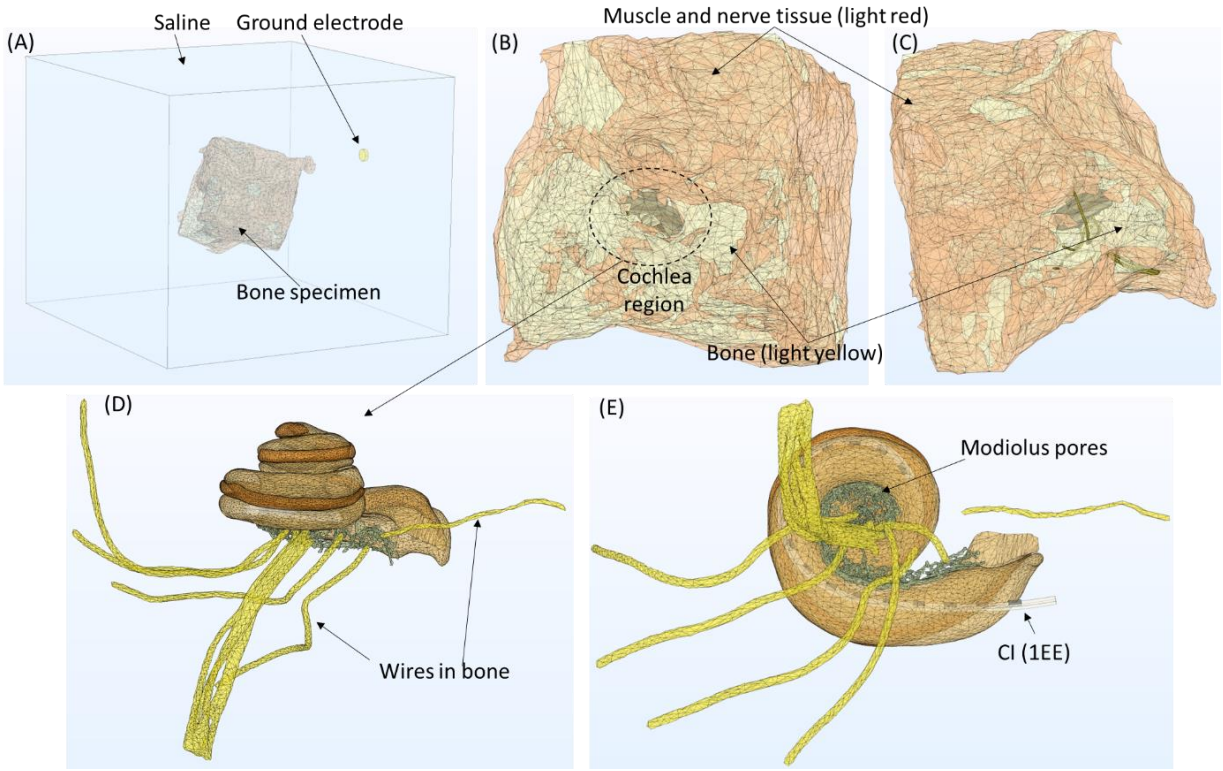

Figure A.1: The built human temporal bone specimen models of specimen 2. (A) The temporal bone specimen merged by saline. (B) and (C) show the specimen model in 2 different points of views. (D) The model of cochlea, modiolus, 10 recording wires, and CI. (E) The bottom view of cochlea.

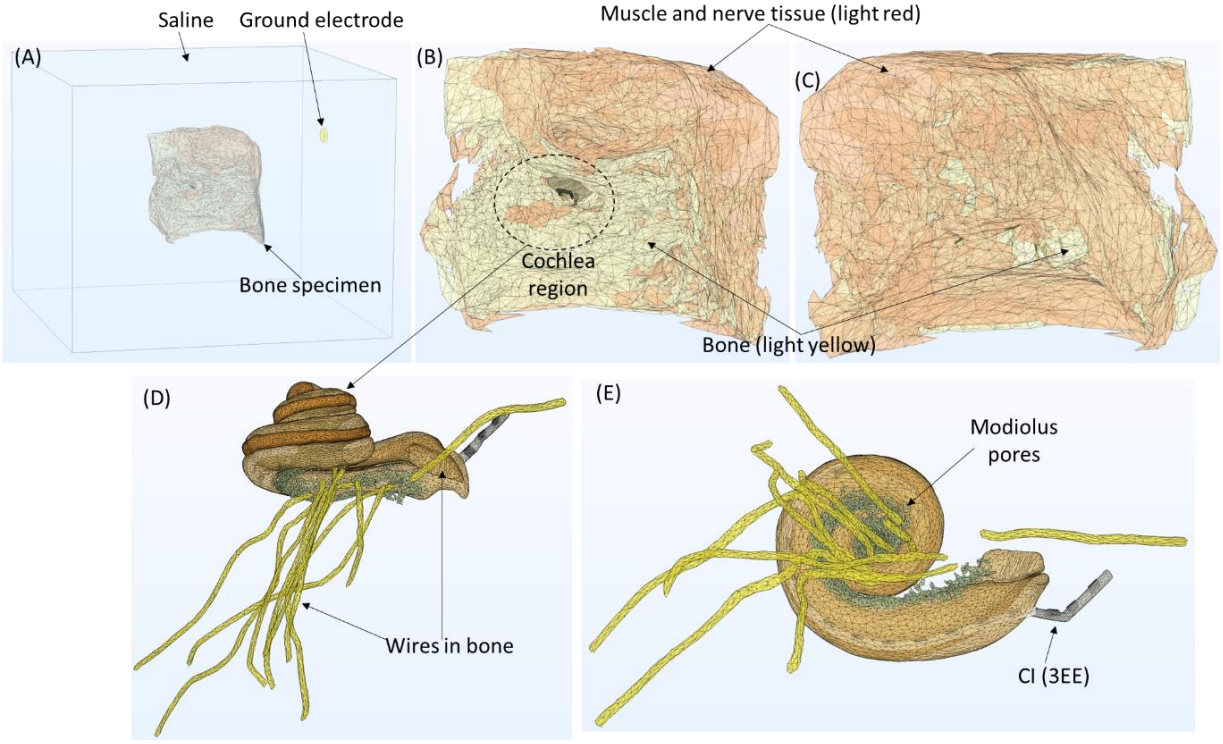

Figure A.2: The built human temporal bone specimen models of specimen 3. (A) The temporal bone specimen merged by saline block. (B) and (C) show the specimen model in 2 different points of views. The bone is mostly wrapped by muscle. (D) The model of cochlea, modiolus, 10 recording wires, and CI. (E) The bottom view of cochlea.

Appendix 2. Tripolar and Bipolar Results

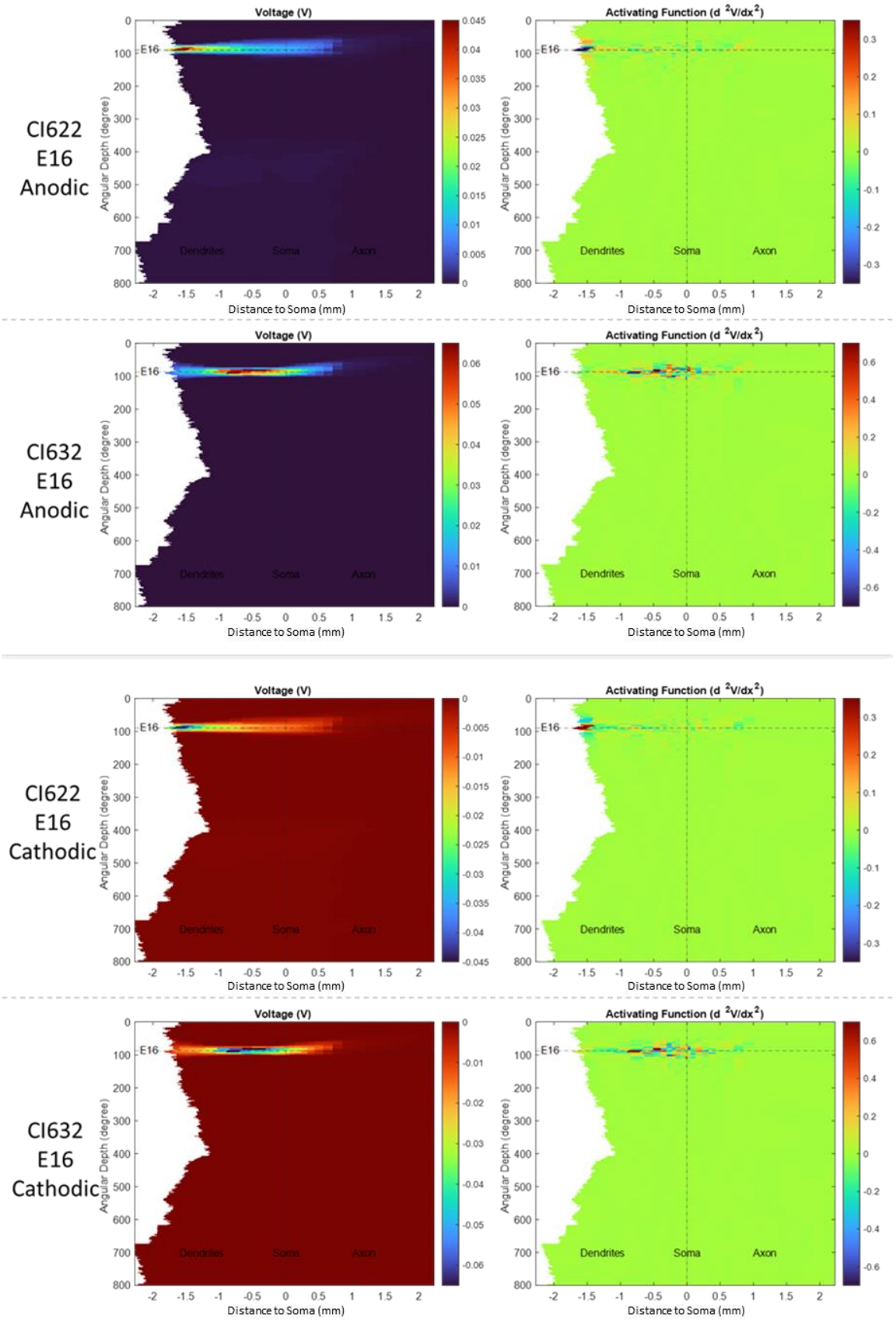

Figure A.3: Voltage and activating functions on trajectories by tripolar stimulations. Figures show both anodic and cathodic stimulations of electrode 16. Please note that the scales are different in CI622 and CI632.

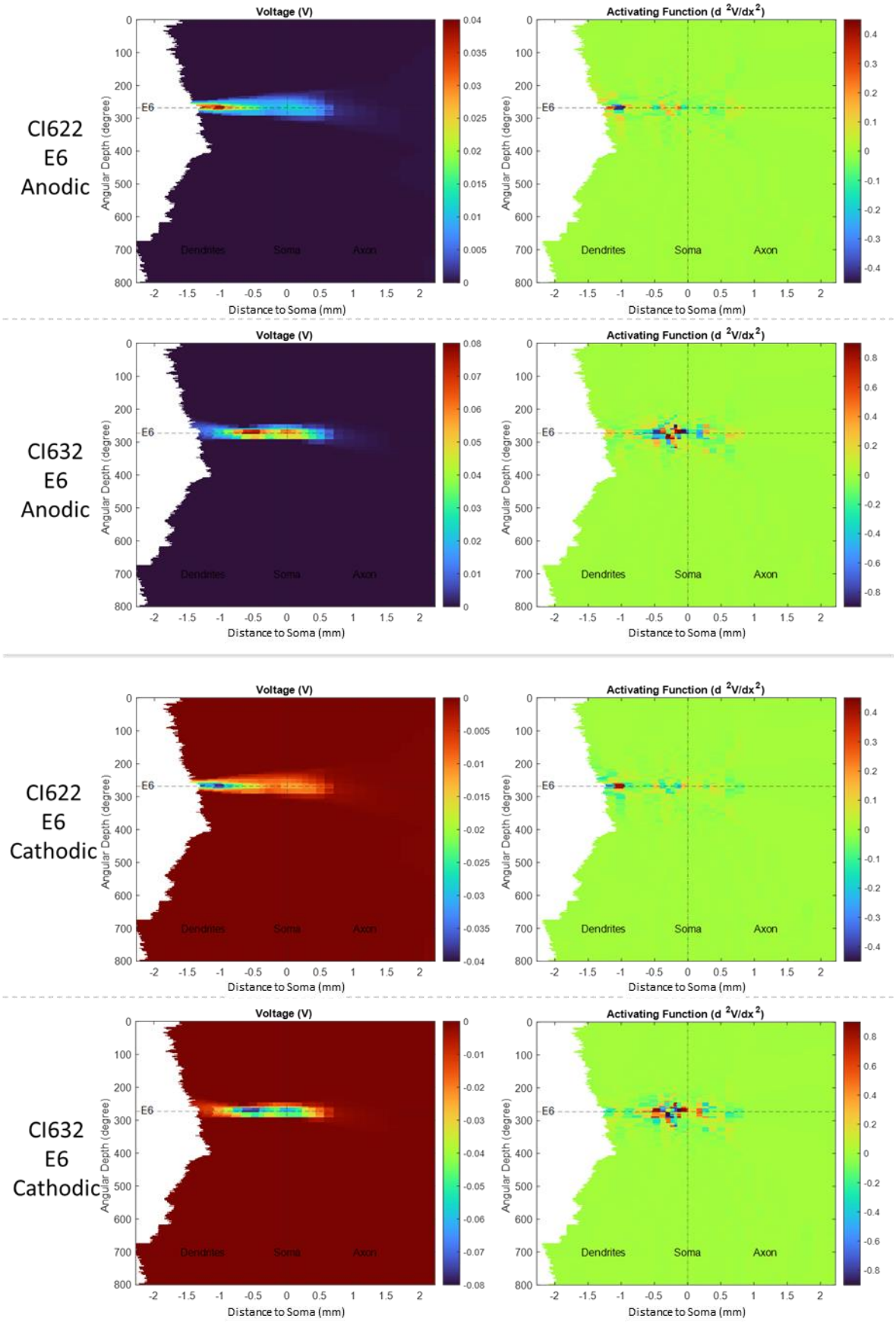

Figure A.3 (Continued): Voltage and activating functions on trajectories by tripolar stimulations. Figures show both anodic and cathodic stimulations of electrode 6. Please note that the scales are different in CI622 and CI632.

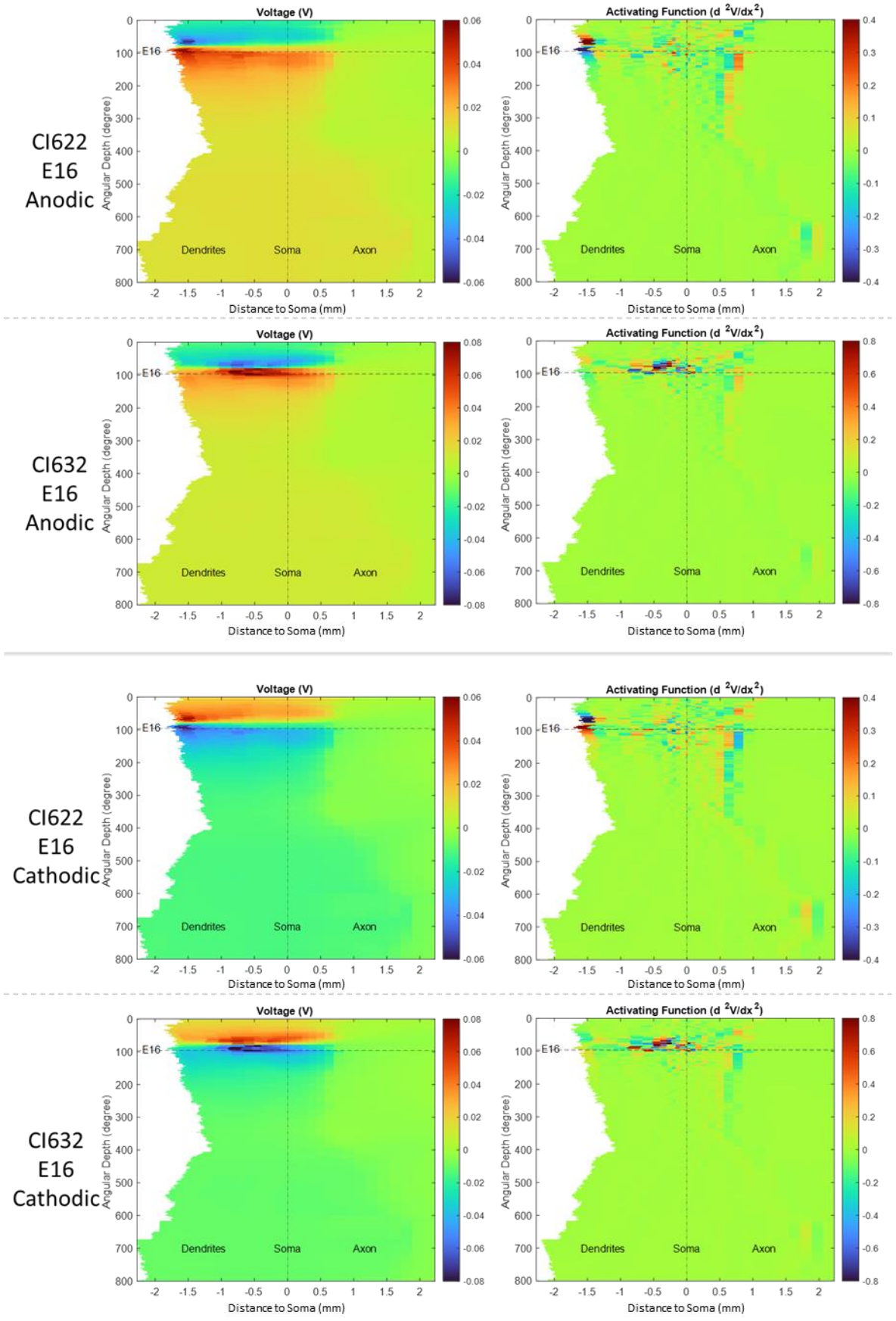

Figure A.4: Voltage and activating functions on trajectories by bipolar stimulations. Figures show both anodic and cathodic stimulations of electrode 16. Please note that the scales are different in CI622 and CI632.

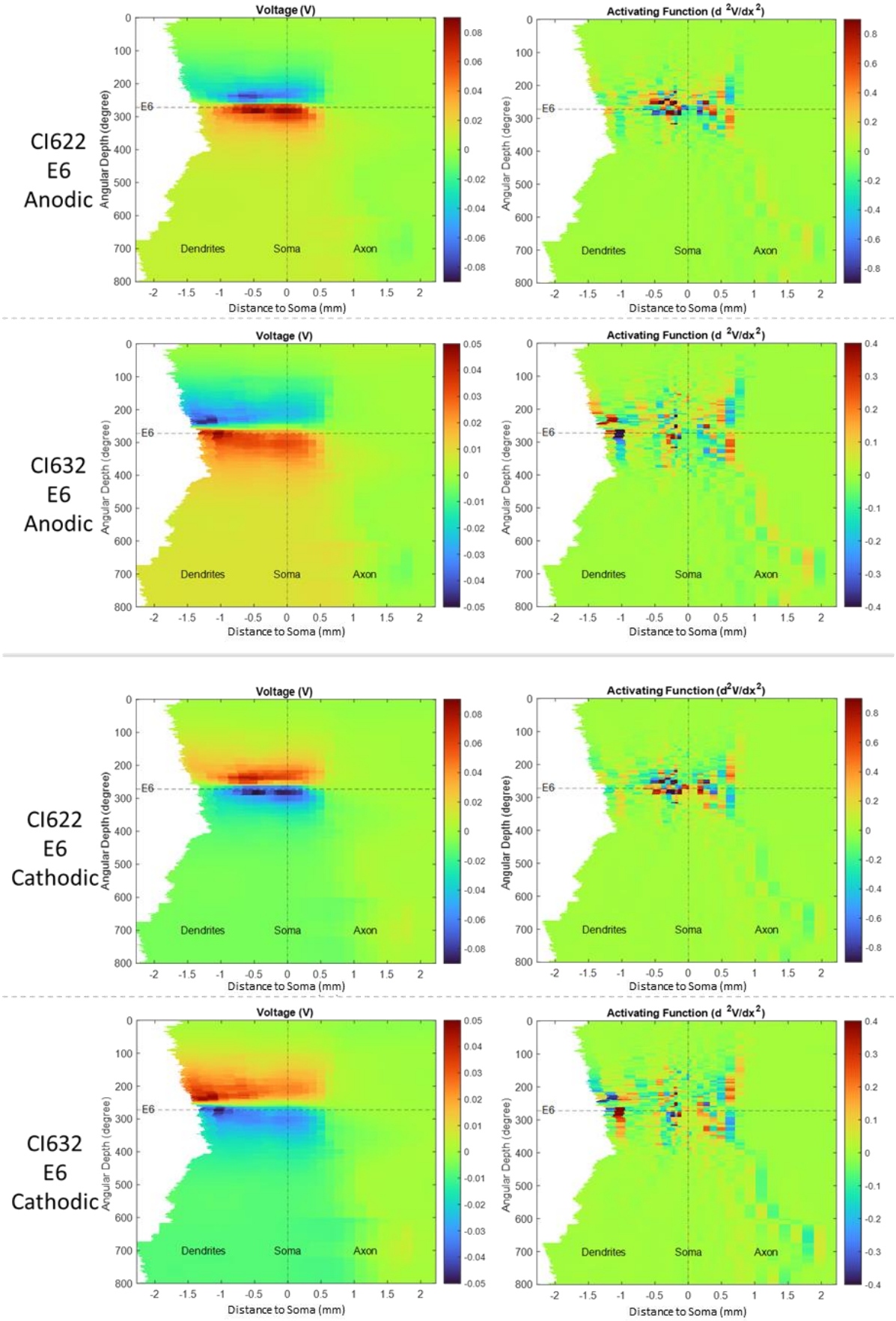

Figure A.4 (Continued): Voltage and activating functions on trajectories by bipolar stimulations. Figures show both anodic and cathodic stimulations of electrode 6. Please note that the scales are different in CI622 and CI632.